Universidade do Minho
Escola de Ciências

Joana Margarida Fernandes da Silva Ribeiro

Photocatalytic degradation of micropollutants with TiO_2/PVDF-TrFE membranes

novembro de 2016

Joana Margarida Fernandes da Silva Ribeiro **Photocatalytic degradation of micropollutants with TiO_2/PVDF-TrFE membranes**

UMinho | 2016

Universidade do Minho
Escola de Ciências

Joana Margarida Fernandes da Silva Ribeiro

Photocatalytic degradation of micropollutants with TiO_2/PVDF-TrFE membranes

Dissertação de Mestrado
Mestrado em Física
Ramo de Física Aplicada

Trabalho realizado sob orientação de
Doutor Senentxu Lanceros-Méndez
Doutora Luciana Pereira

novembro de 2016

ACKNOWLEDGEMENTS / AGRADECIMENTOS

During this journey, I feel the evolution of this work has led to my personal and scientific enrichment, mainly through the conjugation of factors such as the ERASMUS experience and the overall involvement of various institutions and people, who, together, helped me come this far and provided for a harmonious development of this thesis.

I would primarily like to thank University of Minho, which has been my institution throughout my bachelor and Masters. Particularly to the Department of Biological Engineering, where most of my experiments were conducted, and the Electroactive Smart Materials group, who accepted me among them and made me feel at home.

My sincere gratitude to my supervisor, PhD Senentxu Lanceros-Méndez, who made this master thesis possible, welcoming me into his workgroup, and actively supported my work. My thanks to my co-supervisor, PhD Luciana Pereira, for the incentive and support.

I would like to thank Technical University of Dresden, in particular the chair of Materials Science and Nanotechnology, in which my ERASMUS Program took place, and Prof. Dr. Gianaurelio Cuniberti, who accepted me into the group at TU Dresden and made this internship opportunity available. Dresden became my home for four months. I owe to my supervisor at TU Dresden, Dr. Klaus Kühn, for his kindness, vigilance and excellent supervision. To Sara Teixeira, my support pillar in Dresden, always making me smile from ear to ear and contributing for a good working environment.

Special thanks to my work colleague, Pedro Martins, my unofficial mentor, who always encouraged me to do my best, guiding me throughout the research and writing of this thesis and all our creative discussions. To the person that would always help me with anything she could, even at the cost of her free time, Rita Silva. To my work colleges Bruno, Henrique, Andrea, Lisa, Nga and Liliana for their help throughout my work.

To João, for his unconditional support and understanding. To my friends, who put up with me, and, last but not least, to my family, without whom I would not stand where I am.

Thank you for the love and support.

ABSTRACT

With the extensive use of chemicals produced through the development of technology, organic pollutants in water represent a major concern, as they constitute a potential risk for the ecosystem and human health. Furthermore, these compounds are extremely resistant to biological degradation processes and wastewater and drinking water treatment plants, causing their accumulation in water effluents. In this scope, Advanced Oxidation Processes arise as a possible solution, in particular, heterogeneous semiconductor photocatalysis. The primary aim of this study was to evaluate the effectiveness of immobilized titanium dioxide photocatalyst for the removal of pollutants from wastewater. Membranes of poly(vinylidene difluoride−trifluoroethylene) with 8% wt. P25 TiO_2 nanoparticles were produced by solvent casting, with and without the inclusion of zeolites (NaY) to improve wettability, characterized and applied in the photocatalytic degradation of four micropollutants: the cationic dyes Methylene Blue, the antibiotic Ciprofloxacin, the anti-inflammatory Ibuprofen and the plastic precursor Bisphenol A. All the produced membranes possess a highly porous structure, with interconnected pores and a degree of porosity around 70%, with pore sizes ranging between 30 and 80 μm. The composites present the characteristic absorption bands of β PVDF and show unchanged polymer structure in comparison to the pristine polymeric membrane, even after four uses. The membranes with TiO_2 and zeolites are more hydrophilic than the pristine membrane. The presence of TiO_2 nanoparticles modify the hydrophobic nature of the membranes after subjected to ultra violet, as does the inclusion of zeolites. In the first use, the membrane with zeolites degraded Methylene blue with higher efficiency, ≃ 98% after 300 min, and a degradation rate of ≃ 0.044 min^{-1}. The membrane without zeolites performed better in the degradation of Ciprofloxacin, ≃ 93% after 300 minutes, with a degradation rate of ≃ 0.010 min^{-1}. Bisphenol A was not degraded and Ibuprofen seemed to generate by-products during the reaction. In the first use, after 300 minutes, Ibuprofen degraded ≃ 18 and ≃ 48% and Bisphenol A degraded ≃ 7 and ≃ 3%, using membranes with and without zeolites, respectively. Overall, reutilization of the membranes showed little to no efficiency loss after fourth degradations of Methylene blue, and a slight increase in the degradation of Ciprofloxacin, ≃ 98% with a reaction rate of ≃ 0.015 min^{-1}, and of Ibuprofen, ≃ 66% with a reaction rate of ≃ 0.003 min^{-1}, for membranes without zeolites after 300 minutes. The conjugation of these factors make these membranes suitable for photocatalytic degradation of micropollutants.

RESUMO

Vários poluentes orgânicos surgem na água como consequência do excessivo uso de químicos gerados com o desenvolvimento tecnológico. Estes poluentes constituem um potencial risco para o ecossistema e saúde humana. Além disso, são extremamente resistentes a processos de degradação biológica e estações de tratamento de águas residuais e água potável, causando a sua acumulação no meio aquático. Neste sentido, os Processos de Oxidação Avançados surgem como uma possível solução, em particular, a fotocatálise heterogénea com semicondutores. O principal objetivo deste estudo foi avaliar a eficácia da fotocatálise com dióxido de titânio imobilizado para a remoção de poluentes de águas residuais. Assim, membranas de poli(fluoreto de divinilideno-trifluoretileno) com 8% wt. de nanopartículas de TiO_2 P25 foram produzidas por *solvent casting*, com e sem a implementação de zeólitos (NaY) de modo a melhorar a molhabilidade, caracterizadas e aplicadas na degradação fotocatalítica de quatro micropoluentes: o corante catiónico Azul de metileno, o antíbiótico Ciprofloxacina, o anti-inflamatório Ibuprofeno e o percursor plástico Bisfenol A. Todas as membranas produzidas possuem uma estrutura porosa, com poros interconectados e um grau de porosidade de cerca de 70%, com tamanho de poros entre os 30 e os 80 μm. Os compósitos apresentam as bandas de absorção características da fase β do PVDF e mostram uma estrutura polimérica intacta, mesmo depois de quatro utilizações. As membranas com TiO_2 e zeólitos são mais hidrofílicas do que a membrana pura. A presença de nanopartículas de TiO_2 modifica a natureza hidrofóbica das membranas após sujeitas a luz ultra-violeta, assim como a inclusão de zeólitos. Na primeira utilização, a membrana com zeólitos degradou Azul de metileno com maior eficiência, ≃ 98% em 300 minutos, com uma velocidade de degradação de ≃ 0.044 min^{-1}. A membrana sem zeólitos degradou Ciprofloxacina com mais eficiência, 93% em 300 minutos, com uma velocidade de degradação de ≃ 0.010 min^{-1}. O Bisfenol A não foi degradado e o Ibuprofeno pareceu gerar sub-produtos aquando da reação. Na primeira utilização, o ibuprofeno degradou ≃ 18 e ≃ 48% em 300 minutos e bisfenol A degradou ≃ 7 e ≃ 3% em 300 minutos, usando membranas com e sem zeólitos, respetivamente. De uma forma geral, a reutilização das membranas mostrou pouca ou nenhuma perda de eficiência após quatro degradações de Azul de metileno, e um ligeiro aumento na de Ciprofloxacina, ≃ 98% com uma velocidade de reação de ≃ 0.015 min^{-1}, e de Ibuprofeno, ≃ 66% com uma velocidade de reação de ≃ 0.003 min^{-1}, para membranas sem zeólitos após 300 minutos. A conjugação destes fatores faz destas membranas apropriadas para a degradação fotocatalítica de micropoluentes.

TABLE OF CONTENTS

GLOSSARY OF ABBREVIATIONS

AOPs	Advanced oxidation processes
BPA	Bisphenol A
CB	Conduction band
CIP	Ciprofloxacin
COD	Chemical oxygen demand
DLS	Dynamic light scattering
DMF	Dimethylformamide
DWTPs	Drinking water treatment plants
FTIR	Fourier transform infrared spectroscopy
HPLC	High Performance Liquid Chromatography
IBP	Ibuprofen
MB	Methylene blue
MS	Mass Spectroscopy
P(VDF-TrFE)	Poly(vinylidene difluoride–trifluoroethylene)
PVC	Poly(vinyl chloride)
PVDF	Poly(vinylidene difluoride)
SEM	Scanning electron microscope
UV	Ultraviolet
VB	Valence band
WWTPs	Wastewater treatment plants
XRD	X-ray diffraction
ZP	Zeta potential

LIST OF FIGURES

LIST OF TABLES

1. INTRODUCTION

In this chapter, the problem is briefly framed and described in the scope of this work. Different approaches are presented and discussed, as are the motivation and objectives. Lastly, the structure of the dissertation is presented, followed by the author's scientific contribution.

1.1. THE PROBLEMATIC OF POLLUTION

The development of technology and the extensive use of chemicals in agriculture results in a shortage and demand for clean water sources worldwide. Organic pollutants in water are a major concern, forcing for the urgent need to develop highly efficient low-cost advanced water treatment technologies [1]–[4]. Anthropogenic sources can introduce these compounds into the environment, constituting a potential risk for the ecosystem [5]. Pharmaceuticals, for example, are excreted into the environment, entering in the sewer network and reaching the wastewater treatment plants (WWTPs) and ultimately the drinking water treatment plants (DWTPs), which are both not designed for their removal [6], [7]. As the sludge that is produced in WWTPs can be applied in soil fertilization, the same as manure, pharmaceuticals will reach the soil. Contamination can also occur through the release and disposal of unused/expired drugs discharged into the sewage network or deposited in landfills, excreted urine, waste effluents from manufacture or accidental spills during manufacturing or distribution [5].

The presence, variety, toxicity and persistence of organic compounds in wastewater effluents can directly impact the health of ecosystems, presenting a threat to humans through contamination of drinking water supplies [8]. Around 4 billion people worldwide are estimated to experience little or no access to clean and sanitised water supply, and millions of people die of severe waterborne diseases annually [9]. These numbers are expected to grow even more in the near future, as water contamination increases due to the continued discharge of pollutants and contaminants into the natural water cycle [3], [10]–[12].

Micropollutants are organic substances that occur in the water in concentrations of a few nanograms/micrograms per litre and, even at such low concentrations, can affect fundamental biochemical processes in nature. These include, but are not limited to, active pharmaceutical ingredients, compounds with biocidal properties, food additives, cosmetics ingredients, detergents and hormones [6]. Many of these micropollutants are potentially toxic and harmful for human life and other living organisms. On the other hand, the large amount of recalcitrant pollutants in water becomes hard to deal with by conventional water treatment

processes. Additionally, they have been a worldwide concern due to the increasing environmental awareness and legislations [1], [3], [13], [14]. These compounds are extremely resistant to biological degradation processes, which causes their accumulation in the environment, and at the same time require more sophisticated tools for their removal [14].

In response to yield more viable water resources, various practical strategies and solutions have been adopted, such as storing storm and rain water for daily activities. However, these present only short-term solutions, making the effective removal of micropollutants and recycling wastewater a strategic approach in a water-scarce environment in the long run [3], [8]. As a consequence, substantial efforts in developing a suitable treatment processes to easily destroy these organic contaminants have been made, with emphasis on Advanced Oxidation Processes (AOPs) [8], [14].

Ciprofloxacin hydrochloride (CIP), an antibiotic, was first patented in 1983. This chemical has been used as both a treatment and prophylactic regimen against several infections. CIP is used in the treatment of infections, respiratory infections, urinary tract infections, typhoid fever, some sexually transmitted diseases and septicaemia. It is effective against organisms that may contribute to infectious diarrhoea, is utilized in antibacterial therapy and has also been utilized as a secondary agent in the treatment for tuberculosis [15]. Antibiotics similar to CIP, when disposed without regard, are suspected to be responsible for strengthening the resistance of microorganisms, causing serious issues of public health, increasing the difficulty in treating pathologies and causing the imbalance of microbial ecosystems [5], [14], [16]. Even released at low concentrations, the accumulation and persistence of antibiotics in the environment can produce harmful effects, either in aquatic or terrestrial ecosystems [5].

Ibuprofen (IBP) is a nonsteroidal anti-inflammatory drug used in pain and inflammation treatments and fever reduction. Patented in 1961, it is used for analgesic, antipyretic and anti-inflammatory purposes. Ibuprofen is highly soluble in water and has low volatility, suggesting a high mobility in the aquatic environment. Although not as persistent as many other chemicals, it is a commonly detected chemical of the pharmaceutical and personal care products in the environment. IBP undergoes photo degradation with exposure to sunlight, although its degradation products can affect the aquatic environments [15].

Bisphenol A (BPA) is a raw material used in the production of polycarbonate (PC) plastics and epoxy resin. First synthesized in 1891, it is one of the most commonly used industrial chemical in the world, as PC is widely used in food storage containers, such as water

and baby bottles, eyeglass lenses, water bottles, and consumer electronics. Epoxy resin is used as a food-contact surface coating for cans, etc. [15], [17], [18]. Krishnan et *al.* [19] and Witorsch [20] have identified safety uncertainty of BPA. The widespread presence of phenols in wastewater and its associated environmental hazards has heightened concern over public health [8], [17]. BPA in particular was shown to cause neurological and behavioural effects in early stages of development in rodents, with the possibility of affecting the reproductive system in humans [17].

1.1.1. WATER TREATMENTS

Some arid and semi-arid areas with abundant sunlight, low rainfall and long-term droughts have difficulty to seek viable water resources [3], [14]. Because wastewater from treatment plants originated from agricultural and industrial activities constitute one of the largest possible water resources, its reuse could counterweight the problem with a cleaner water supply. Recycling wastewater is usually associated with the presence of suspended solids, health-threat coliforms and soluble refractory organic compounds, becoming difficult and expensive to treat [3]. Thus, the necessity for further research on the removal of traced contaminants to minimise their accumulation [8].

In order to prevent environmental contamination through water sources, numerous processes able to degrade/remove micropollutants have been studied, evaluated and compared [5]. Attention is given on methods used in WWTPs since some pollutants usually exit secondary treatment unaffected and, therefore, need to be treated in subsequent stages [14].

In Figure 1 the most studied methods for water treatment between the years 2000 and 2010 can be observed [5], as well as the extent of research. The later data was acquired by means of the search engine from the website https://apps.webofknowledge.com, using the "treatment method's name" with the "water treatment" tag between the mentioned period.

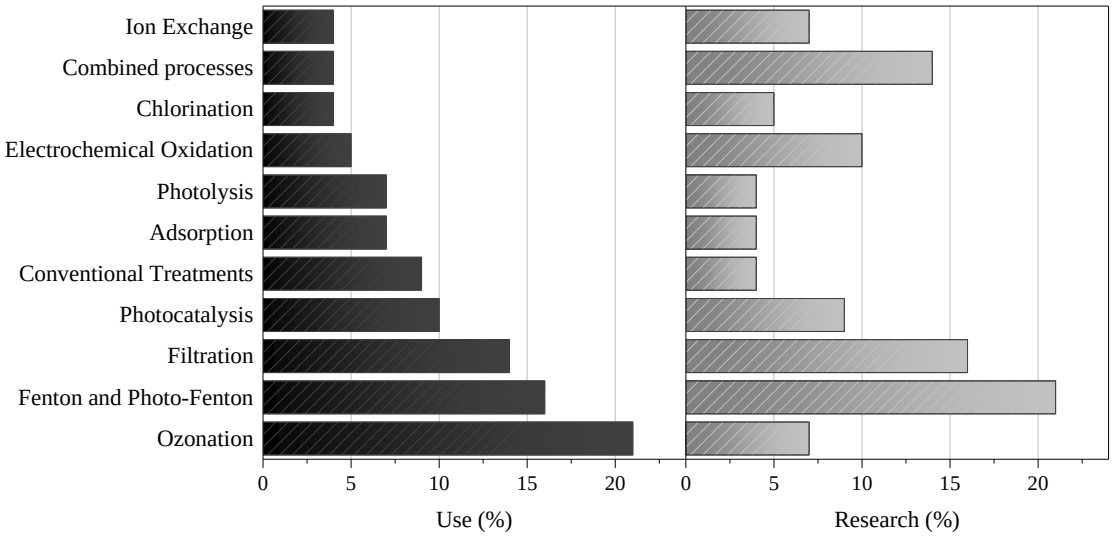

Figure 1 – Diagrams of most studied methods for water treatment between the years 2000 and 2010 (black) and most researched methods between the years 2000 and 2010 (gray). Adapted from **[5]**.

Processes such as filtration and coagulation/flocculation/sedimentation are the most used in conventional WWTPs. These are techniques which require subsequent treatment to remove the pollutants from the effluents. Due to the low efficiencies of these methodologies and the occasional inability of their use, new alternatives have emerged [5], [21]–[25]. Currently available wastewater treatment technologies include activated carbon adsorption and chemical coagulation, membrane filtration, sedimentation and ion exchange on synthetic adsorbent resins, which do not completely eliminate or destroy the pollutants present in water [3], [10], [26]. These technologies have high operating costs and could generate toxic secondary pollutants during the treatment [27], requiring additional steps and cost [3], [8]. Other techniques include chemical oxidation and biodegradation, liquid extraction and membrane techniques, among others. The application of these methods depend mainly upon pollutant concentration in the effluent and cost of the process. Combination of different processes for higher or total mineralization of the pollutant may be also a strategy to deal with the drawbacks of each method [5].

Adsorption is widely used in industry for the removal of organic contaminants, but the contaminant is transferred from the liquid to a solid phase, this produces a new solid residue with the contaminant and should be subsequently treated [5]. In filtration processes, the contaminants are retained in the pressurized side of the membrane while the clean effluent passes through to the other side. This process has the disadvantage of not degrading the contaminant, but concentrating it in the solid phase, generating a new waste. So far, these techniques have been mostly used in combination with others [5]. Ion exchange systems have

been used to improve water quality, though it is rarely used for antibiotics removal [5]. Chlorination is widely used as a disinfectant. However, it generates mutagenic and/or carcinogenic by-products. This has led to the rapid research and development in the field of AOPs as an innovative water treatment technology [3], [5], [28], [29].

1.1.2. ADVANCED OXIDATION PROCESSES

AOPs are based on the generation of highly reactive species (*i.e.* H_2O_2, $^{\bullet}OH$, O_2 and O_3) that mineralize organic compounds, water pathogens and generated by-products [3], [8]. Over the last 30 years, research and development for AOPs has been immense [14], [30]. These processes are mainly based on the generation and reaction of hydroxyl radicals (OH radicals or $^{\bullet}OH$), as they are more reactive than the other oxidative species also used in water and wastewater treatment [31]. AOPs are divided in homogeneous degradations, in which the catalyst is in the same phase as the reactants, and heterogeneous degradations, that occurs at the interface of two phases, usually solid-solution or solid-gas. Some of these AOPs include treatments such as ozonation, photolysis, Fenton oxidation, electrochemical oxidation and heterogeneous photocatalysis (semiconductor photocatalysis) [5], [14]. Nowadays, the most tested methodologies are ozonation, Fenton/photo-Fenton and semiconductor photocatalysis [5], as evidenced by Figure 1. The most common area of application for AOPs is water and wastewater treatment, though applications also include groundwater treatment, soil remediation, municipal wastewater sludge conditioning, production of ultrapure water and volatile organic compounds treatment and odour control [14], [30]. Moreover, the concept of applying AOPs as a phase of pre-treatment in order to enhance biodegradability and reduce toxicity, conjugated with biological post-treatment, has gained a lot of attention over the past several years [30]. Table 1 shows some of the most studied AOPs, with a few advantages and disadvantages. AOPs may also be coupled with other physicochemical and biological processes, either as pre-treatment stage or post-treatment. Process coupling can substantially improve treatment efficiencies [14].

Table 1 – Overview of the most used AOPs.

Processes	Advantages	Disadvantages	References
Ozonation	• Applied when the flow rate and/or composition of the effluents are fluctuating; • Highly efficient.	• High cost of equipment and maintenance; • High energy required; • Temperature and pH-dependent; • Mass transfer limitations; • Low mineralisation; • Eco-toxicity remains or increases.	[5], [28], [32]
Fenton and Photo-Fenton	• Not energy intensive; • No off-gas treatment required; • Use of solar radiation; • Low-cost and environmentally safe reagents; • Easy to handle and operate; • Suitable to treat hospital or pharmaceuticals manufacturing effluents; • Less toxic effluents, ready for biological post-treatment.	• No full scale application; • Requires iron extraction system; • Narrow pH range of operation; • Catalyst recovery; • Decrease in efficiency if an excess of hydrogen peroxide is used; • Applicable only to matrices with low concentrations.	[5], [28], [32]–[34]
Photolysis	• Enhanced when combined with hydrogen peroxide; • Enhanced by low concentrations.	• Limited to photo-sensitive compounds; • Higher toxicity than the original effluent; • Limited to low COD concentrations.	[35]
Electrochemical oxidation processes	• Suitable for high concentrations of pollutants and COD; • Effective, versatile, cost-effective, easy and clean; • Chemical and electrochemically stable; • Good conductivity; • High efficiency.	• Limited to small flow rates; • High operating costs; • Depends upon electrode material, experimental conditions and electrolyte composition; • Temperature, organic concentration and pH-dependent; • Toxic by-products.	[29], [36]
Phocatalysis	• Effective and efficient; • Inexpensive; • Environmental friendly; • Economic and ecologic light source; • Can be performed at higher wavelength than other UV AOPs; • No off-gas treatment required.	• Low quantum efficiency; • Production of toxic products possible; • No full-scale applications; • Pre-treatment necessary; • Separation required in a slurry reactor; • Temperature, low COD and pH-dependent.	[3], [28], [37]–[40]

Among these AOPs, heterogeneous photocatalytic combines a semiconductor photocatalyst, an energetic radiation source and an oxidizing agent [8]. Other AOPs using H_2O_2

with ozone (O_3), H_2O_2 with UV radiation or O_3 with UV, are strongly inhibited by the presence of bicarbonate ions. These processes occur in homogeneous solutions, in which the HCO_3^- ions effectively scavenge the •OH radicals, occurring mainly at the particle surface and not in the solution, which is a clear disadvantage toward photocatalysis [41].

1.1.3. PHOTOCATALYSIS

Semiconductor photocatalysis started after researchers discovered that illuminated semiconductor particles were able to catalyse a wide range of redox reactions of organic substrates [5]. Photocatalytic water treatments use different nano-scaled semiconductor materials as catalysts, such as TiO_2, ZnO, Fe_2O_3, CdS, GaP, WO_3, $SrTiO_3$ and ZnS [42], [42]–[45]. These materials are capable of transforming the energy of absorbed photons (through either UV or, in very specific cases, visible light) into charge carriers. This results in electrons (e^-) and holes (h^+) that diffuse to the surface of the semiconductor, reacting with the water, oxygen and the pollutant adsorbed to the surface of the catalyst in an aqueous media [31], [46], [47].

Research has escalated over the last years (Figure 2). These results reflect citations to source items indexed within Web of Science Core Collection and over 3182 total results and 93812 total times cited.

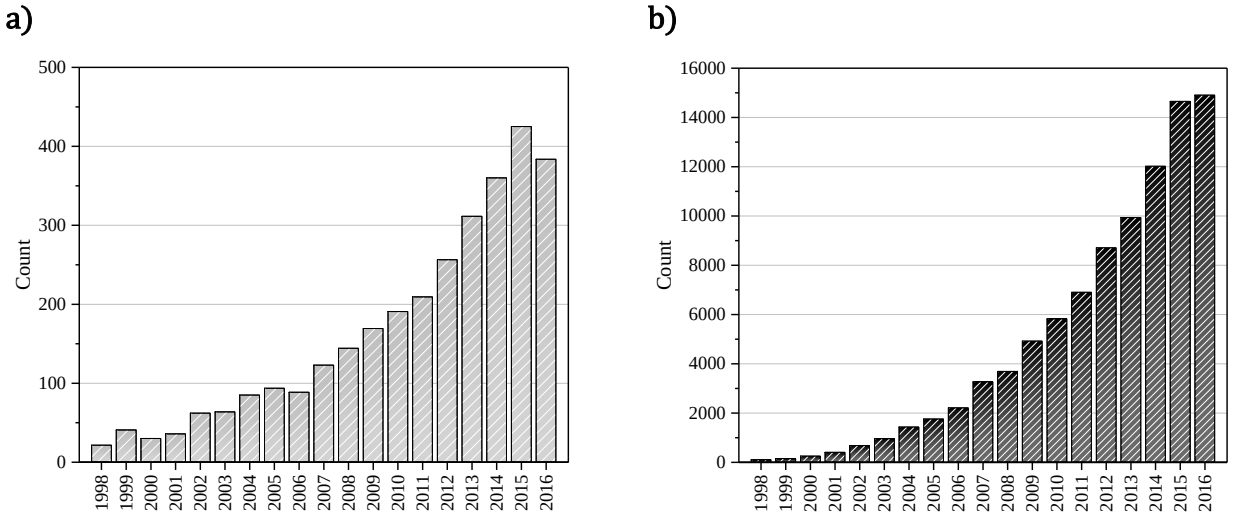

Figure 2 – a) Published items in each year; **b)** citations in each year. Based on results from web of science, with "water treatment" and "photocatalysis" as search topic.

A large number of researches in water treatment have been applying semiconductor photocatalysts due to their effectiveness in degrading a wide range of recalcitrant organics into readily biodegradable compounds, eventually mineralizing them to harmless carbon dioxide, water and inorganic compounds [2], [3], [8], [37]. Another advantage is that the catalyst itself is inexpensive and photo-chemically stable, and the commercial diversity of its crystalline forms and particle characteristics [14]. Being an environmental friendly chemical technique, photocatalysis presents breakthroughs that address environmental problems such as pollutant degradation, heavy metal cation reduction, arsenic (As) and Chromium (Cr(VI)) removal, offering great potential in the degradation of different organic contaminants in wastewater [1], [44]. Nevertheless, although the photocatalytic oxidation method is a promising route for the treatment of wastewater, its major drawbacks are the low quantum efficiency due to the inefficiency of visible light harvesting, photoreactor design, recovery and reuse of the photocatalyst, production of toxic by-products and possible catalyst deactivation [3], [8]. The photocatalytic degradation may also be dependent upon the solution's pH, catalyst type and concentration, substrate type, light intensity, composition of the wastewater and pollutants concentration [8].

Biological treatment is one of the most recent applications for heterogeneous photocatalytic technology, where the non-biodegradable compounds in wastewater can be turned into biodegradable compounds, reducing the retention time in biological treatment stages. Photocatalysis may also replace chemical disinfestation methods due to its efficiency against various microorganisms [3].

Consequently, given the above mentioned needs, and in order to choose a sustainable and efficient technique for the treatment of wastewater, it is mandatory to understand the impacts of various parameters on photocatalytic degradation efficiency [8].

1.1.4.1. Photocatalytic Materials

A semiconductor is characterized by its valence and conduction bands. By absorbing photons with energy equal or higher than its band gap (energy between the valence and the conduction band), an electron is promoted from the valence to the conduction band, generating a hole in the valence band [5]. Several semiconductors have been studied, among them, Titanium Dioxide (TiO_2), Zinc Oxide (ZnO) and Cadmium sulphide (CdS) are the three most commonly

used in wastewater decontamination, usually in suspension systems, due to their unique optical properties, low cost, availability, high activity, chemical and thermal stability, chemical resistance to breakdown and strong mechanical properties [14], [38], [45].

Among the semiconductor catalysts, TiO_2 has been well known for its great potential for applications in environmental purification, decomposition of carbonic acid gas and generation of hydrogen gas. With its commercial production dating back to 1923, TiO_2 is obtainable from a variety of ores and is mainly applied in pigments, adsorbents, catalysts supports, filters, coatings, photoconductors and dielectric materials [48]. The application of TiO_2 in the photocatalytic degradation of organic pollutants in water has combined the inexpensiveness of TiO_2 with the inexhaustible UV, emerging as a promising new route for water treatment [1]–[3], [5], [8], [13], [49]–[51]. Being the most active photocatalyst under the photon energy of $300\ nm < \lambda < 390\ nm$, TiO_2 remains stable even after the repeated catalytic cycles, unlike Cds and ZnO, that is degraded along to produce toxic by-products[3], [9], [51]. Nonetheless, TiO_2 has a few liabilities, such as the difficulty and high cost for post separation of the used nanoparticles from the treated affluent, low UV utilization efficiency, usually associated to the slurry reactor system, and relatively high recombination rate of the electron/hole pairs [50], [52]. Bulk TiO_2 has three main crystalline phases: rutile, anatase and brookite, among which rutile and anatase are the most active. Both anatase and rutile have a tetragonal structure, with rutile being a high-temperature stable phase, and having an optical energy band gap of 3.2 eV (380 nm) and 3.0 eV (415 nm) for anatase and rutile, respectively [27], [47], [48], [53].

Specifically, and to this date, Degussa P25 TiO_2 is the most widely applied commercial photocatalyst in the experimental research of water treatment. P25 contains 75% of anatase and 25% of rutile phases with a specific Brunauer, Emmett and Teller (BET) surface area of $50 m^2 g^{-1}$ and a primary particle size of 20 nm [3], [8], [14]. This catalyst is used as a standard reference under different photo activity conditions [3]. Comparing with other photocatalysts, the photocatalytic activity of Degussa P25 was reported to be higher owing to the slow recombination between electrons and holes [8]. Although nanoscale TiO_2 shows considerable improvement in terms of physical and chemical properties compared to the bulk TiO_2 catalysts, its smaller particle size and morphology remains the main problem when applied in larger scale water treatment systems, due to the difficulty of building an effective UV reactor system with controlled conditions and retention [3], [54].

A good material that presents interesting characteristics, likewise making it widely used, is ZnO due to its wide band gap (3.4 eV) and good optoelectronic, catalytic and photochemical

properties. Although, so far, it still possesses a fast recombination rate of photo generated electrons/holes pairs [3], [51]. Overall, ZnO shows good performance as a photocatalyst, decomposing diverse organic contaminants more efficiently than TiO_2 in an aqueous solution [51]. Also popular is CdS due to its shorter excitation wavelength ($\simeq$ 495 nm) and a good absorption of sun light because of its smaller band-gap (2.4 eV) [53]. Nevertheless, the fact that ZnO and CdS suffer from photo-dissolution when in water, causing them to decompose into by-products that are toxic to the environment, is considered the main hurdle that lowers its photocatalytic efficiency [38], [55].

Given the arguments specified above, TiO_2 seems to be the most advantageous material for photocatalytic applications.

1.1.4.2. Photocatalytic Mechanism

Despite adsorption being a technique used for water treatment, the term adsorption is commonly used to describe the tendency that species in fluid phase have to adhere to a solid surface. Because the potential energy of the solid is low, the force field creates a region near the solid's surface that results in the increase of molecular density [5]. This fact is important in the sense that, in a photocatalytic reaction, the photo-induced reactions take place at the surface of a catalyst [1]. The primary events occurring on an illuminated TiO_2 particle, during the photocatalytic degradation of organic pollutants are summarized in Figure 3.

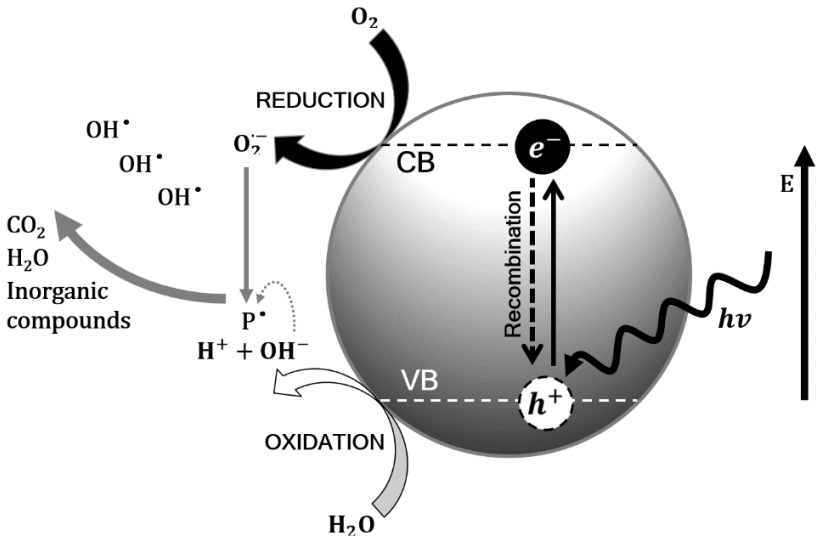

Figure 3 – Scheme of the photocatalysis mechanism on a semiconductor particle with the presence of a water pollutant (P) and light irradiation.

Firstly, the photocatalyst particle absorbs radiation of energy greater than or equal to its band gap energy, which generates electron–hole pairs (Equation (1)). Although most of these charge carriers suffer from recombination and produce thermal energy, part of the photo-generated electrons and holes can rapidly migrate to the surface of catalyst particle, where they are ultimately trapped and able to undergo a series of oxidative and reductive reactions with the adsorbed species at the surface of the particle. The trapped holes in the valence band can react with either the organic contaminant, adsorbed to the surface of the particle, and produce organic radical cations (Equation (2)), or chemisorbed OH^- or H_2O to produce $^{\bullet}OH$ radicals (Equation (3)). Similarly, the electrons in the conduction band are scavenged by O_2, yielding superoxide radical anions $O_2^{\bullet-}$ (Equation (4)), which, in turn, react with protons to form peroxide radicals. Ultimately, $^{\bullet}OH$ radicals derive from both oxidation chemisorbed OH^- or H_2O by holes and reduction dissolved O_2 by electrons [1], [14], [56].

$$TiO_2 \xrightarrow{h\nu} TiO_2(h^+ + e^-) \quad (1)$$

$$h^+ + OH^- \rightarrow HO^{\bullet}_{ad} \quad (2)$$

$$h^+ + H_2O \rightarrow HO^{\bullet} + H^+ \quad (3)$$

$$e^- + O_2 \rightarrow O_2^{\bullet-} \quad (4)$$

This mechanism can be assigned to overall heterogeneous catalysis reactions and can be used for the application of the hydrogen generation and pollutant decomposition [1], [31]. The optical absorption properties and catalytic performances of a semiconductor photocatalyst strongly depend on their microstructures (surface area, crystal phase and crystal plane) [1]. Moreover, this process can be driven by UV or visible light [1], [8], [44]. The sun produces 0.2 to 0.3 mol photons $m^{-2}h^{-1}$ in the range of 300–400 nm, with a typical UV flux of 20–30 W m^2, near the Earth's surface, signalling sunlight as an economic and ecologic light source [8].

There are typically two types of photoreactors described in the literature. A slurry photoreactor refers to a catalyst which is suspended in the water to be treated, while the immobilised photoreactor has the catalyst attached to a substrate which is immersed in the water to be treated [49].

1.1.4.3. PHOTOCATALYSTS WITH SUSPENDED CATALYSTS

Photocatalytic reactions in suspension involves photocatalysts suspended in an aqueous solution. Catalyst concentration, light wavelength and intensity, the solution pH, the addition of H_2O_2 as an extra oxidant (in order to promote reactions), and the water matrix are important parameters that strongly affect its performance [14].

Although photocatalytic reactions using nanoparticles present superior photocatalytic activity because of nanoparticles having high surface area, good dispersion and abundant active sites, the main hurdle of photocatalysis in suspension is in removing, recovering and/or recycling the photocatalyst for further uses. Because photocatalysts are usually fabricated as nano-sized particles, they are difficult to retain and separate from the reaction solution. To avoid losing the catalyst particles, which will decrease the efficiency of the process and also lead to the introduction of TiO_2 as a new pollutant of contamination in the treated water, and to accelerate powder separation, certain additional procedures must be adopted, resulting in slow additional treatment costs [1], [3], [14], [49], [57]. Filtration is one of the used recovery methods. Microfiltration, for example, was reported to recover the catalyst particles for reuse and, while controlling the pH close to the isoelectric point in order to induce coagulation and ease separation process [3], [9]. Non-reusable photocatalytic materials considerably increase the operating cost, significantly limiting actual applications in wastewater treatment [1], [49].

Although a large surface area-to-volume ratio promotes efficiency in terms of charge separation and adsorption, the small particle size and large surface energy of TiO_2 makes it a target for agglomeration. Agglomeration of the particles is highly disadvantageous in terms of particles size preservation, surface-area reduction and its reusable lifespan [13], [58].

1.2. MOTIVATION AND OBJECTIVES

Driven by the problems previously presented, the motivation of the present work is the development and optimization of a titanium dioxide nanoparticles immobilization method, aiming to its subsequent implementation in grand scale systems for wastewater treatment.

Although membrane processes are already being used, it does not enable the degradation of the contaminants, but only transfers them onto the membrane [5]. In this sense, the development of a membrane which can be used and re-used in water treatment, without the concerns of contamination or the need for an additional cleaning process, is of the utmost importance. This is where photocatalysis comes as a good process to pair up with nanocomposite membranes, by incorporating stable, cheap and environmental friendly TiO_2 nanoparticles, into the structure of a polymeric membrane.

The main objectives of the presented work is to produce and characterize photocatalytic membranes, composed of P(VDF-TrFE), with immobilized TiO_2 nanoparticles. The efficiency of the proposed membranes will be evaluated on the photocatalytic degradation of different model micropollutants, in comparison with photocatalytic degradation processes with TiO_2 in suspension. Moreover, reusability of the membranes will also attempted and studied, in relation to changes in degradation efficiency and loss of immobilized nanoparticles. The proposed materials will be characterized, before and after use, by various techniques.

This work was conducted as a collaboration between University of Minho, Electroactive Smart Materials group (ESM), and the Technical University of Dresden, Materials Science and Nanotechnology group in the scope of an ERASMUS Placement program.

1.3. Structure of the Dissertation

The dissertation is divided into the following chapters.

Chapter 1 – Introduction

This chapter describes the main problem in relation to this work, as is the motivation and main objectives. Lastly, the planning of this work is presented.

Chapter 2 – State of the Art

In this section, the main frame upon which settles this work is presented and briefly discussed, giving an insight on how and why this study was conducted.

Chapter 3 – Materials and Methods

The first part of this chapter describes all the used materials for this study. The second part describes the methods used to characterize and apply the proposed materials for photocatalytic processes for the removal of model micropollutants.

Chapter 4 – Results and Discussion

In this chapter, the results of material synthesis, characterization and application (as described in chapter 3) are presented and thoroughly discussed, as well as compared with other works.

Chapter 5 – Conclusion and Future Perspectives

In this chapter, some conclusions and final considerations are presented about this and other related works. Some suggestions are also presented as a way to help develop future applications.

1.4. CONTRIBUTION

This work gave way to a presentation in the form of a Poster intituled "Approaches for enhanced photocatalytic activity", with co-authors H. Mora, J. Ribeiro, B. Magalhães, P.M. Martins, Sara Teixeira, Klaus Kühn, Gianaurelio Cuniberti, S. Lanceros-Méndez, in the 20th National Conference of Physics and 26th Iberian Meeting for the Teaching of Physics, in University of Minho, Portugal, from 8 to 10 of September 2016. A paper is under preparation: "*Reusability of TiO_2/PVDF-TrFE membranes on degradation of micropollutants*", with co-authors J. Ribeiro, P.M. Martins, S. Teixeira, L. Pereira, Klaus Kühn, Gianaurelio Cuniberti, S. Lanceros-Méndez.

2. State of the Art

This Chapter corresponds to a study of the area of immobilized photocatalytic systems, their advantages and disadvantages, substrate materials and techniques. As an alternative to counter certain limitations, emphasis is given on membranes of poly(vinylidene difluoride−trifluoroethylene), produced by solvent casting, as an easy method to obtain porous structures able to immobilise TiO_2 nanoparticles successfully.

2.1. IMMOBILIZED TiO_2 NANOPARTICLES

In order to overcome the problems brought by suspension systems, semiconductors immobilised onto a solid substrate have been studied and performed. Ideally, the support should allow a strong adherence to the catalyst, high specific surface area, strong adsorption affinity towards the contaminants and a catalyst reactivity not negatively affected by the attachment process [5], [58]. Despite resulting in a considerable reduction of surface area, thus lowering the photocatalytic degradation efficiency [1], [5], [14], this methodology seems to be promising in the efficient removal of micropollutants from effluents with low concentrations of organic matter, such as rivers, groundwater and drinking water [5], [59]. Immobilising photocatalysts also reduces the amount of catalyst active sites and suffers from mass transfer limitations and the reduced contact with light [3], [5], [14].

Notwithstanding, studies on immobilised systems report comparable photocatalytic performance in relation to systems employing nano/micro-particles in suspension, which represents a step in the right direction for photocatalytic applications [13]. Even with the developed of immobilisation procedures over the past few decades, this technology has never been practically applied in water/wastewater treatment [5], [49]. There are also several factors limiting the choice of a suitable and an efficient immobilisation procedure, particularly at economical levels, such as the immobilization methods, light source (artificial [38], [46], [60] or solar energy [9], [18]) and micropollutant type (organics [59], [61], [62] or dyes [49], [60], [63]). Consequently, comes the need to design and fabricate high-quality photocatalysts with enhanced photocatalytic activities and stabilities and the desired morphologies [1].

2.1.1. IMMOBILIZATION SUBSTRATES

Several substrates have been tested as a support, and offer prospects for TiO_2 immobilization for the degradation of water pollutants, including silica, glass [64] and graphene [42], [65]–[67], known for their transparency, polymers [68]–[71], activated carbon, which are porous with a high specific surface area, clay [51], [72], which have high adsorption and cost effectiveness, metals, sand, paper, quartz, wool, pyrex, cement beads and steel mesh, etc. [1], [5], [45], [73].

Overall operating performance with immobilized TiO_2 is dependent upon support type, pore size and blockage, regeneration or back-washing and , in some cases, fouling [3]. Yu *et. al.* [54] conducted a study in which various materials and immobilization processes were analysed for TiO_2 nanoparticles. The use of nanofibers, nanowires or nanorods solves the mass transfer limitation due to their thin longitudinal morphology. These fibre membranes show high pollutant removal rate, nevertheless, the use of less durable materials such as glass or woven cloths may lead to a low durability, with the deposited nanoparticles wearing-off, loss of photocatalytic activity over time and increase pressure drop in the reactor system.

Countless materials and techniques have already been evaluated, some with encouraging results. However, the immobilization of TiO_2 nanoparticles remains a challenge. Many of these substrates lack the conditions required for photocatalytic applications, such as strong adhesion of the nanoparticles to the substrate and catalyst reactivity after its attachment [73].

More recently, attention seems to be growing in regard to polymers such as polyester, polyamide-12, cellulose, high density polyethylene, chitosan and poly(vinylidene fluoride) [71], [73]–[75]. Among the polymer classes, electroactive polymers are one of the most interesting, used as smart materials in various applications, such as sensors, actuators, energy harvesting and as biomaterials in the biomedical field, among others [74]. Among the few polymers presenting piezo, pyro or ferroelectricity, poly(vinylidene fluoride) (PVDF) and its co-polymers have the best electroactive properties, consequently being the material of choice for the increasing number of possible applications [74], [76], [77].

2.1.2. POLY(VINYLIDENE FLUORIDE) AND ITS CO-POLYMERS

This section describes the relevant characteristics and properties of the studied material, P(VDF/TrFE), as a co-polymer of PVDF, and a comparative theoretical study between these materials. Finally, the subsequent studies of the diverse possible applications are presented, while referring to the concepts and definitions of their electroactive properties.

Fluoropolymers are characterized by high chemical inertness, very low surface tension, thermal stability and electrical insulating properties [78]. PVDF is a semi-crystalline fluoropolymer of repeat unit (CH2-CF2-) [74], [78]. Many of the interesting properties of PVDF are related to the strong electrical dipole moment of the PVDF monomer unit, of $5 - 8 \times 10^{-30}$ C m, due to the electronegativity of fluorine atoms in relation to those of hydrogen and carbon atoms. This means that each chain possesses a dipole moment perpendicular to the polymer chain [74], [79]. PVDF and vinylidene co-polymers show a complex structure and can crystallize in five distinct phases, corresponding to different chain conformations [13], [74], [80]. The three most investigated and used PVDF phases are shown in Figure 4.

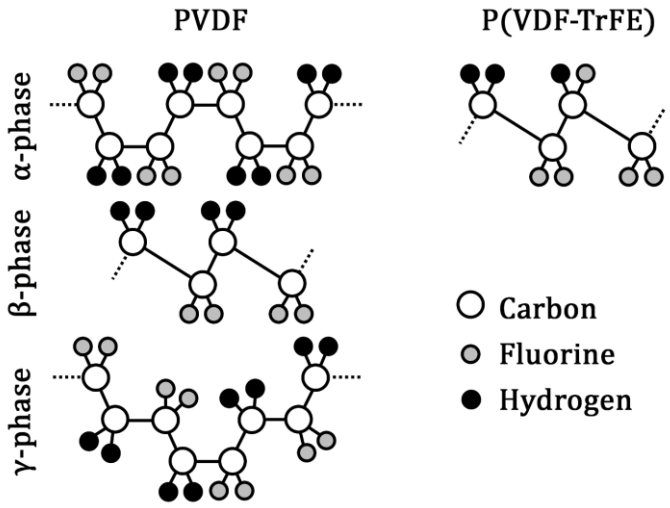

Figure 4 – Schematic representation of the chain conformation of α, β and γ-phases of PVDF and one of its co-polymers, P(VDF-TrFE). Based on **[74]**.

Among the three most investigated PVDF phases, the α-phase presents a nonpolar structure with a TGTG′ chain conformation, while the β- and γ-phases present a polar structure with all-trans planar zigzag TTT and T3GT3G′ chain conformation, respectively. The β-phase has the highest dipolar moment per unit cell (8×10^{-30} C m) when compared to the other two phases [13], [70], [74], [79].

Several co-polymers of PVDF have been developed to improve certain properties and adapt to the increasing technological demands. These include poly(vinylidene difluoride-Trifluoroethylene) (P(VDF-TrFE)), poly(trifluoroethylene chloride) (P(PDF-CTFE)), poly(vinylidene fluoride-co-hexafluoropropene) (P(VDF-HFP)) and poly(vinylidene fluoride-trifluoroethylene-chlorofluoroethylene) (P(VDF-TrFE-CTFE)) [74]. P(VDF-TrFE) is one of the most studied co-polymers and its chain conformation can be observed in Figure 4. Polymer crystalline phase is deeply influenced by the processing technique and conditions or the inclusion of nanoparticles, yet PVDF—TrFE (70:30) crystallizes in the β-phase regardless [13]. This co-polymer possesses a high degree of crystallinity and a high remnant polarization ($\simeq$ 110 mC m^{-2}) when compared with PVDF, giving, in turn, rise to a larger electromechanical coupling factor, k, which translates into a higher efficiency of piezoelectric properties. P(VDF-TrFE) can be produced either in the form of films [79], fibres [81], [82] and membranes with a controlled micro porosity [45], [69]. The physicochemical properties of this fluorinated co-polymer make it suitable for the intended application, as it shows excellent chemical, mechanical, thermal and UV radiation resistance, related to the stable C–F bonds of the polymer chain [45], [74].

In this work, P(VDF-TrFE) was used as a support, due to its microporous structure, which is suitable for TiO_2 nanoparticles immobilization [83], through the production of membranes with controlled porosity and pore size. TiO_2/P(VDF–TrFE) nanocomposite membranes have been previously successfully produced with demonstrated photocatalytic activity in the degradation of methylene blue (MB) [73].

When using polymeric membranes the photocatalytic reaction can take place, not only at the surface of the membrane, but also inside its interconnected pores, enabling the treated water to be continuously discharged without the loss of photocatalyst particles [3]. There is, however, always the risk of technical problems such as the deterioration of the membrane structure, low photocatalytic activity and the loss of deposited TiO_2 over time [3]. Although the reusability of photocatalytic nanocomposites has been previously studied, many failed to fulfil important requirements, as an efficient attachment of the nanoparticles to the support and a production method that does not reduce the efficiency of the catalytic properties, as compared to the suspended form [45].

2.1.3. FABRICATION TECHNIQUES

Numerous techniques have been proposed and employed for the immobilization of photocatalytic nanoparticles onto a polymeric support [49]. Some of these techniques are displayed in Table 2.

Table 2 – List of methods for the fabrication of supports for the immobilization of TiO_2 nanoparticles.

Technique	Type	References
Electrospinning	• Fibrous membrane	[44], [74], [81]–[84]
Spin and dip coating	• Film • Fibres and membranes	[68], [85] [64], [86], [87]
Deposition and sputtering	• Film	[88]–[90]
Solvent Casting	• Film • Porous membrane	[74] [13], [45], [73], [83]

Thin films have the disadvantage of a low surface area and the fact that good fixation of the nanoparticles is not guaranteed [44]. Membrane technology has greatly grown in the last 30 years, not just for water desalination applications, but also for food processing and medical applications [74].

This work will focus on the solvent evaporation method, also known as solvent casting, as it enables the production of membranes with a controlled degree of porosity and pore size. This allows to tailor the microstructure of the polymer for the desired application and to easily recover and reutilize the immobilized catalyst [45], [73], [74]. One of the problems of using P(VDF–TrFE) is its low wettability [73], as a result of its low surface tension, which restricts the interaction between the pollutant and the polymeric substrate, where the TiO_2 nanoparticles are immobilized [73], [78]. In order to overcome that limitation and obtain a well hydrophilic surface, various techniques can be employed, such as coating with nanoparticles, UV irradiation and electron irradiation [91]–[94].

3. MATERIALS AND METHODS

In this section the materials and methods involved in the production, characterization and application of poly(vinylidene difluoride−trifluoroethylene) (P(VDF-TrFE)) membranes will be presented. The process for the fabrication of photocatalytic polymer membranes will be pointed. The materials were characterized and their photocatalytic activity was assessed. Initially, the photocatalytic degradation of micropollutants was performed using the produced nanocomposite membranes. Afterwards, as a means of comparison between the immobilization and the suspension systems, the photocatalytic degradation of the same micropollutants, but with the nanoparticles in solution, was tested.

3.1. MATERIALS

P(VDF–TrFE) was obtained from Solvay 70:30. P25 TiO_2 nanoparticles were supplied by EVONIK industries. Zeolites (NaY) were obtained from Zeolyst International. MB and DMF were supplied from Merck. CIP (98%), IBP (98%) and BPA (99%) were obtained from Sigma-Aldrich. NaOH (97%) was obtained from VWR. MembraPure water was used in all experiments.

3.2. NANOCOMPOSITE MEMBRANE PRODUCTION

The technique of solvent casting used to produce the nanocomposite membranes of P(VDF-TrFE) was performed as follows: 9 mL of N,N-dimethylformamide (DMF) was added to 8% wt. P25 TiO_2 nanoparticles. The solution was then left in ultrasonic bath for 3 hours. After the bath, 1 g of P(VDF-TrFE) was added and the solution was stirred for 2 hours, until complete dissolution. The resulting solution was then poured into a glass Petri dish and left to dry for approximately 4–5 days at room temperature, to allow the DMF solvent to evaporate. After the complete evaporation of the solvent, the final membrane was obtained. The resulting membrane seems smooth at first glance, but it is porous. A brief scheme of the process can be observed in Figure 5.

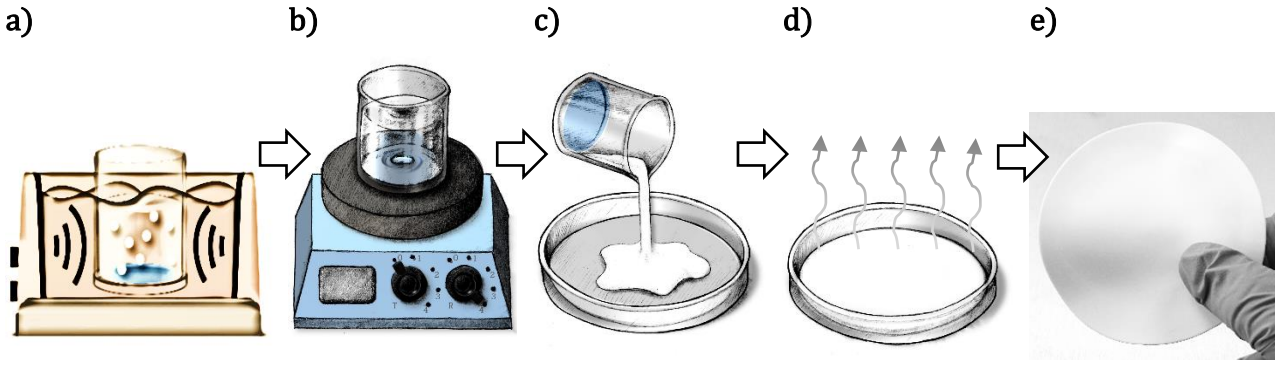

Figure 5 – Representation scheme of the steps involved in the production of nanocomposite membranes through solvent casting; **a)** ultrasonic bath; **b)** magnetic stirring; **c)** pouring on glass petri dish; **d)** solvent evaporation; **e)** membrane after complete evaporation of the solvent.

The wettability of nanocomposite membranes was tailored through the incorporation of zeolites (NaY) into the P(VDF–TrFE) matrix. Zeolites are highly hydrophilic and porous structures, with pores of 5 – 12 Å, making them good adsorbents [73], [91]. In order to mitigate the adsorption limitations instigated by immobilization, zeolites (NaY) were added to some of the nanocomposites. A total of three types of P(VDF-TrFE) composite membranes were prepared. One with 0.087 g (wt. 8%) of $Ti0_2$, one with 0.087 g (wt. 8%) of $Ti0_2$ and 0.030 g (wt. 3%) of NaY, and a third one without TiO_2 or NaY, to serve as control [3].

3.3. CHARACTERIZATION TECHNIQUES

In the following sections, the various techniques used to characterize the P25 TiO_2 nanoparticles, but also the P(VDF-TrFE) membranes, are described. There are two important factors that influence physical properties in a material, that are the crystalline phase and the particle size and can be studied through several techniques [48]. For this, X-Ray Diffraction (XRD), Dynamic Light Scattering (DLS) and Zeta potential (ZP) were used to study the crystalline phases of the TiO_2 nanoparticles, particle size and the electric charge stability relative to its pH, respectively. The membranes were studied using Scanning Electron Microscopy (SEM), Porosimetry, Contact angle and Fourier Transformed Infrared Spectroscopy (FTIR), in relation to their morphology and membrane thickness, their porosity and pore size, wettability and their chemical stability, respectively.

3.3.1. NANOPARTICLES

3.3.1.1. X-RAY DIFFRACTION

Information on the crystalline phases was obtained by XRD. X-rays are high-energy electromagnetic waves and can be generated by the use of sealed tubes, rotating anodes or synchrotron radiation sources. A heated tungsten filament in a vacuum generates electrons that are accelerated through a high potential field and directed toward a target. Firstly, the deceleration of these electrons leads to the emission of X-ray photons. Secondly, by ejecting electrons from the inner shells, the impinged atoms are ionized and, to get a more stable state, electrons from outer shells "jump" into these generated gaps. These two effects induced by the incident electrons lead to the generation of X-rays [48], [70], [95].

All crystalline materials present a diffraction pattern, which are x-rays diffracted by the hkl (Miller index) planes. In a polycrystalline, non-textured material with fine grains, diffraction occurs for each lattice plane and direction that satisfies the Bragg's law in the case of constructive interferences. The cleavage faces of a crystal appear to reflect X-ray beams at certain angles of incidence, as explained by Bragg's Law:

$$n\lambda = 2d_{hkl} \sin\theta \quad (5)$$

with θ being the angle of incidence in degrees, d_{hkl} the distance between atomic layers in a crystal in nm, λ the wavelength of the incident X-ray beam in nm and n the order of diffraction [96]. Figure 6 represents the refracted x-ray in a crystalline matrix.

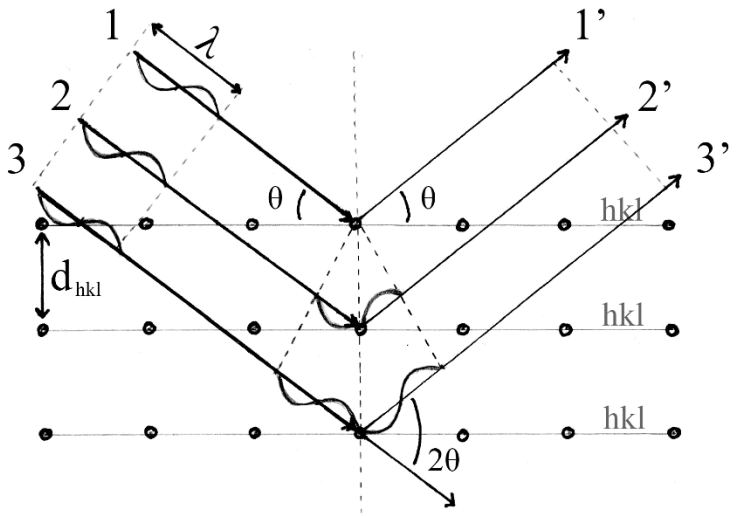

Figure 6 – XRD diagram of reflected x-rays on a crystal structure.

Hard x-rays, with wavelengths below 1 nm, are diffracted by the planes of atoms in a solid, whose spacing is of similar dimensions. Soft x-rays, with wavelengths in the range 1 nm to 10 nm, are more commonly used in x-ray microscopy and are diffracted by structures whose periodicity is several nm. This diffraction is used to determine the atomic structure of solids [96], [97].

To measure the phase content of the TiO_2 nanoparticles used in this work, XRD measurements were performed by a HR-XRD scan diffractometer, operating in the reflection mode with Cu-Kalfa radiation (40 kV, 30 mA) and a diffracted beam monochromator, using a step scan mode with the step (2θ) of 0.02° and 1.25 seconds per step.

3.3.1.2. Dynamic Light Scattering

The average hydrodynamic diameter of the P25 TiO_2 nanoparticles can be measured by DLS. Size is an important factor to define nanoparticles. Even a mixture of particles with different

sizes can be considered a nanomaterial as long as at least 50% of the particles present diameters ≤ 100 nm. As a result, it is important to know the precise size distribution [98]. Typically, a DLS system consists of six main components, which can be seen in Figure 7.

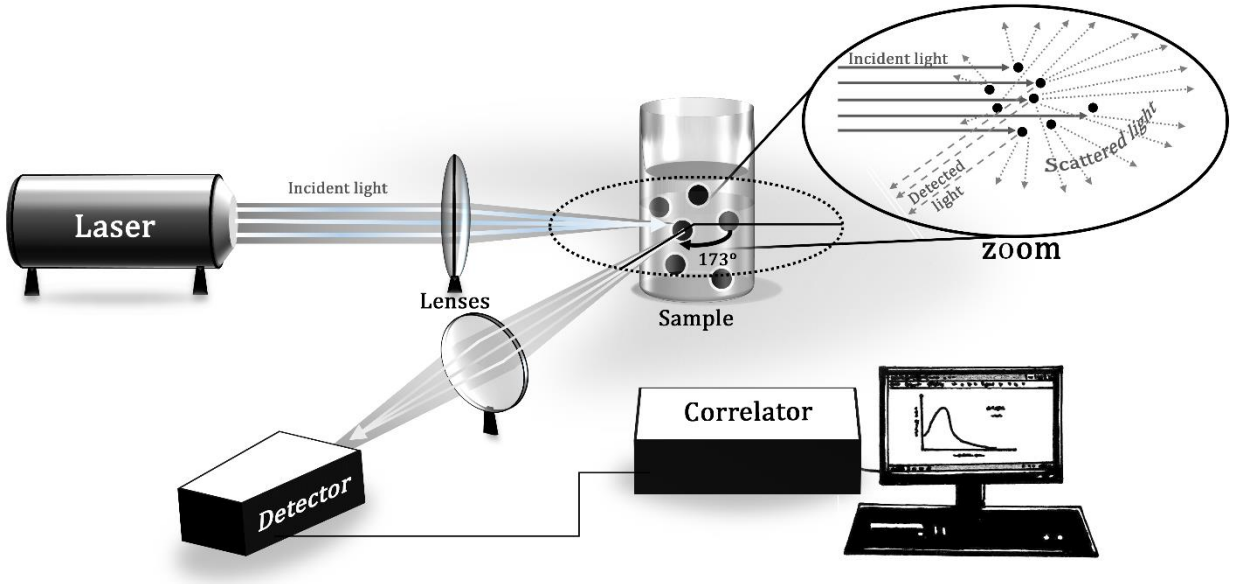

Figure 7 – Schematic of the functionality of DLS.

A laser illuminates the sample particles within a cell, with most of the beam passing straight through the sample, although some is scattered by the particles within the sample. The intensity of the scattered light is measured by a detector placed at any possible angle in relation to the beam, as a particle scatters light in all directions. An attenuator is used to reduce the intensity of the laser, hence reducing the intensity of the scattering, otherwise the detector will become overloaded [99].

The measurements were obtained using a Malvern nano–ZS with a Zetasizer software, which estimates the particle mean hydrodynamic diameter from the intensity distributions (zeta-average), in backscattering mode at 173°, at a room temperature of 25°C. The TiO_2 nanoparticles were dispersed in ultra-pure water, with concentrations of 5, 15 and 35 mg L^{-1}, and the solutions were placed in ultrasonic bath for 2 hours, in order to avoid multi-scattering events. The hydrodynamic diameter was assessed 5 times for each concentration.

3.3.1.3. ZETA POTENTIAL

The electric charges in the periphery of the particles are represented by their zeta potentials (ZPs). After applying an electric field, it is possible to measure the motion of the particles, determining the velocity and direction in which the particles move [41], [100]. ZP, or electrokinetic potential, is the potential at the slipping/shear plane of a colloid particle moving under electric field, as can be observed in Figure 8 [98], [100].

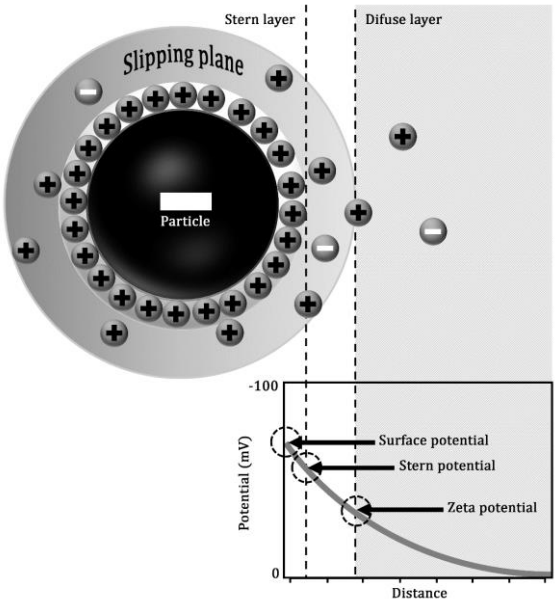

Figure 8 – Schematic representation of the different layers of a suspended particle and respective zeta potential. Based on **[100]**.

The ZP varies with pH, becoming more positive and negative with acidic and basic pHs, respectively. Consequently, a curve of ZP in relation to pH is useful to determine the isoelectric point, *i.e.* , the pH where the ZP becomes zero [98]. The isoelectric point, or point of zero charge for aqueous dispersions, represents both the pH at which an immersed solid oxide electrode would have zero net charge (pH_{pzc}), and the pH resulting in electrically equivalent concentrations of the positive and negative complexes [41], [98].

Colloids are less stable and agglomerate/flocculate when the pH is close to the isoelectric point [98]. The pH dictates the ionization state of the catalyst surface, consequently affecting the extent of organics adsorption and degradation. Particles between 1 and 100 nm are considered stable at ZP > |30| mV [14]. As such, if TiO_2 nanoparticles and the pollutant exhibit opposite charges, they will attract each other, which promotes adsorption. This makes ZP

measurements relevant for photocatalysis applications as the adsorption of molecules depends upon pH [13], [14]. The velocity of a particle in an electric field is commonly referred to as its Electrophoretic mobility, and can be related to the ZP by the Henry equation:

$$U_E = \frac{2\varepsilon z f(\mathrm{ka})}{3\eta} \quad (6)$$

where z is the zeta potential, U_E the electrophoretic mobility, ε the dielectric constant, η the viscosity and $f(\mathrm{ka})$ the Henry's function [100].

The zeta potential was determined using a Malvern nano–Z5 ZEN3600 with a Zetasizer software, at a room temperature of 25°C, a Ha-Ne laser ($\lambda = 633$ nm) and an detection angle of 173° in backscattering mode. These potentials were measured in electrophoretic cells containing the TiO_2 particles in 100 mg L^{-1} ultrapure water solutions with various known pH values of 2, 4, 7, 9 and 12. For this, solutions of HCl (1 M) and NaOH (1 M) can be added to adjust the pH [73]. The average value and standard deviation for each sample was obtained from measurements. The results were obtained using the Smoluchowski theory approximation, $f(\mathrm{ka}) = 1.5$ [100].

3.3.2. Nanocomposite Membrane

Characterization of the nanocomposite membranes before use is crucial to understand their properties and to link with their performance in a specific application and determined conditions. In some cases, the membranes were also studied after use, owing the importance of reutilization and recycling, as a way to reduce cost.

3.3.2.1. Scanning Electron Microscopy

The morphology of the samples can be evaluated SEM [48]. When accelerated electrons enter a solid, they are scattered both elastically, by the electrostatic interaction with atomic nuclei, and inelastically, by interaction with atomic electrons [97]. SEM images have a relatively large depth of focus, as the electrons travel very close to the optic axis, a requirement for obtaining good image resolution [97]. The general mechanism behind SEM functionality are exemplified in Figure 9.

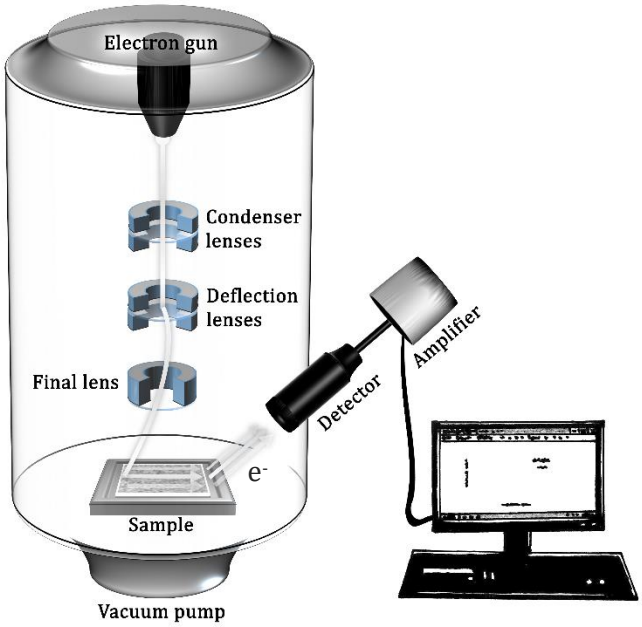

Figure 9 – Scheme of a scanning electron microscope. Based on **[97]**.

The material is scanned with the use of an electron beam, which, after passing through a series of lenses, is reflected or back-scattered, collected by a detector and displayed on a cathode ray tube screen. The image represents the surface of the scanned material [70]. Because insulating materials do not provide a path to ground for the sample current and may undergo electrostatic charging when exposed to the electron probe, coating the surface of the SEM specimen with a thin film of metal or conducting carbon is a solution. Gold and chromium are common coating materials, coated in vacuum through evaporation or sublimation techniques, resulting in film thickness of 10 to 20 nm, which is able to conduct sufficiently and prevent charging of most specimens [97].

The sample's surface and cross section can be observed, using the obtained images to determine the thickness and pore sizes of the membranes. Finally, in order to observe if the removal of nanoparticles took place after its use, SEM was also studied after four uses for the photocatalytic degradation of MB. To prepare the membranes for analysis, small squares were cut from the samples and fixed onto a suitable support. Special care had to be taken when preparing the samples for cross section analysis, so as to preserve their porous inner structure. After submerging each sample in liquid nitrogen for a few seconds, the samples were easily broken apart. All the samples were coated during 30 seconds with a thin gold layer and analyzed with a Quanta 650 from FEI Scanning Electron Microscope.

The membrane's pore size and thickness were measured based on direct observation through the obtained SEM images. As an extra means of comparison, the thickness of each membrane was measured three times in five different sites within the membrane using a Fisher Dual Scope MPDR micrometre. Finally, a sample containing P25 TiO_2 nanoparticles was also prepared for SEM observation, in order to calculate the particles size.

3.3.2.2. POROSIMETRY

Porosimetry, used to calculate the porosity of the samples, was carried out by the pycnometer method. Water is often used in this method however, because the polymeric membranes are extremely hydrophobic, an organic solvent, ethanol had to be used. After measuring the mass of a small sample (m_s), a pycnometer of approximately 25 mL was filled with Ethanol until the limit (m_1). The sample was then inserted - it is necessary to remove an excess of ethanol from the pycnometer before inserting the sample, as it otherwise would cause it to spill - and the pycnometer was filled until the limit again (m_2). Finally, after saturated with ethanol, the sample was removed and the pycnometer was weighted with the remaining ethanol (m_3) - again an excess of ethanol had to be removed and reinserted back into the pycnometer. The process can be seen in Figure 10.

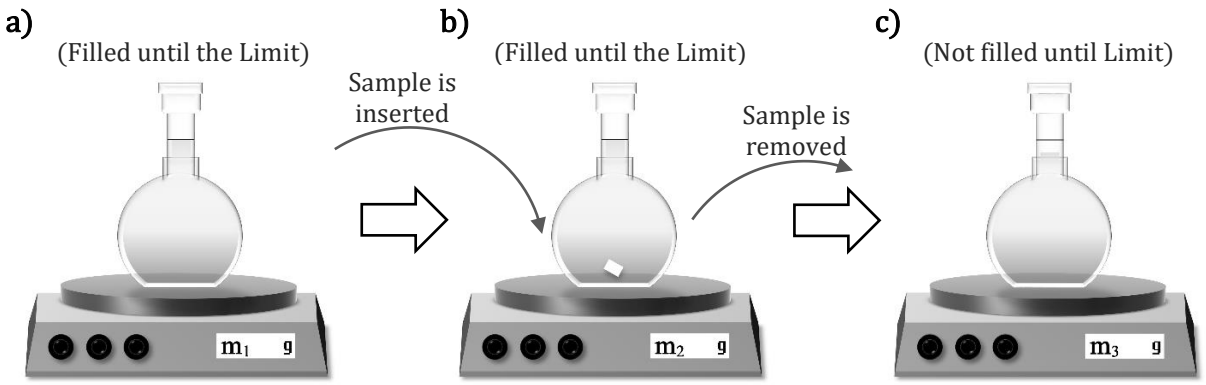

Figure 10 – Process of porosity measure through the pycnometer method; **a)** mass of the full pycnometer; **b)** mass of the full pycnometer plus the sample; **c)** mass of the unfilled pycnometer after removing the sample.

This procedure was repeated three times for each sample and the obtained values correspond to the average and the respective standard deviation. Finally, knowing how much

ethanol the membrane absorbed by the difference in masses, the percentage of porosity ϕ (%) can be calculated using the following Equation (7) [13], [73]:

$$\phi = \frac{m_2 - m_3 - m_s}{m_1 - m_3} \quad (7)$$

There is always an associated error for a loss of ethanol during the whole process and because ethanol evaporates very quickly. In this sense, it is extremely important to minimize all the other error-inducing variables, meaning the use of a clean tweezer and always making sure the pycnometer is also clean before each usage is crucial.

3.3.2.3. Contact Angle

The conventional method to determine the wettability of the membranes is through water contact angle analysis. Although a simple method, with the samples easy to be prepared and results easy to be processed, wettability is a complex phenomenon, related to both physical and chemical effects, making the contact angle dependent upon pore size, roughness, porosity and pore size distribution [78], [101]. As seen in Figure 11.a, the contact angle indicates the degree of wetting when a solid and liquid interact [102], meaning the angle of the tangent to the drop where the drop touches the surface can be related to the surface's ability to repel or absorb water.

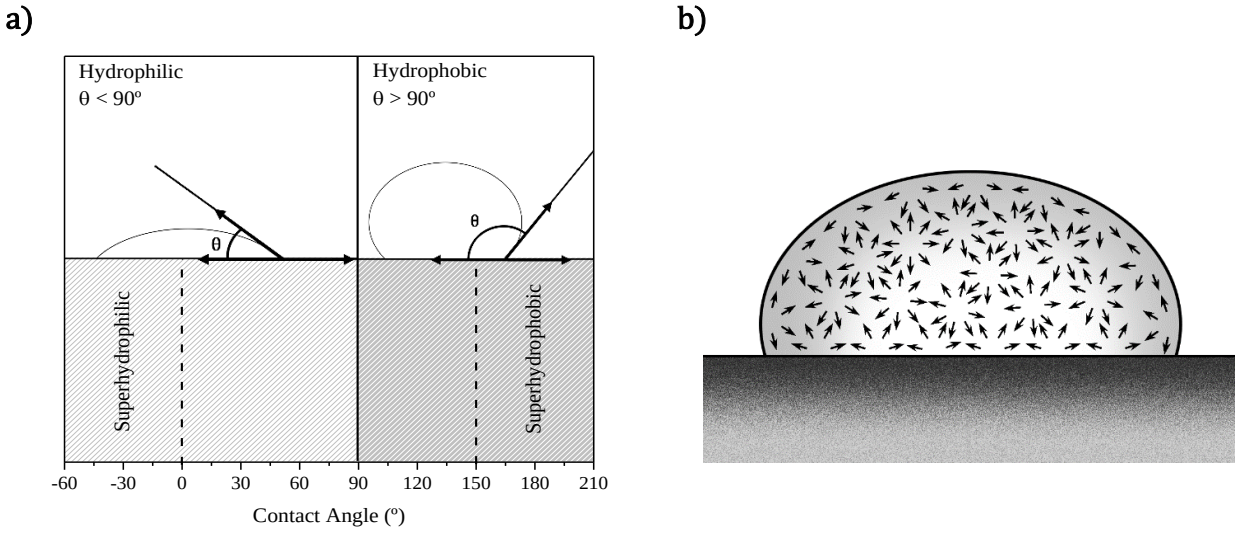

Figure 11 – a) Relation of the surface wettability with the contact angle; **b)** surface tension caused by unbalanced forces of liquid molecules at the surface. Based on and adapted from **[102]**.

More specifically, a contact angle lower than 90° indicates that wetting is favorable, therefore the fluid will spread over a large area on the surface. Furthermore, complete wetting, or super-hydrophilicity, occurs when the contact angle is 0°, where the drop turns into a flat puddle. On the other hand, contact angles greater than 90° usually mean that wetting is unfavorable therefore the fluid will minimize its contact with the surface, forming a compact liquid droplet. For super-hydrophobic surfaces, water contact angles are usually greater than 150°, showing almost no contact between the liquid drop and the surface [73], [78], [92], [102].

Because molecules exposed at the surface do not have neighboring molecules in all directions, they are only pulled by the inner neighboring molecules, creating an internal pressure (Figure 11.b), resulting in the liquid voluntarily contracting its surface area to maintain the lowest surface free energy [102]. Surface and interfacial energies determine how liquid droplets deform when they adhere to a surface. The surface free energy (γ_p) can be estimated using an adaptation of Young–Dupre equation:

$$\gamma_p = \frac{\gamma_W}{4}(1 + \cos\theta_0)^2 \quad (8)$$

where θ_0 is the contact angle at equilibrium ($\theta = \theta_0$) and γ_W is the water surface free energy of value 73 mJ m^{-2} [73], [78], [103].

To satisfy the ideal sphere assumption, the drop volume cannot be larger than 10 µL [92]. As such, drops of 3 µL of distilled water were deposited in three different sites of each membrane through a micro-syringe, at a drop rate of 5 µL s^{-1}. The contact angle was then measured using a Data Physics SCA20 microscope, at a room temperature of approximately 20º C, after 0, 5 and 10 minutes of the drop being deposited, using side view drop photographs obtained by an optical microscope equipped with a camera. The half-angle algorithm was applied by the software to calculate the contact angle values. For each drop, the contact angle value is the mean of the right and left angles measured for each drop [78], [92]. The same process was repeated where the samples were subjected to UV light for 30 minutes. The contact angle was measured at the instance of drop deposition and after times of 5 and 10 minutes, while still under irradiation of UV light. The final results were obtained as an average value and respective standard deviation of the three measured drops for every situation and membrane.

3.3.2.4. Fourier Transform Infrared Spectroscopy

The FTIR has been used to qualitatively assess the modification process of the membrane. Sample preparation and data analysis is relatively simple, however, for the analysis of the surface of a membrane, this technique presents a few limitations [101]. FTIR provides information on molecular vibrations and is commonly used to quantify the electroactive phase content of PVDF and its co-polymers [70], [74] and in biomedical, biomaterials, and tissue studies [101]. In Figure 12 the basics of a FTIR spectrophotometer are represented.

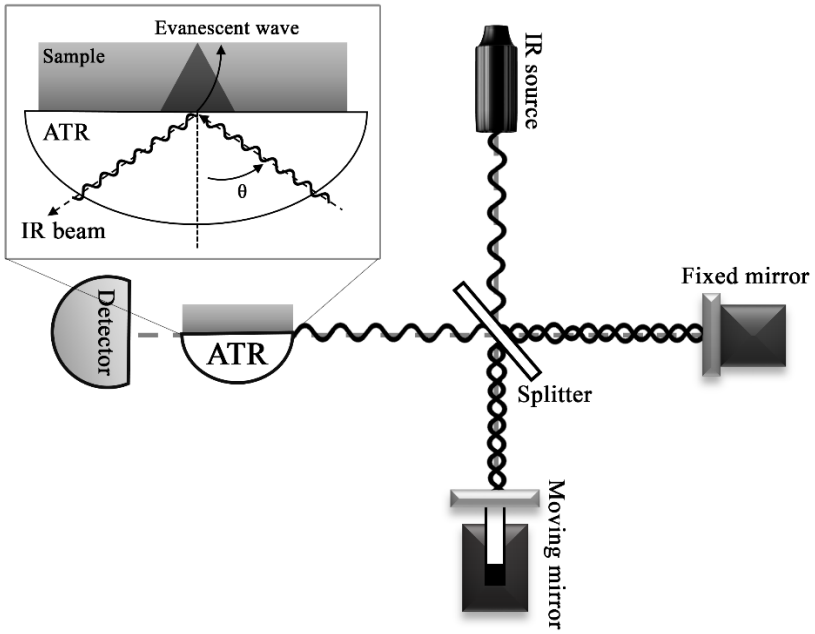

Figure 12 – Schematic of the functionality of a FTIR-ATR apparatus. Based on **[104], [105]**.

FTIR in ATR mode involves transmission of an IR beam through a crystal that has a high refractive index, resulting in near-total internal reflection at a certain angle. The internal reflectance results in an evanescent wave that typically penetrates a few microns into the sample, depending on the refractive index of the sample [104], [106]. These factors are related through equation (9).

$$\theta = \sin^{-1}\left(\frac{n_s}{n_c}\right) \tag{9}$$

where n_s is the refractive index of the sample, n_c is the refractive index of the crystal and θ is the critical angle [104].

The attenuated energy from each evanescent wave, the regions of the infrared spectrum where the sample absorbs energy, is passed back to the IR beam, which exits the crystal through

the opposite end and reaches the detector, after which an infrared spectrum in generated [74], [104], [106]. The spectra provides valuable information, allowing to distinguish between the different crystalline forms of the material [74]. In order to retrieve the intensity data from the single-beam spectrum it is necessary to perform a Fourier Transform [105]. It is then possible to identify the chemical species in a sample by measuring the obtained bands on the spectra and corresponding them to a particular bond stretching [101].

Using this technique to scan the surface of membranes that have been modified and/or fouled could yield interesting results concerning the adsorption of compounds and the modification of the membranes themselves [101]. As such, to identify the presence of micropollutant particles possibly adsorbed to the membranes after their use in photocatalysis, FTIR analysis on ATR mode was done on membranes after four uses of MB photocatalytic degradation. The spectra were obtained with a FTIR Alpha-Bruker apparatus over a range of 650–4000 cm^{-1} using 64 scans and a resolution of 4 cm^{-1}.

3.4. PHOTOCATALYTIC DEGRADATION

3.4.1. SAMPLE PREPARATION

The micropollutants ciprofloxacin (CIP), ibuprofen (IBP) and bisphenol A (BPA), were tested as model compounds for the assessment of the efficiency of the proposed materials. Methylene Blue (MB) was used as an initial model for this study allowing to easily follow the reaction by monitoring solution decolourisation, serving as a first indication that all is working correctly. Additionally, MB is widely used in photocatalytic tests, and many works using this dye are available in the literature, allowing to compare with work here presented. It is also important to note that MB is easily photodegraded under visible light, giving extra importance to the use of UV. The four tested compounds are displayed in Table 3.

Table 3 – List of micropollutants studied in this work.

Name	c (mg L^{-1})	Type	Absorption peak (nm)	Molecular structure
MB	2	Dye	665	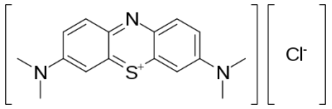
CIP	5	Antibiotic	276	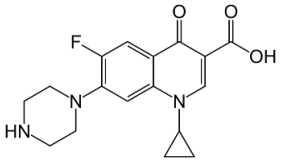
IBP	15	NSAID [1]	220 260	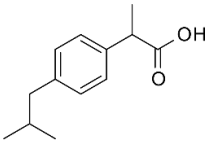
BPA	45	Phenolic	275	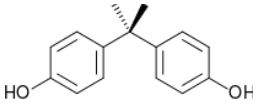

[1]- nonsteroidal anti-inflammatory drug

The solutions of model compounds were prepared at the concentration of 2 mg L^{-1} of MB, 5 mg L^{-1} of CIP, 15 mg L^{-1} of IBP and 45 mg L^{-1} of BPA. Concentrations were chosen based on the results obtained by the calibration curves [Annex C]. As CIP does not dissolve completely, it is necessary to add a few drops of sulfuric acid solution (H_2SO_4 – 1 M) under constant

magnetic stirring. In case of IBP and BPA, a base, sodium hydroxide (NaOH – 1M) was used instead of acid.

To prepare the membranes for photocatalytic degradation, 4 squares of 2 by 2 cm and 2.5 and 2.5 cm were cut for each sample. Then, they were fixed side by side onto the inner side of a borosilicate-glass beaker using double-sided adhesive tape. 50 mL of the aqueous solution containing the micropollutants solutions was used to fill the cup and immerse the membrane.

Finally, to compare the obtained immobilization results with the suspension method, samples of 50 mL were prepared for each studied pollutant, using the same concentrations of model pollutants, 2 mg L^{-1} of MB, 5 mg L^{-1} of CIP, 15 mg L^{-1} of IBP and 45 mg L^{-1} of BPA, but with 0.087 g of TiO_2, the equivalent of the 8% wt. used in the membranes, directly dispersed in the solutions.

3.4.2. Degradation of Micropollutants

Two beakers were mounted under UVA radiation, under constant stirring. In between the beakers stands a UV34 Lux Meter (PCE), to monitor the intensity of the radiated UV, which ranged from 1.8 to 1.9 mW cm^{-2}. Initially, the samples were subjected to 30 minutes under stirring in the dark (without radiation), to reach the adsorption-desorption equilibrium. Afterwards, subjecting the beakers to UV, samples were then taken at the reaction times of 0, 30, 60, 90, 120, 150, 180, 210, 240, 270 and 300 minutes. The peak wavelength of the lamp was 365 nm (6 Philips 8W mercurial fluorescent lamps – UMEX) and the beakers were placed at 15 cm from the illuminating device. The complete system can be observed in Figure 13.

Three sets of controls were used, one consisted of the solutions without the membranes exposed to the same conditions as mentioned before, another was the solution with polymer membranes containing P(VDF-TrFE) without photocatalyst, exposed to the same conditions, and another was the solution with the membranes without any exposure to light (in the dark) [ANNEX D].

To test the reusability of the nanocomposite membranes, the photocatalytic degradation experiments were carried out in quadruplicate under the same conditions. For this purpose, after each use, the membranes, still fixed onto the inner sides of the beaker, were cleaned with Millipore water under magnetic stirring for about 5 minutes and left to dry completely before

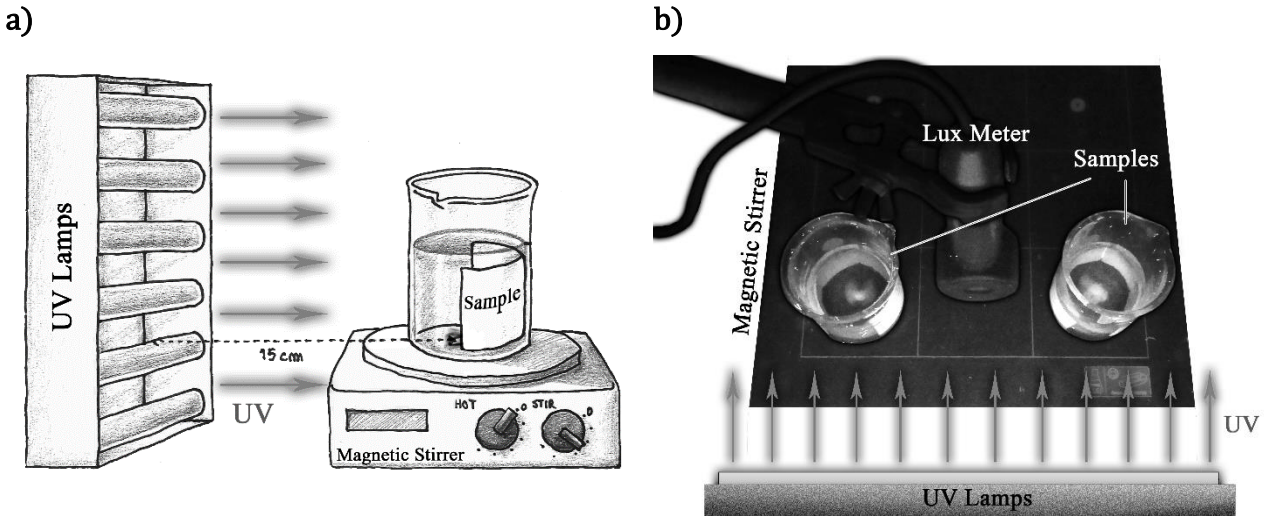

Figure 13 – a) Lateral perspective; **b)** top perspective; Scheme of the photocatalytic reactor with 6 UV lamps standing 15 cm apart from the centre of the samples. During the whole process, the samples were in constant magnetic agitation.

the next use. A total of four photocatalytic degradation assays were conducted for each membrane, except for the controls, in the aforementioned conditions.

Finally, a single degradation was made for each of the studied pollutants, using the initial pollutant's concentration with the TiO_2 nanoparticles directly dispersed in the solutions. After 30 minutes in the dark, the solutions were subjected to UV radiation with samples taken at 0, 5, 10, 20, 30, 45, 60, 75 and 90 minutes. These samples were posteriorly centrifuged for 40 minutes at 18000 rpm, to remove the catalyst, and the pollutants degradation was monitored by UV-Vis spectroscopy. This is a necessary step for samples containing TiO_2 nanoparticles in suspension, because if there are particles present, scattering will occur, thus influencing the results.

3.4.3. SPECTROPHOTOMETER AND MICROPLATE READING

The photocatalytic degradation of each micropollutant was analysed by monitoring the intensity variation of the main absorption peak of each compound, by using spectrophotometric techniques, which is simple, rapid, moderately specific and applicable to small volumes [107].

UV-Visible spectrophotometry principle revolve around the fundamental Beer-Lambert law, which states that, when a beam of light passes through a transparent cell containing a solution of an absorbing substance, the intensity of light can decrease. A spectrophotometer indirectly measures the amount of UV or visible light absorbed by a substance in solution as a

wavelength function, by way of detecting the transmitted radiation (that was not absorbed by the solution), which is proportional to the absorbed signal. Qualitatively, organic compounds can be identified using this method, if any recorded data is available, in order to ascertain the quantity of molecular species absorbing the radiation [107]. The main components of a spectrophotometer are displayed in Figure 14.

The Absorbance can also be given in relation to the Transmittance by the relation:

$$A = \log_{10}\left(\frac{1}{T}\right) = \log_{10}\left(\frac{I_0}{I}\right) \tag{10}$$

with T being the transmittance, which is the portion of the incident light at a certain wavelength that passes through the sample, I_0 represents the intensity of the incident light and I represents the intensity of the transmitted light.

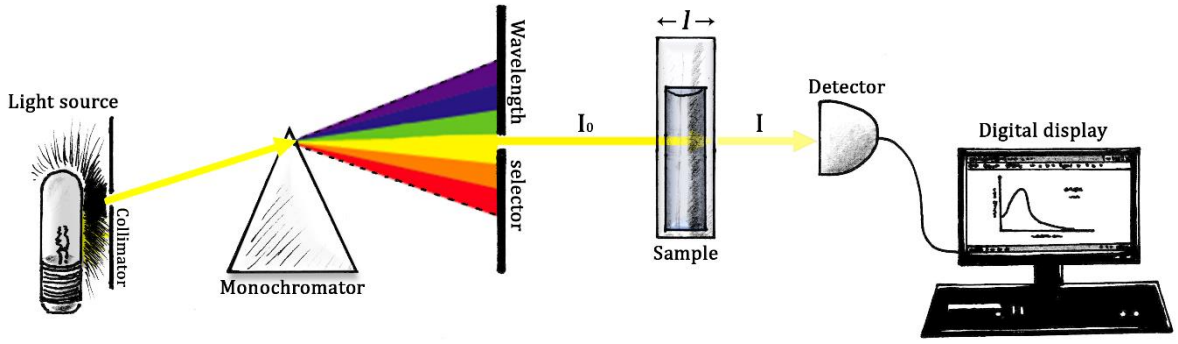

Figure 14 – Basic schematic of a spectrophotometer.

The concentration of the compound at different reaction times can be estimated by the Beer-Lambert law:

$$A = \varepsilon \cdot l \cdot c \tag{11}$$

where, A is the absorbance of the sample at the maximum wavelength (λ_{max}), ε is the molar coefficient, l the length of the cuvette (1 cm) and c the concentration of the sample [105], [107], [108].

Accordingly, given Equation (10) and (11), the following relation is obtained:

$$\log_{10}\left(\frac{I_0}{I}\right) = \varepsilon \cdot l \cdot c \tag{12}$$

$$\Rightarrow I = I_0 10^{-\varepsilon \cdot l \cdot c} \tag{13}$$

Equation (12) relates the quantity of transmitted radiation with the concentration of the sample. As concentration increases, so does the absorbance, thus decreasing the transmitted

light. Based on this, the UV-vis spectra were recorded and the respective concentrations of Micropollutants were calculated at λ_{max} using the molar extinction coefficients, which were determined at [Annex C]. The monitored peaks and their respective absorbance values were used to estimate the amount of degraded Micropollutants during the photocatalytic process, as well as the needed initial concentrations needed for the wanted Absorbance, as the measuring equipment shows certain limitations.

The reaction of the degradation of pollutants in an aqueous solution fits a pseudo-first-order reaction, the Langmuir-Hinshelwood model, which can be expressed by the expression:

$$\ln\left(\frac{C}{C_0}\right) = -kt \tag{14}$$

where C_0 and C represent the concentration of the dye initially and at the time t, obtained through the maximum value of absorbance, and k is the pseudo first-order rate constant of the reaction, or reaction rate (min^{-1}) [13], [109]. Resolving Equation (14) in relation to C, the following relation is obtained:

$$\Rightarrow C = C_0 e^{-kt} \tag{15}$$

By fitting an exponential curve to the data obtained through the peaks of Absorbance over time, k is easily obtained by the slope of the curve, which will be the reaction rate of the degradation.

The photocatalytic degradation of all pollutants was determined by analysing the absorbance spectrum of the aqueous solutions removed over time from the degradation tests. This was done with the use of a Varian CARY-100 UV-VIS spectrophotometer, for the case of the immobilization tests, and a Biotek Cytation3 Microplate reader in spectrum mode using 96-well plates, with 0.2 mL for each sample, in triplicate, for the case of the tests in suspension.

4. RESULTS AND DISCUSSION

In this Chapter, the results respecting membranes characterization and application are presented and discussed, also allowing for a brief comparison with previous works in the literature.

4.1. CHARACTERIZATION OF THE NANOPARTICLES AND MEMBRANES

In this sub-section, the materials characterization results are analysed and discussed. Firstly, the results of P25 TiO_2 nanoparticles will be analysed, followed by the processed nanocomposite membranes.

4.1.1. NANOPARTICLES

4.1.1.1. PARTICLE SIZE AND PHASE CONTENT

The particle size distribution of P25 TiO_2, calculated through SEM imaging (measured 200 times in a total of two SEM images) can be seen in Figure 15.a. In order to assess the phase composition of the TiO_2 nanoparticles, diffraction patterns obtained through XRD of both anatase and rutile TiO_2 powders were compared with reference to JCPDS database. The obtained peaks and corresponding phases can be observed in the Figure 15.b.

Because photocatalytic reactions occur on the surface of the nanocatalyst, when the surface area increases, the number of active sites increases proportionally [13]. In this sense, a high specific surface area is one of the most important properties in photocatalytic activity, meaning a smaller diameter can favour photocatalysis. As such, the size of the P25 TiO_2 particles was measured (Figure 15.a). The SEM images displaying the TiO_2 nanoparticles and the measured standard diameter of 33.8 ± 10.8 nm show that the size is in accordance with the manufacturer ($\simeq$ 21 nm) and literature [45], [73]. For instance, Teixeira *et. al.* [45] obtained a specific surface area of 56 $m^2\ g^{-1}$ for P25 TiO_2 nanoparticles and a particle size of 25 ± 3.32 and Martins *et. al.* [73] obtained a size of $\simeq$ 30 nm, both by SEM analysis.

In the XRD patterns, Figure 15.b exhibit strong diffraction peaks at 25°, 38°, 48° and 54° indicating TiO_2 in the anatase phase (101), (004), (105) and (200), respectively, and at 27°, 55°

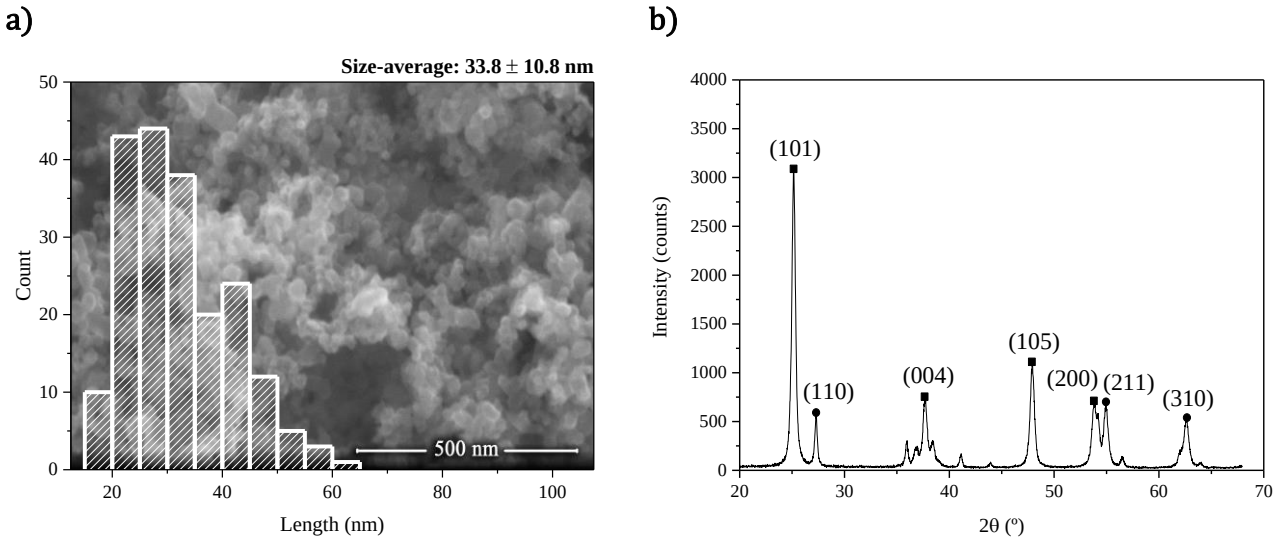

Figure 15 – a) SEM image of TiO_2 P25 nanoparticles and respective particle size histogram; **b)** XRD patterns of TiO_2 nanoparticles in its (■) anatase phase and (●) rutile phase.

and 63°, indicating TiO_2 in the rutile phase (110), (211) and (310), respectively. All peaks are in good agreement with the standard spectrum (JCPDS card 88-1175 and 84-1286) [Annex A].

Through the presence of almost all the same phases observed in this study in all of the considered published articles by other authors, it is possible to conclude that these results are well related with previous works and with the data sheet provided by manufacturer [13], [45], [73], [83]. Additionally, although anatase, brookite, and rutile are the three main phases of TiO_2, presenting different photocatalytic activities, anatase is the most photocatalytic active [45].

4.1.1.2. Hydrodynamic size and Electric charge stability

The results obtained by of the Dynamic Light Scattering (DLS) and Zeta (ζ) potential (ZP) studies are shown in Figure 16. These results give the particle size and the surface charge of the particles through the interaction between the charges in relation to the pH of the solution.

Observing the results (Figure 16.a), the standard particle hydrodynamic diameter and deviation is 430 ± 28 nm, which is significantly above the estimated value by SEM and the value provided by the manufacturer. In SEM analysis $\simeq$ 30 nm was obtained and the data sheet provided by Evonik ® indicates $\simeq$ 21 nm. This difference can be addressed to nanoparticles agglomeration in the aqueous medium, as they show a smaller diffusion rate and higher light scattering than isolated particles [13], [73]. As a comparison, Martins *et. al.* [13] obtained a size

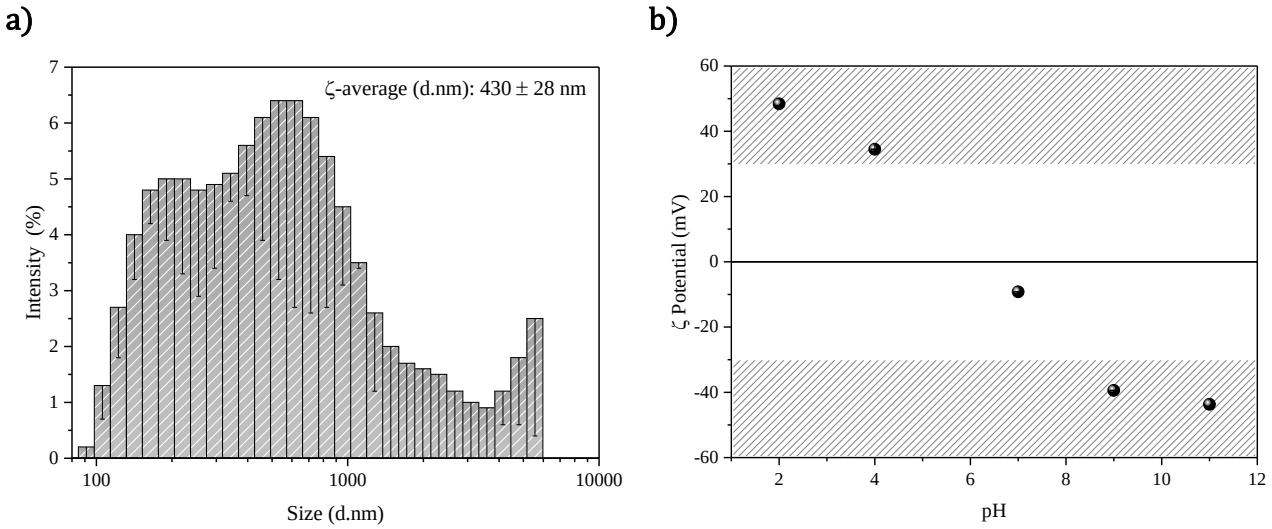

Figure 16 – a) Histogram and standard deviation of particle size of TiO_2 nanoparticles done by DLS; **b) ζ** potential curves for the studied TiO_2 nanoparticles in relation to the level of pH.

of 28 ± 5 nm by DLS. Nonetheless, both data present a similar trend. This can be countered if the DLS analysis is done when the pH of the solution is in the stable zeta potential zone, as it lessens the probability of particle agglomeration.

On the other hand, it is known that the equilibrium is normally found at ZP values superior than 30 mV and inferior than -30 mV [13], [73], this means that, by studying our obtained results in Figure 16.b, the particles show stability at pH values at least ≤ 4 and ≥ 9. In this range, the peripheral charge in the surface of the nanoparticles is higher, aggravating the repulsion between nanoparticles. This creates greater stability and avoids aggregation and precipitation of the nanoparticles [13], [73]. The isoelectric point can also be observed at around $pH = 6.5$. These results are consistent with the literature which indicates that the TiO_2 net charge is 0 at $pH = 6.8$ and that TiO_2 is positively charged at $pH < 6.8$ and negatively charged at $pH > 6.8$ [13], [41], [73]. ZP measurements are important for photocatalysis, as the adsorption of molecules is dependent upon pH. This means that, if the TiO_2 nanoparticles and the micropollutants exhibit opposite charges from one another, they will attract each other, promoting the adsorption and enhancing the photocatalytic activity [13], [73].

4.1.2. POLYMERIC MEMBRANES

4.1.2.1. MORPHOLOGY, PORE SIZE, POROSITY AND MEMBRANE THICKNESS

As a primary analysis, the surface samples before utilization can be observed through SEM imaging and compared in the following images in Figure 17.

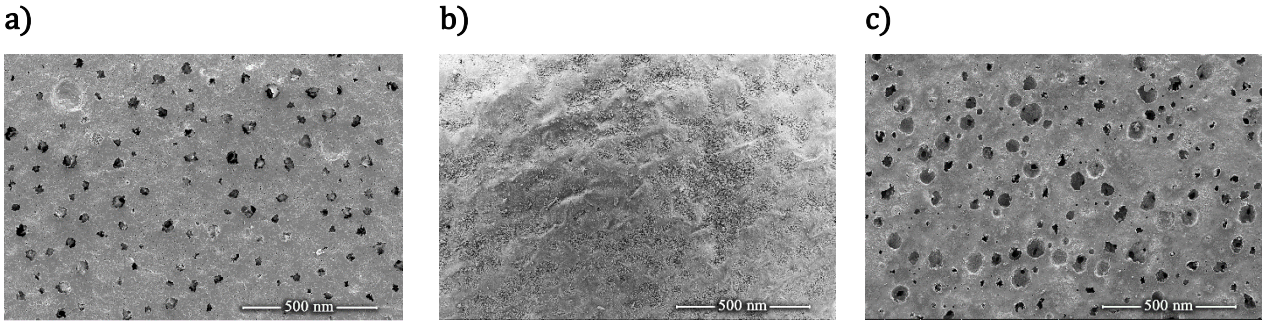

Figure 17 – SEM surface images of **a)** P(VDF-TrFE); **b)** P(VDF-TrFE)/TiO_2; **c)** P(VDF-TrFE)/TiO_2/NaY membranes.

As can be observed in Figure 17, all the membranes possess a porous structure, though, because of contrast and low definition reasons, they are not so easily spotted in the membrane with P(VDF-TrFE) and TiO_2 nanoparticles (Figure 17.b). The porous structure of the membranes was achieved thanks to the evaporation of the solvent Dimethylformamide (DMF) at room temperature from a homogeneous solution [45]. In Figure 18 are the SEM images for simple P(VDF-TrFE) membranes with two distinct scales.

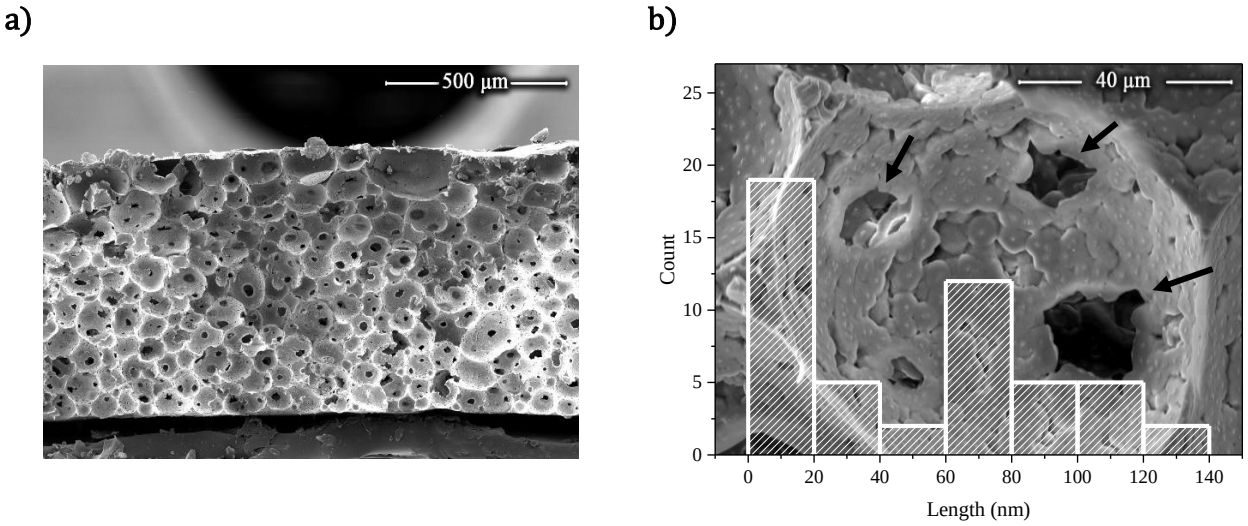

Figure 18 – Cross section images of P(VDF-TRFE) membranes before use **a)** lateral view; **b)** close up of the pores and respective pore size histogram estimated from 50 pores. Black arrows indicate smaller pores within pores.

It is possible to spot the presence of few nanoparticles attached to the surface of the membranes in Figure 17.b and Figure 17.c. However, through cross section, it was able to obtain a better understanding of the morphology of the membranes, by looking directly into the interior of the membrane and the interconnected pores and calculating the pore size distribution.

In Figure 18.a, the presence of pores inside pores can be observed. The interconnectivity between these pores favor percolation and eases the reach of the pollutant nanoparticles well inside the membrane. The porosity also is maintained throughout the membrane and not just at its surface. Using the cross section SEM images, the diameters of a total of 50 pores were measured in each membrane using the software ImageJ. The histograms of the individual membrane pore sizes were then constructed (Figure 18.b). The pores presented well distributed sizes between 10 and 130 μm.

In order to compare the morphologies of the membranes before and after their use in photocatalysis, SEM was performed for both cases. This analysis was not performed for the simple P(VDF-TrFE) membranes as these do not contain the necessary photocatalyst used in the process and are only used as a control. In Figure 19 the SEM images for P(VDF-TrFE) with TiO_2 membranes with two distinct scales and its respective pore size histogram, as well as SEM images after four MB photocatalytic degradations, are presented.

In Figure 19, the images of TiO_2 nanoparticles stationed inside the pores in both before and after use, can be seen, meaning that nanoparticle loss did not take place after four photocatalytic utilizations and membrane cleaning. Through Figure 19.d a wider distribution of the nanoparticles throughout the pores can be noticed, indicating they were re-dispersed

a)

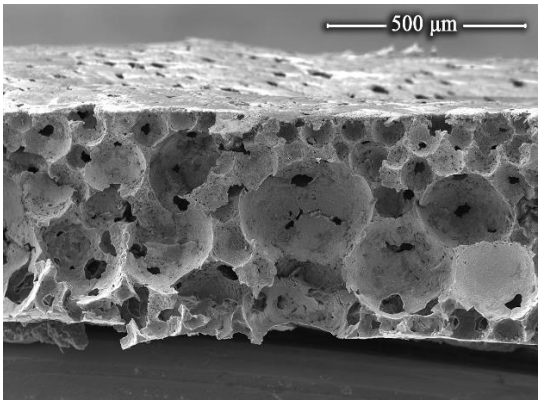

b)

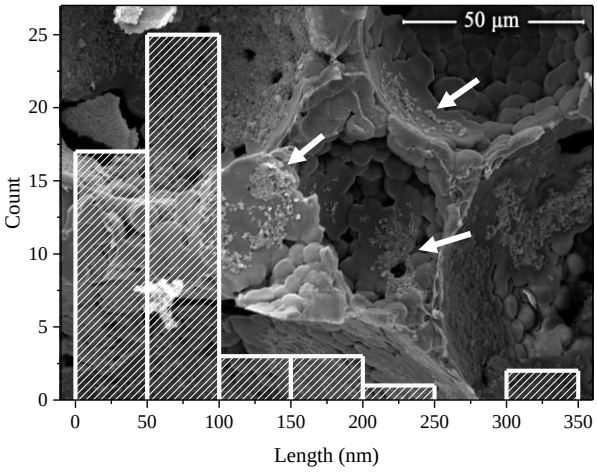

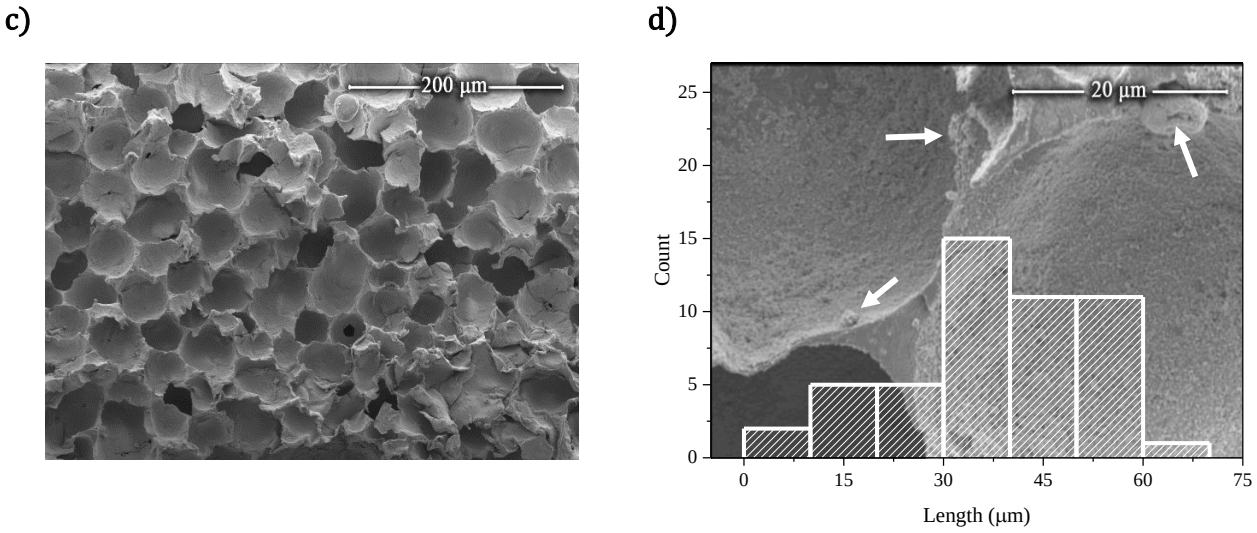

Figure 19 – Cross section images of P(VDF-TRFE) with 8% wt. TiO_2 membranes **a)** before use; **b)** before use, close up of the pores with the nanoparticles and respective pore size histogram estimated from 50 pores; **c)** after four MB uses; **d)** after four MB uses, close up of the pores with the nanoparticles and respective pore size histogram estimated from 50 pores. White arrows indicate nanoparticle aggregations.

after four utilizations. The membranes before use have a pore size distribution between 25 and 325 µm, larger than the purely polymeric membrane. After use, the size of the pores ranged from 5 to 65 µm, meaning a decrease in size, although it is inside the measurements error

In Figure 20 are the SEM images for P(VDF-TrFE) with TiO_2 and NaY membranes with two distinct scales and its respective pore size histogram, as well as SEM images after four MB photocatalytic degradations.

By observation of the SEM images in Figure 20, all membranes show similar spherical pores, independent of the presence of nanoparticles. A good dispersion of nanoparticles within the polymer matrix, was also achieved, present even after four uses in photocatalytic degradation. Similarly observed in the P(VDF-TrFE)/TiO_2 membranes, and by observing Figure 20.d, the particles seem to have suffered a re-distribution after four used in MB, although it is not possible to distinguish the nanoparticles aggregates from the zeolites. The P(VDF-TrFE) with TiO_2 and NaY membranes show a pore size distribution between 5 and 85 µm, the smallest values out of all membranes before use. Pores inside pores and high interconnectivity is once more visible. After use, the pores apparently became bigger, with values ranging from 10 and 190 µm. This can be due to the fact that water promotes pore dilation, as the smaller pores get subsequently bigger.

The mean and standard deviation of the pore size, obtained through the histograms of the SEM images, for all three types of membranes before use, as well as the porosity results

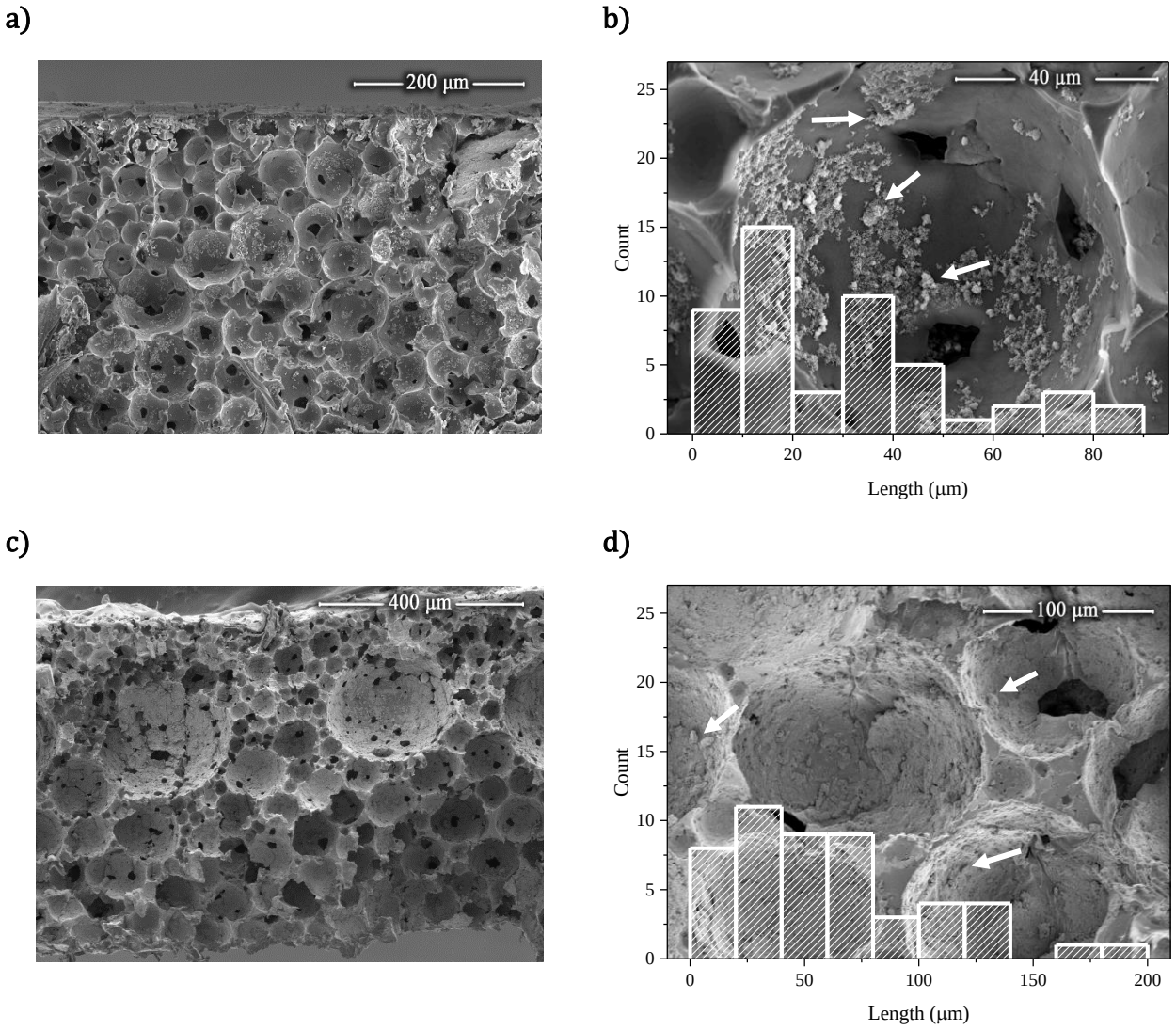

Figure 20 – Cross section images of P(VDF-TrFE) with 8% wt. Tio_2 and 3% wt. NaY membranes **a)** before use; **b)** before use, close up of the pores with the nanoparticles and respective pore size histogram estimated from 50 pores; **c)** after four MB uses; **d)** after four MB uses, close up of the pores with the nanoparticles and respective pore size histogram estimated from 50 pores. White arrows indicate nanoparticle/zeolite aggregations.

obtained by the pycnometer method can be compared by the results set in Figure 21. Lastly, in order to compare the membrane thickness through different methods, the mean and respective standard deviation results of the membrane's thickness measured with SEM and the micrometre can also be observed in Figure 21.b.

Observing Figure 21.a, all of the samples present a porosity level above 70%, with pore sizes ranging between 30 and 80 µm. This is in agreement with the pore size range of 50 – 80 µm obtained by Martins *et. al.* [13]. The membrane featuring zeolites shows the highest porosity, at 89 $\pm$ 5 %, and at the smallest pore size, at 30 $\pm$ 20 µm. This is in agreement with the observation of the SEM images, were a higher number of small pores inside pores can be seen, meaning a higher pore concentration but smaller overall pore size. Because zeolites, in

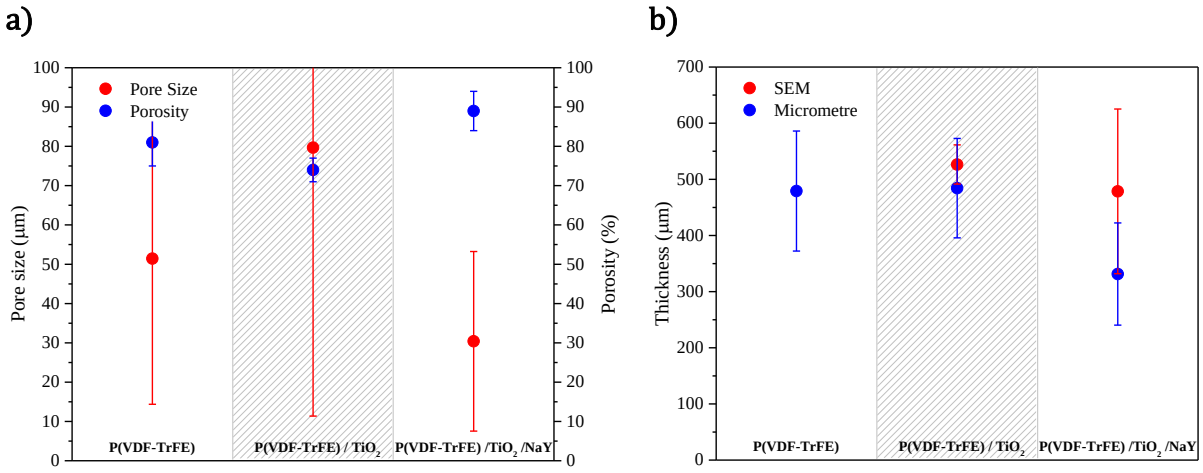

Figure 21 – Average value and standard deviation for **a)** pore size and porosity; **b)** membrane thickness observed in the composite membranes with the use of SEM and ImageJ and a micrometre.

themselves, are porous, which is presented in the form of a cavity the size of a few Å, the porosity results refer to the porosity of the membrane and the zeolites. The membrane with TiO_2 nanoparticles but without zeolites show the highest values of pore size, of 80 $\pm$ 68 µm, as through observation of the SEM images, few pores inside pores are seen, making the big main pores predominant. This membrane also shows the smallest values in porosity, 74 $\pm$ 3 %. The membrane with just P(VDF-TrFE) features values in between, with pore size values of 51 $\pm$ 37 µm and porosity levels at 81 $\pm$ 6 %, meaning the TiO_2 nanoparticles and the NaY zeolites influence the microstructure of the polymer. All the major differences in pore size and thickness are within experimental errors. The porosity results do not only represent the membrane porosity, as they are dependent upon the porosity of the zeolites. As such, the decrease of the average pore size and the increase of the overall porosity can indicate a strong influence of the zeolites on the phase diagram and the crystallization process. Martins *et. al.* [73] indicate that zeolites act as nucleation elements for the crystallization of the polymer, hindering barriers for the phase separation process and leading to a higher number of smaller pores. For photocatalytic application, large pore interconnectivity enhances light penetration, while increasing mass transfer of pollutants and reactants [13], [14], [73].

The obtained results for pore sizes and porosity are in accordance with the authors in [45] who observed average pore sizes of 21.3 $\pm$ 8.1 µm, for 15 wt.% of the TiO_2 nanocomposites, Martins *et. al.* [73] obtained pores ranging from 51 to 62 µm and 73 to 79% of porosity for pristine polymer and samples containing TiO_2 nanoparticles and 24 µm with 89% when adding of 3% of NaY.

Porosity is also a crucial factor because degradation efficiency is deeply related to the nanocomposite microstructure, as a suitable polymeric structure enables good mass transfer, promoting proper light harvesting and interaction between the micropollutants and the porous inside wall loaded with nanoparticles, making the membrane suitable for photocatalysis [13]. However, an exceedingly small pore may prove disadvantageous if it forbids the passage of the micropollutants, reducing the active site of the membrane.

The membrane with NaY was the thinnest of the three in both measurement methods, with 480 ± 150 and 330 ± 90 μm by SEM and the micrometre, respectively (Figure 21.b). The membrane with both PVDF-TrFE and TiO_2 does not show much difference between the two methods, with 530 ± 40 μm, by SEM, and 480 ± 90 μm, by the micrometre. The membrane with just P(VDF-TrFE) presents the most observed differences between the 660 ± 10 μm observed through SEM and the 480 ± 110 μm observed through the micrometre. This last discrepancy in values can be due to the lack of measured data of P(VDF-TrFE) membrane through SEM, as it was only possible to measure one membrane in two different sites, as opposed to two membranes in four total different sites, as was the case of the P(VDF-TrFE)/TiO_2 and P(VDF-TrFE)/TiO_2/NaY membranes. Other authors obtained thickness values of ~ 550 μm [13], which are in accordance with the results obtained in this study. The porosity, pore size and membrane thickness characterization results are summarized in Table 4.

Table 4 – Summary of porosity, obtained through the pycnometer method, and pore size results, obtained through SEM imaging, and membrane thickness, obtained with SEM imaging and a micrometre, for the three tested membranes before use.

Type	Pore Size (μm)	Porosity (%)	Thickness (μm)	
	d	**ε**	**h_{SEM}**	**h_M**
P(VDF-TrFE)	50 ± 40	81 ± 6	660 ± 10	480 ± 110
P(VDF-TrFE)/TiO_2	80 ± 70	74 ± 3	530 ± 40	480 ± 90
After four MB uses	40 ± 10	-	-	-
P(VDF-TrFE)/TiO_2/NaY	30 ± 20	89 ± 5	480 ± 150	330 ± 90
After four MB uses	60 ± 40	-	-	-

As previously stated, because the efficiency of the process is highly dependent upon a good interaction between the micropollutant and the TiO_2 surface, the above facts prove the

importance of a suitable porous structure, which make these membranes appropriate for photocatalytic activity [13], [73].

4.1.2.2. WETTABILITY

Contact angle tests were performed in order to estimate the wettability of the nanocomposite membranes and its variation upon UV exposure. The super-hydrophilic characteristic of TiO_2 when subjected to UV light is well known [110], [111]. As such, it is mandatory to test if the presence of TiO_2 influences the wettability of the polymeric membranes.

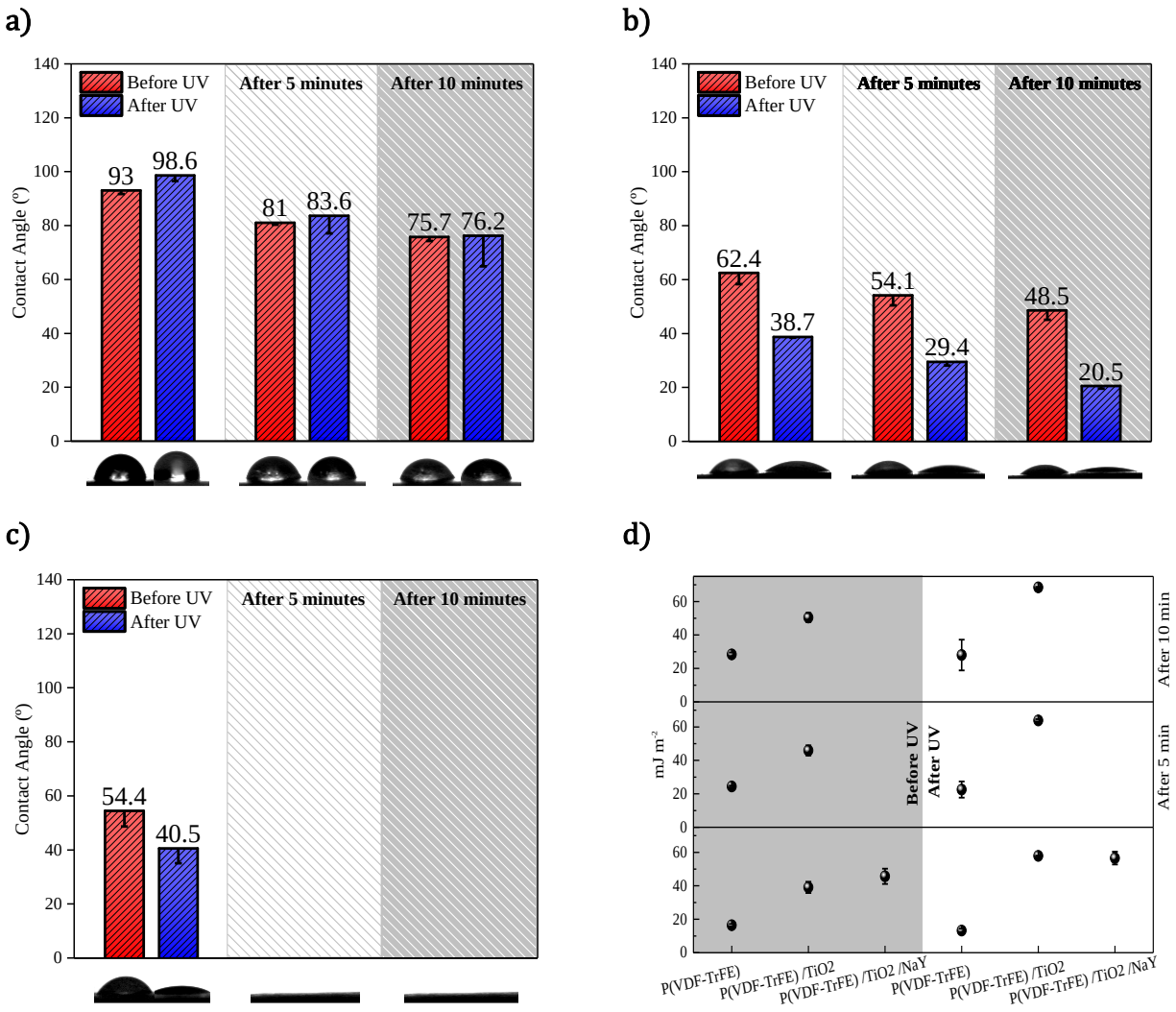

Figure 22 – Contact angle before and after exposure to 30 minutes of UV radiation, for 0, 5 and 10 minutes after the drop was placed, for a) P(VDF-TrFE); b) P(VDF-TrFE)/TiO_2; c) P(VDF-TrFE)/TiO_2/NaY; d) estimated surface free energy γ_p.

As explained in chapter 3, the wettability of the membranes was studied by measuring the contact angle of water drops in the surface of the membranes. The results can be observed in the graphics in Figure 22, which represent the standard contact angle value after a total of 10 minutes of deposition time for the three types of membranes produced, while also comparing them before and after being exposed to 30 minutes of UV radiation. Figure 22.d depicts the surface free energy of the membranes, calculated using the obtained contact angles.

As can be seen in Figure 22.b, the membrane with TiO_2 nanoparticles displayed a more hydrophilic behaviour when compared with the membrane without TiO_2, with angles ranging from 48.5° to 62.4°. The results in time are similar to the obtained to the pristine membrane (Figure 22.a) but it is clear that the presence of TiO_2 favours the absorption of water by the membrane with the effect being increased after being subjected to UV, with angle values from 20.5° to 38.7°.

Contact angles can be changed by chemically modifying surfaces or adding certain solute molecules into the medium of the surfaces [103]. The latter is verified by the results of P(VDF-TrFE)/TiO_2/NaY membrane (Figure 22.c), which present the most hydrophilic results, contact angle of 54.4°, before UV exposure. The drops here are completely spread after 1 minute of deposition time, with the angle being smaller after subjected to UV radiation, 40.5°, when comparing to before UV exposure.

When the surface of a photocatalyst is exposed to UV, the contact angle of the water drop deposited on its surface is gradually reduced. After enough exposure to light, the surface becomes super-hydrophilic, meaning it does not repel water at all, so the water cannot exist in the shape of a drop, but instead flatly spreads on the surface of the substrate, as seen in Figure 22.b, or even reach the point of absorbing the drop completely, as seen in Figure 22.c. Because P(VDF-TrFE) is known to be extremely hydrophobic (as was also proved by Figure 22.a), the difference in contact angle observed between samples indicates that the presence of TiO_2 nanoparticles, with their UV-induced super-hydrophilic behaviour, alters the hydrophobic nature of the P(VDF-TrFE) membranes. This is in accordance with what was observed through the earlier surface SEM images, *i.e.* few TiO_2 nanoparticle exist at the surface of the membrane. If the contrary were to happen, and a great number of nanoparticles were detected, this would result in smaller contact angles than those obtained after UV exposure.

The inverse can be seen in the calculated surface free energy results, visible in Figure 22.d, where the value of γ_p decreases when θ increases, meaning that the membrane with

zeolytes and the membranes with TiO_2 nanoparticles after UV exposure present the highest values of γ_p.

In Table 5 the main results are summarised.

Table 5 – Summary of the values of contact angle and surface free energy for the studied membranes.

Type	t (min)	θ (°)		γ_p (mJ m^{-2})	
		Before UV	After UV	Before UV	After UV
P(VDF-TrFE)	0	93.0 ± 1.3	98.6 ± 2.1	16.4 ± 0.8	13.2 ± 1.1
	5	81.0 ± 0.7	83.6 ± 6.5	24.4 ± 0.5	22.5 ± 4.8
	10	75.7 ± 1.5	76.2 ± 11.3	28.4 ± 1.1	28.0 ± 9.2
P(VDF-TrFE)/TiO_2	0	62.4 ± 4.1	38.7 ± 0.3	39.1 ± 3.4	57.9 ± 0.2
	5	54.1 ± 3.7	29.4 ± 1.3	45.9 ± 3.0	64.0 ± 0.7
	10	48.5 ± 3.4	20.5 ± 0.9	50.5 ± 2.8	68.5 ± 0.4
P(VDF-TrFE)/TiO_2/NaY	0	54.4 ± 5.7	40.5 ± 5.5	45.7 ± 4.6	56.6 ± 3.8
		Drop is completely spread			

These results are in agreement with those obtained in the literature, by Martins *et. al.* [73] obtaining contact angles of 76° and 97° and surface energy of 27.9 mJ m^{-2} and 13.87 mJ m^{-2} for pristine polymer and 8% of TiO_2 nanoparticles, respectively. Previous works also studied and reported on the hydrophobic nature of polymer nanocomposites containing TiO_2 nanoparticles. Similarly observed through our own results, these particles only display hydrophilic behaviour when irradiated with UV [73]. The inclusion of zeolites also yields hydrophilic properties to the membrane as the water droplet completely spreads onto its surface and is rapidly absorbed. These properties are exclusively attributed not only to the micro-porosity and capillary effect of the zeolites but also to the increased irregularity caused by zeolites on the surface of the membrane. By increasing the wettability it is possible to promote the contact between the pollutant and the surface of the TiO_2 nanoparticles, which is key for improving the photocatalytic performance.

4.1.2.3. PHASE CONTENT AND CHEMICAL PROPERTIES

In order to determine the polymer phase content and the chemical interaction between the photocatalytic nanoparticles and the polymer matrix, Infrared Spectroscopy (FTIR-ATR) tests were conducted. The results are shown in Figure 23.

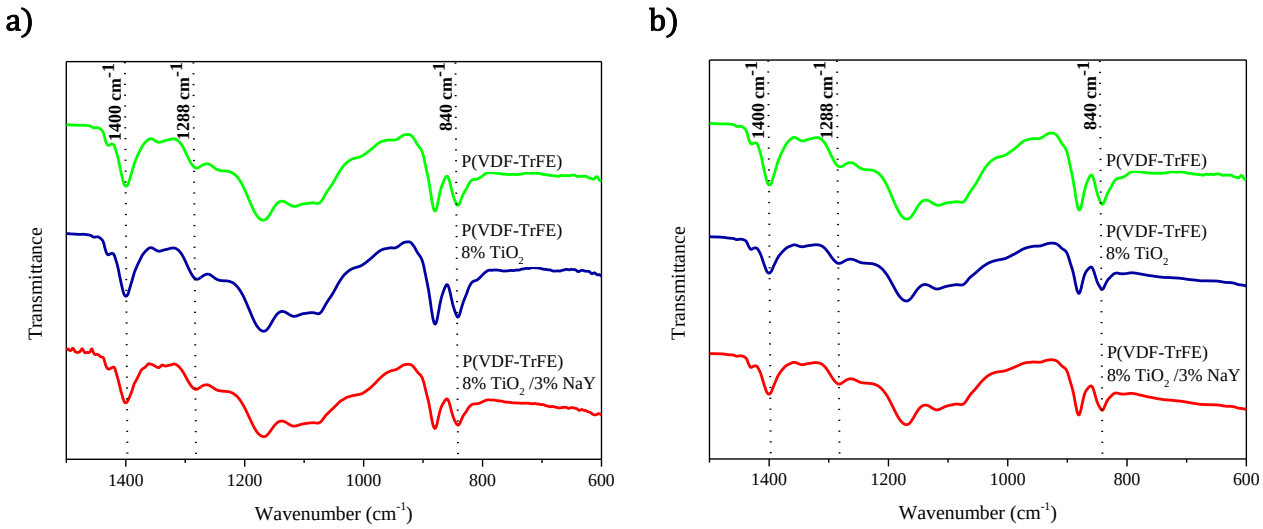

Figure 23 – FTIR spectra of P(VDF-TrFE) nanocomposites with TiO_2 and NaY nanoparticles **a)** before use; **b)** after four uses in MB photocatalytic degradation.

Through observation of Figure 23.a, FTIR spectra show that P(VDF–TrFE)/TiO_2 and P(VDF–TrFE)/TiO_2/NaY composites show unchanged polymer structure when comparing to the pristine polymeric membrane. Comparing with the standard PVDF peaks in [Annex B], it can be noticed that the characteristic bands of polymer β-phase appear at 840, between 1279 and 1290 and at 1400 cm^{-1}, which are present in all samples. No FTIR bands at 766, 795, 855 and 976 cm^{-1} were observed, attributed to the nonpolar α-phase, or 776, 812, 833 and 1234 cm^{-1}, characteristic of a γ-phase. This implies that P(VDF-TrFE) crystallization induced the formation of β–phase, independent of the nanoparticles presence and content, and no chemical bonds were detected between the polymer and the incorporated nanoparticles [13], [45], [73]. Even though a band around 900–1100 cm^{-1} should be observed when adding zeolites, this is not the case. As comparing with the results obtained by the Martins *et. al.* [73], it can be concluded that the concentration of zeolites used in this work is not enough to observe the referred peak. Furthermore, Martins *et. al.* [73] concluded that membranes with 8% of NaY lose some mechanical properties, consequently, ideally a lower concentration should be used, which is the case of this work.

FTIR-ATR was measured after the membranes were used, in order to detect traces of micropollutants. Even after four uses, no changes in the bands seem to occur. Moreover, the chemical structure of the membranes does not seem significantly affected after four uses for long periods of time under UV, retracing the fact that PVDF copolymers are extremely resistant to radiation. These results mean that any pollutant was adsorbed at the membrane and that the decrease of their concentration was due to degradation.

4.2. PHOTOCATALYTIC DEGRADATION OF MICROPOLLUTANTS

The degradation results of the studied micropollutants, methylene Blue (MB), ciprofloxacin (CIP), ibuprofen (IBP) and Bisphenol A (BPA), by photocatalysis were analysed by spectrophotometry. Absorbance spectra and kinetic curves were built for easy visualization of the results. As a means of comparison between the two photocatalytic systems, photocatalysts were tested in suspension and immobilization. As such, a few experiments were performed in solution using the same photocatalyst (P25 TiO_2) and pollutants concentrations under the same conditions.

4.2.1. METHYLENE BLUE

Photocatalytic activity was first tested by degrading 2 mg L^{-1} of MB in an aqueous solution, under UV radiation. MB shows a maximum absorption peak at around 665 nm [13], [73] and upon exposition to UVA radiation, the absorption peak is gradually diminished, illustrating its degradation.

Figure 24 illustrates the difference in area of the membrane versus exposure to the light source. The objective was to observe whether or not the nanoparticles had been uniformly distributed throughout the membrane, even when using a higher area. Opposing light can reach the whole membranes with smaller 4x4 cm area.

By observation of the graphics in Figure 24, it is obvious that surface area is the main factor here, as the membranes with 5x5 cm area took less time to degrade the sample than the membranes with 4x4 cm area, even if it seemed they were abstracting the light from reaching the whole membrane. It is also conclusive that the membranes with 3 wt. % of NaY degrade MB even faster than the membranes without it. A small peak shift in the MB spectrum to values below the monitored 665 nm peak can also be observed. This shift may be associated with the N-demethylation of MB by the TiO_2 nanoparticles or the formation of N-demethylated intermediates [13]. High Performance Liquid Chromatography (HPLC) combined with Mass Spectroscopy (MS) should be performed in order to prove this idea [61]. Furthermore, it was observed that the MB solution has become completely colourless after 300 minutes of irradiation.

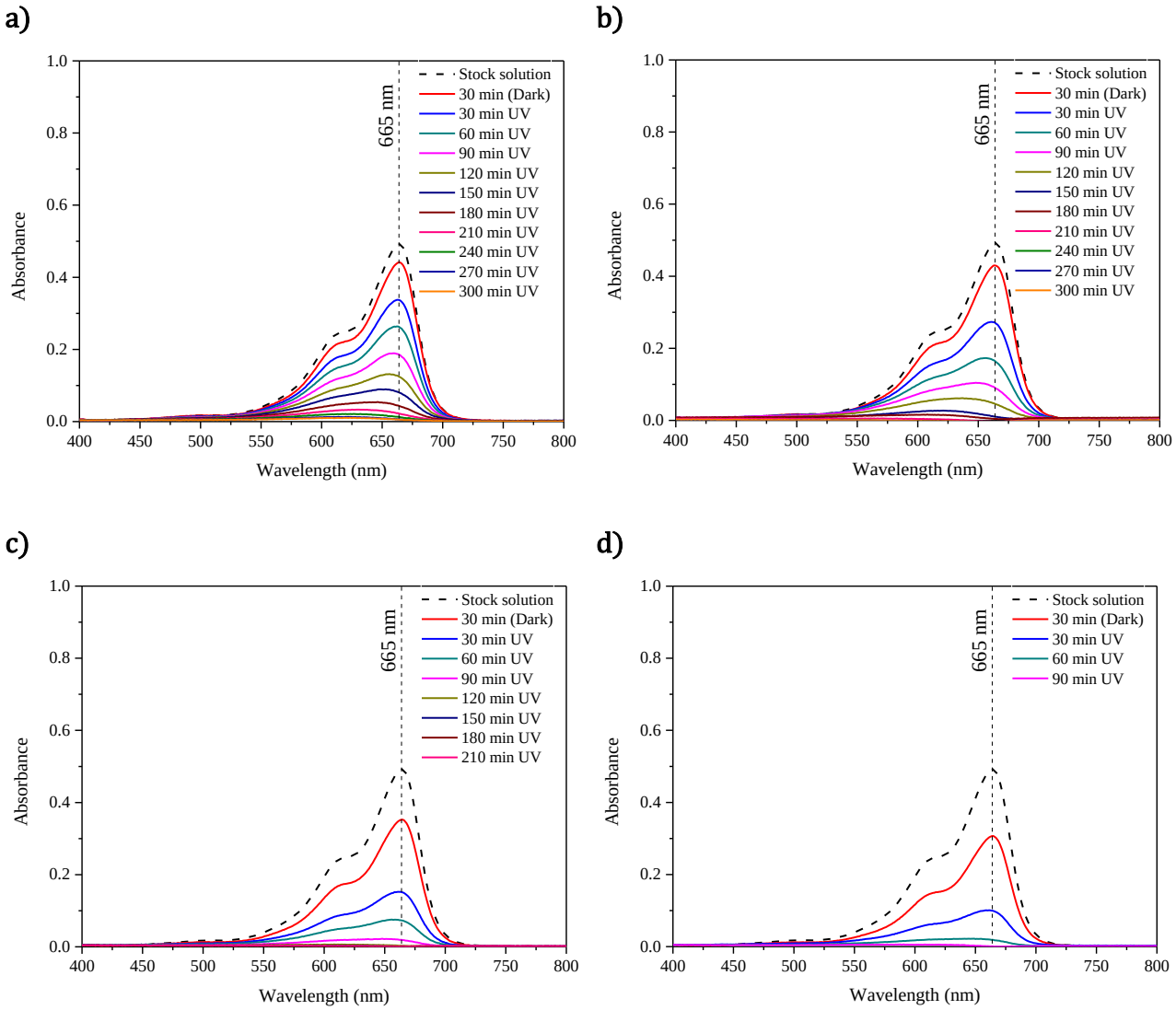

Figure 24 – Spectrum of absorbance comparison for the first use of **a)** 4x4 cm P(VDF-TrFE)/TiO_2 membrane; **b)** 5x5 cm P(VDF-TrFE)/TiO_2 membrane; **c)** 4x4 cm P(VDF-TrFE)/TiO_2/NaY membrane; **d)** 5x5 cm P(VDF-TrFE)/TiO_2/NaY membrane.

Figure 25 compares the degradation efficiency after a total of four uses under UV radiation. Pure P(VDF—TrFE) membranes were also tested and, as expected, did not reveal photocatalytic activity [ANNEX D]. These membranes serve as controls for the degradation tests.

The cost-effectiveness of the photocatalytic process depends upon how many times a photocatalyst can be reused without decreasing its efficiency. It is also important to study the effect of the photo-catalyst's concentration on the photocatalytic activity of these nanocomposites, which was studied by the Teixeira *et. al.* [45]. The authors conclude that the highest TiO_2 concentration present higher degradation rates. The photocatalytic composites

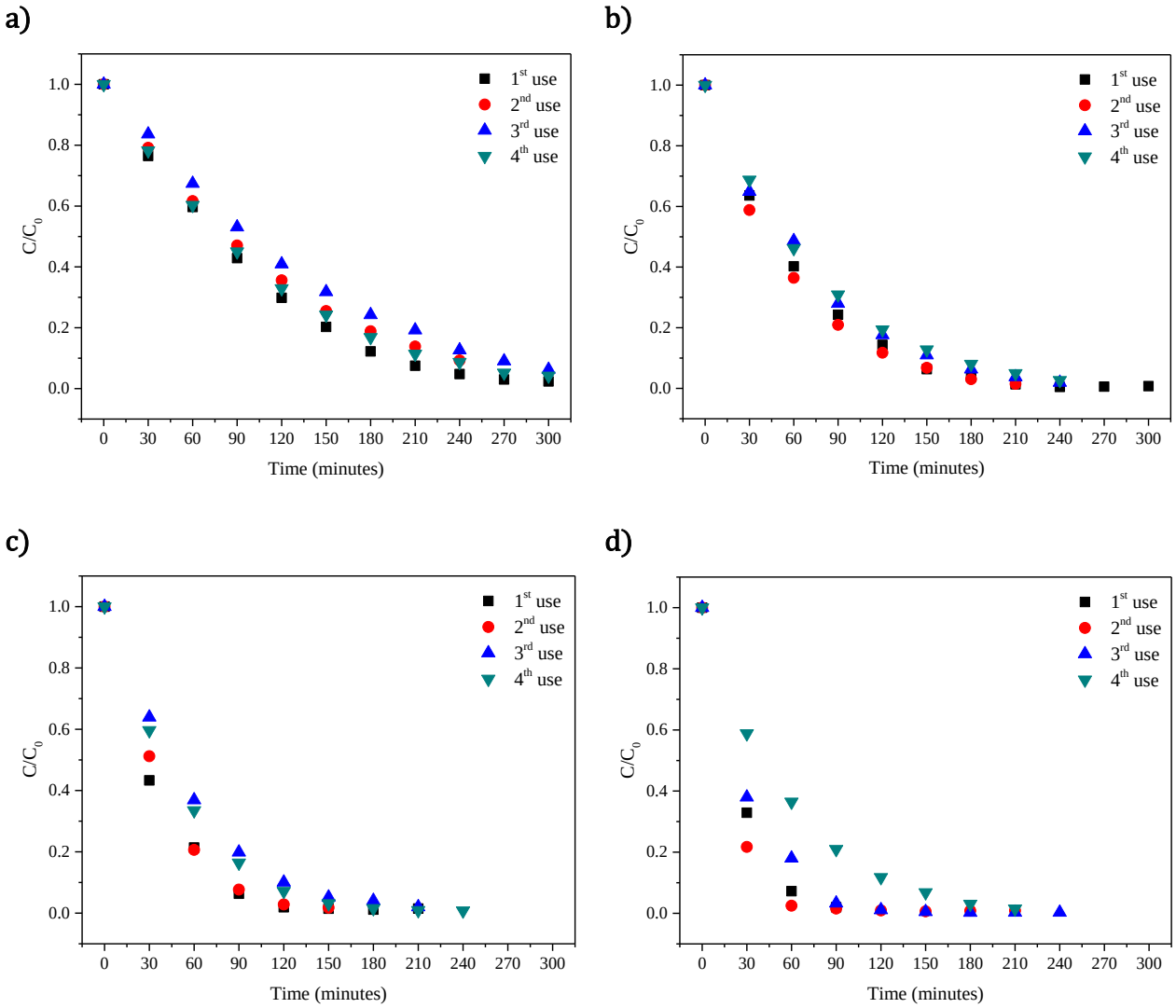

Figure 25 – Comparison of degradation efficiency kinetic curves after four uses for each sample using **a)** 4x4 cm P(VDF-TrFE)/TiO_2 membrane; **b)** 5x5 cm P(VDF-TrFE)/TiO_2 membrane; **c)** 4x4 cm P(VDF-TrFE)/TiO_2/NaY membrane; **d)** 5x5 cm P(VDF-TrFE)/TiO_2/NaY membrane.

under consideration do not show significant decrease in their activity when the experiments were repeated three times using the same sample.

As a simple means of comparison, the same amount of TiO_2 nanoparticles was directly added to a sample of 50 mL 2 mg L^{-1} MB solution and analysed after a total photocatalytic degradation time of 90 minutes using the microplate reader, as can be seen in the Figure 26.

Analysing the results obtained for TiO_2 in solution, the photocatalytic degradation was successful, having degraded 90% after 20 minutes, which are, as estimated, faster than the immobilized TiO_2 results. Although the curve presented in Figure 26.b is in between 0 and 90 minutes, for comparative purposes, it is not possible to correctly adjust a kinetic curve to all of

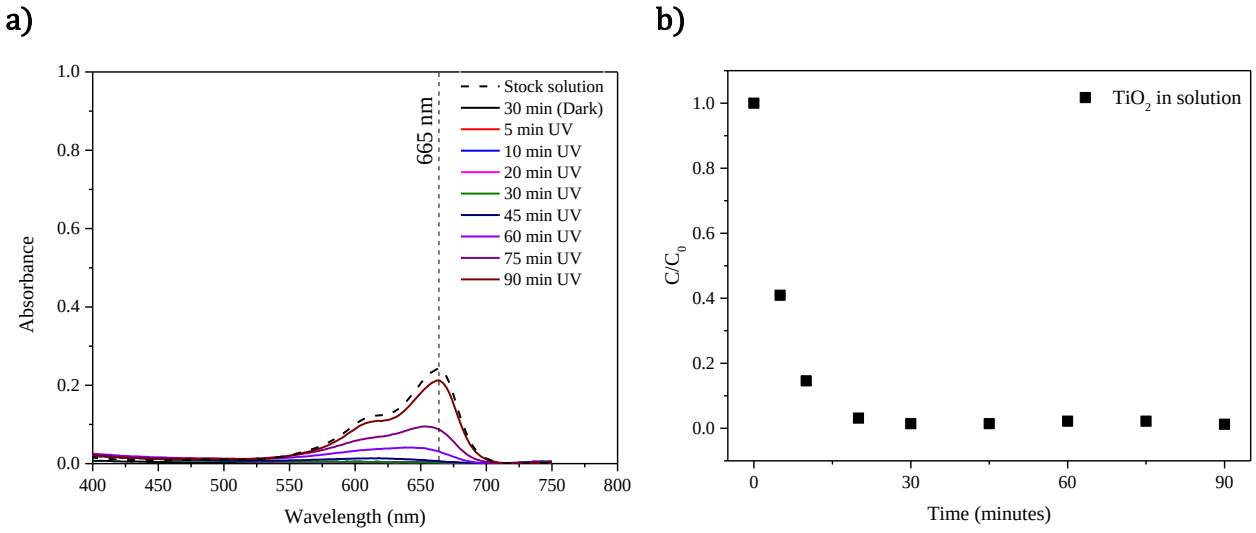

Figure 26 – a) Absorbance spectrum of MB degraded with TiO_2 nanoparticles in solution; **b)** kinetic degradation over time curve of MB with TiO_2 nanoparticles in solution.

the values in the graphic. Thus only the first few points were considered, until a proper kinetic curve was properly adjusted. The results are summarized in Table 6.

In Table 6, the best degradation results are highlighted in grey, belonging either to the first or second uses of each membrane.

Martins *et. al.* [73] degraded 10^{-5} M of MB using 8% TiO_2 and 8% TiO_2 with 3% NaY Immobilized in P(VDF-TrFE) and, similarly to the proposed composites in this study, obtained a reaction rate of 0.37 and 0.23 min^{-1} and degradation of 99 and 91%, respectively, after 90 minutes, Martins *et. al.* [13] obtained a reaction rate of 0.012 min^{-1} with 81% after 100 min with TiO_2 and Teixeira *et. al.* [45] obtained a reaction rate of 0.18 min^{-1} for composites with 10% of TiO_2. A reaction rate of 0.056 and 0.079 min^{-1} and a degradation of 92% and 97% for 0.005 g and 0.01 g of TiO_2 in suspension, respectively, was obtained in the work by Göbel *et. al.* [24].

Table 6 – Results of photocatalytic degradation of MB with immobilized TiO_2, with A being the percentage of Adsorption, D the percentage of degradation, $t_{90\%}$ the time at which the micropollutant had was degraded more than 90%, k the degradation rate and R^2 the adjust for k.

TYPE	SIZE (cm)	USE	A (%)	D (%)	$t_{90\%}$ (min)	k (min^{-1})	R^2
P(VDF-TrFE) /TiO_2	4x4	1	**11**	**98**	**210**	**0.013**	0.991
		2	**11**	**91**	**240**	**0.010**	0.995
		3	**14**	**94**	**270**	**0.009**	0.991
		4	**15**	**96**	**240**	**0.011**	0.996
	5x5	1	**13**	**99**	**150**	**0.019**	0.97
		2	**18**	**99**	**150**	**0.020**	0.993
		3	**4**	**98**	**180**	**0.016**	0.994
		4	**15**	**97**	**180**	**0.015**	0.996
P(VDF-TrFE) /TiO_2 /NaY	4x4	1	**38**	**99**	**90**	**0.023**	0.90
		2	**29**	**98**	**90**	**0.028**	0.991
		3	**25**	**98**	**150**	**0.019**	0.994
		4	**27**	**99**	**120**	**0.022**	0.988
	5x5	1	**38**	**98**	**60**	**0.044**	0.997
		2	**58**	**99**	**60**	**0.021**	0.90
		3	**27**	**99**	**90**	**0.027**	0.91
		4	**33**	**99**	**150**	**0.020**	0.993

4.2.2. CIPROFLOXACIN

A solution of 5 mg L^{-1} CIP was degraded by 5x5 cm nanocomposite membranes. The results of the photocatalytic degradation of CIP for the first use of the immobilized (with and without NaY) and the suspended TiO_2 nanoparticles can be observed in the absorbance spectra given in Figure 27 as well as the respective degradation curves for four reuses of the membranes.

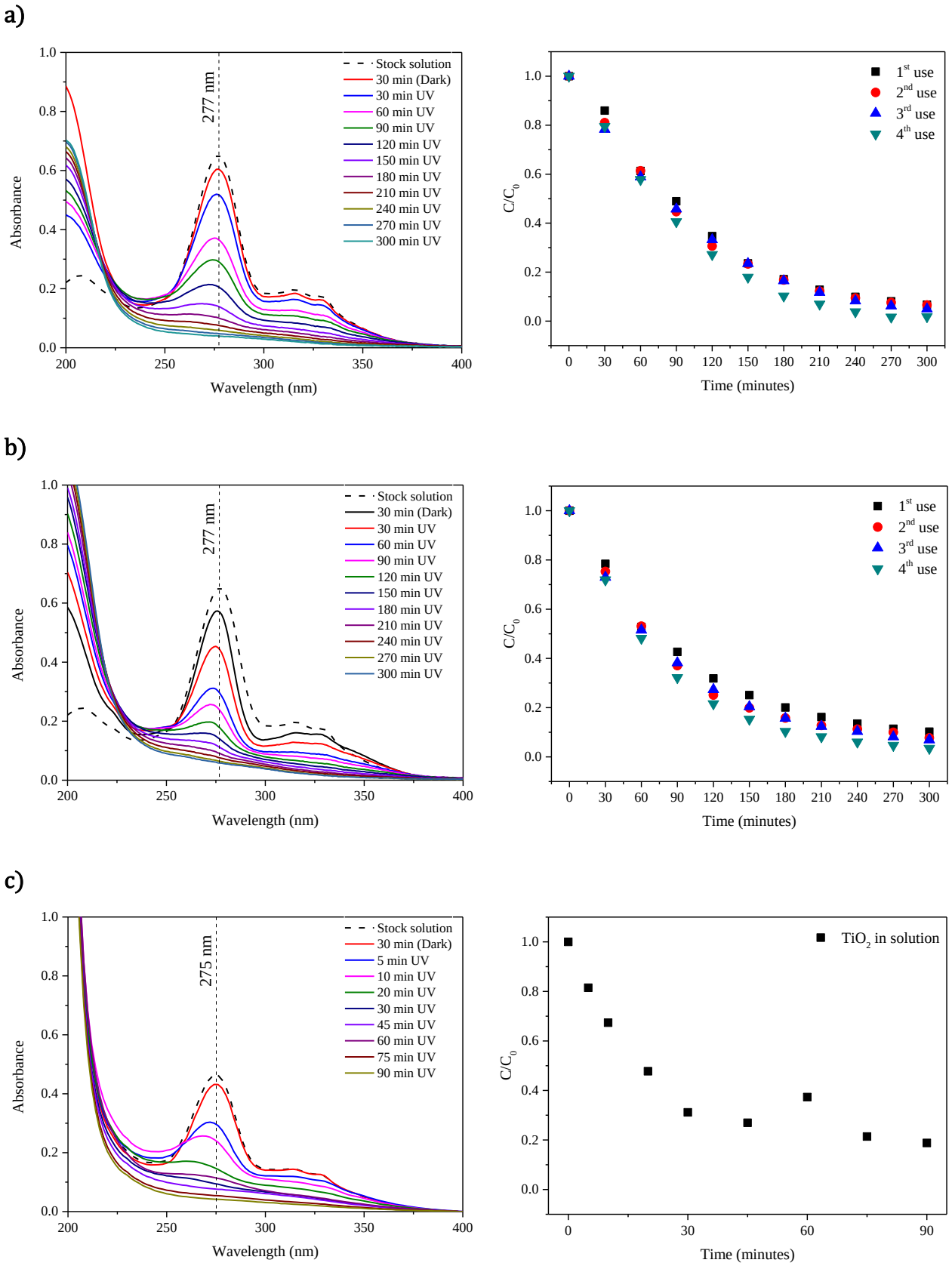

Figure 27 – Absorbance spectrums and degradation over time curves of CIP degraded with **a)** 5x5 cm P(VDF-TrFE)/TiO_2 membrane; **b)** 5x5 cm P(VDF-TrFE)/TiO_2/NaY membrane; **c)** TiO_2 nanoparticles in solution.

As observed in the spectra in Figure 27, the absorbance peak of CIP was at around 277 nm. All the samples were successfully degraded after the total time of exposure (300 minutes with immobilized TiO_2 and 90 min for suspended TiO_2). The value of absorbance 0.4 in solution for 60 minutes can be ignored, as it was influenced by an error in the absorbance measurement. Membranes with zeolites show a slightly higher absorbance percentage, when comparing with the membranes without zeolites. Reaction rate values seem to favour the membranes after utilizations, though the difference is not significant. The results are summarised in Table 7.

Table 7 – Results of photocatalytic degradation of CIP with immobilized TiO_2, with A being the percentage of Adsorption, D the percentage of degradation, $t_{90\%}$ the time at which the micropollutant had was degraded more than 90%, k the degradation rate and R^2 the adjust for k.

TYPE	SIZE (cm)	USE	A (%)	D (%)	$t_{90\%}$ (min)	k (min^{-1})	R^2
P(VDF-TrFE) /TiO_2	5x5	1	**7**	**93**	**240**	**0.010**	0.993
		2	**13**	**93**	**240**	**0.010**	0.994
		3	**9**	**95**	**240**	**0.010**	0.997
		4	**17**	**98**	**210**	**0.015**	0.98
P(VDF-TrFE) /TiO_2/NaY	5x5	1	**12**	**90**	**300**	**0.008**	0.98
		2	**13**	**92**	**270**	**0.009**	0.97
		3	**22**	**93**	**270**	**0.009**	0.97
		4	**26**	**97**	**210**	**0.011**	0.993

In Table 7, the best degradation results are highlighted in grey, surprisingly belonging to the fourth and final use of each membrane. In the first utilization, the membrane with TiO_2 degraded a total of 93%, while in the fourth reutilization the value rose to 98%. Similarly, the reaction rate value also increased from 0.010 to 0.015 min^{-1}. The same was verified in the membrane with zeolites, where the degradation increased from 90 to 97% and the reaction rate increased from 0.008 to 0.011 min^{-1}. Also contrary to what was observed with the degradation of MB, the membrane without zeolites performed better, although the zeolites still possess a higher percentage of adsorbance.

Silva *et. al.* [61] degraded 85% of 300 mg L^{-1} of CIP from water in 6 minutes using 1.0 g L^{-1} of suspended TiO_2 nanoparticles and UV.

4.2.3. IBUPROFEN

Nanocomposite membranes of dimensions 5x5 cm were used to degrade a solution of 15 mg L^{-1} of IBP. The results for the first use of immobilized (with and without NaY) and suspended TiO_2 nanoparticles can be observed in the absorbance spectra of Figure 28, as well as the respective degradation curves for four uses (three reuses) of the membranes.

Although Sigma-Aldrich reference sheet for IBP has 260 nm as the main absorbance peak, the results show the presence of a peak near 220 nm. This peak lowers with increasing reaction time, indicating that the compound is being degraded. At the same time though, there seems to be a peak near 260 nm rising, probably the indication of by-products being formed during the photocatalytic reaction. This second peak is not visible in the results by solution,

a)

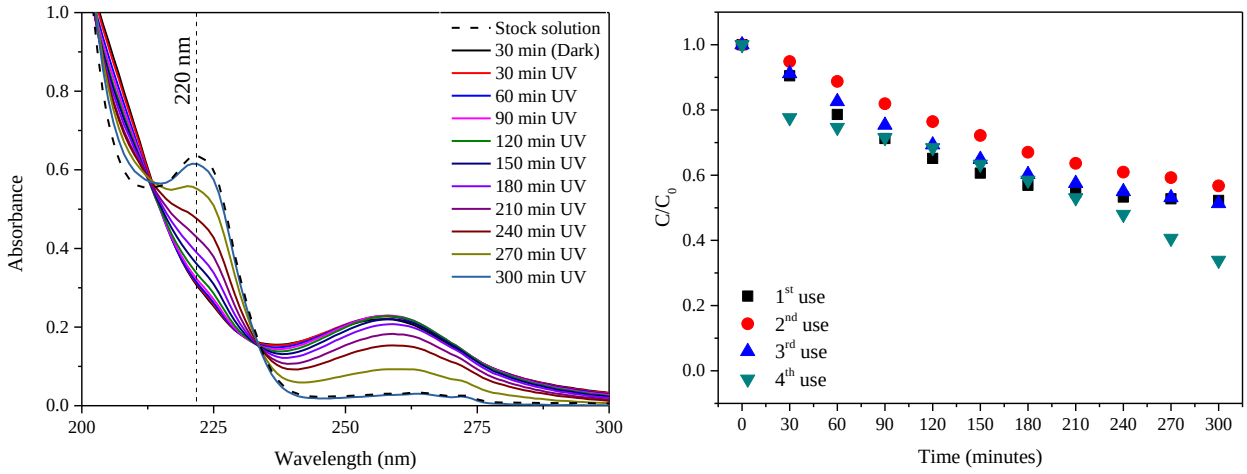

b)

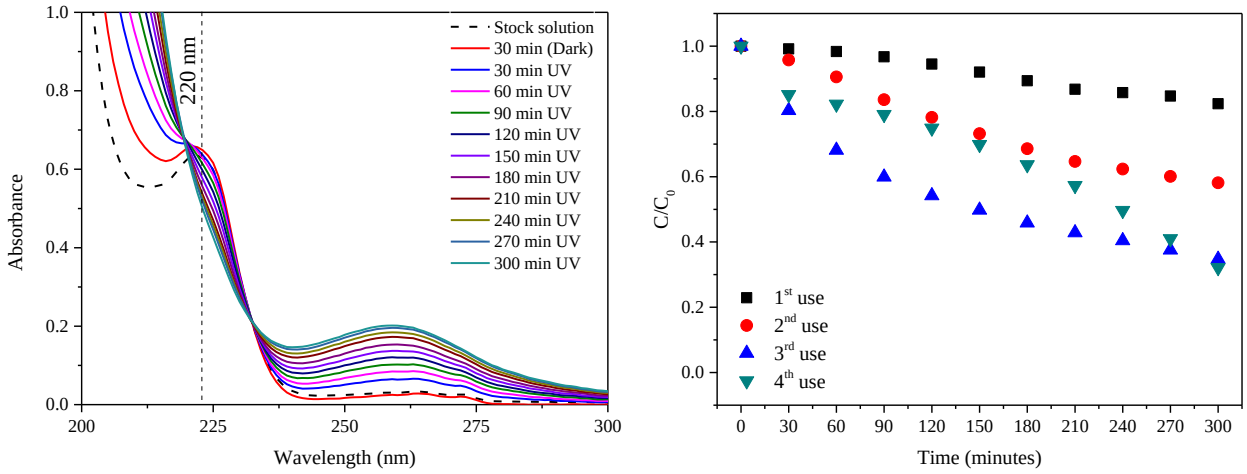

c)

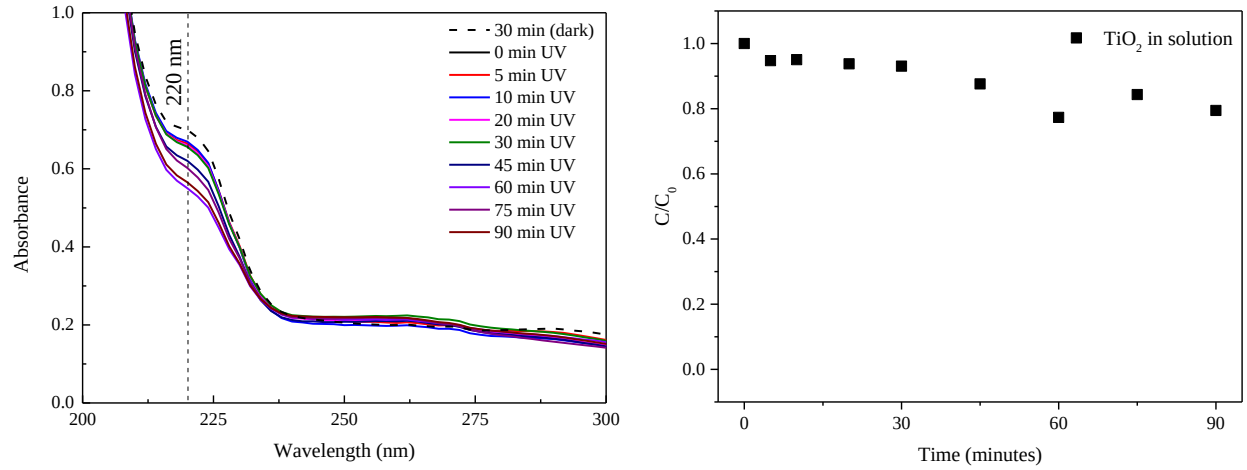

Figure 28 – Absorbance spectrums and degradation over time curves of IBP degraded with **a)** 5x5 cm P(VDF-TrFE)/TiO_2 membrane; **b)** 5x5 cm P(VDF-TrFE)/TiO_2/NaY membrane; **c)** TiO_2 nanoparticles in solution.

where only a small percentage of degradation took place, as can be observed by the decrease of the IBP maximum absorbance peak. To see if these by-products were further degraded, the samples were left under UV and agitation for a total time of 24 hours, as seen in Figure 29.

a) b)

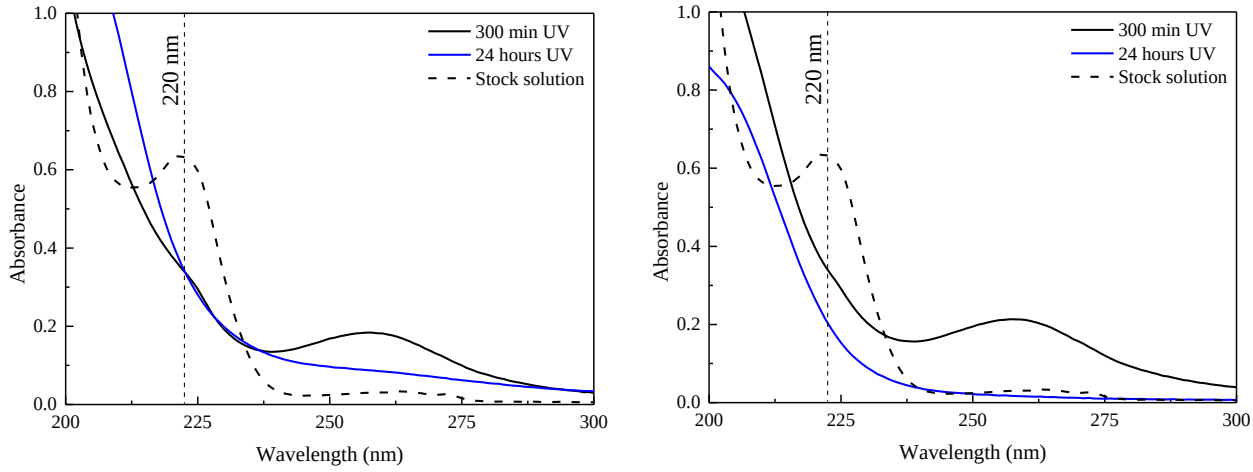

Figure 29 - Absorbance spectrum of the first reused (second use) membranes degradation of IBP and its by-products generated through the photocatalytic reaction, using a membrane with **a)** P(VDF-TrFE)/TiO_2; **b)** P(VDF-TrFE)/TiO_2/NaY.

It is clear that even the by-products generated were eventually degraded, as the maximum absorbance peak located at 260 lost intensity after 24 hours of UV exposure, indicating total degradation. The results are summarized in Table 8.

Table 8 – Results of photocatalytic degradation of IBP with immobilized TiO_2, with A being the percentage of Adsorption, D the percentage of degradation, $t_{90\%}$ the time at which the micropollutant had was degraded more than 90%, k the degradation rate and R^2 the adjust for k.

TYPE	SIZE (cm)	USE	A (%)	D (%)	$t_{90\%}$ (min)	k (min^{-1})	R^2
P(VDF-TrFE) /TiO_2	5x5	1	**3**	**48**	**-**	**0.003**	0.96
		2	**1**	**43**	**-**	**0.002**	0.985
		3	**10**	**49**	**-**	**0.003**	0.95
		4	**22**	**66**	**-**	**0.003**	0.94
P(VDF-TrFE) /TiO_2/NaY	5x5	1	**3**	**18**	**-**	**0.001**	0.98
		2	**1**	**42**	**-**	**0.002**	0.987
		3	**17**	**65**	**-**	**0.003**	0.96
		4	**15**	**68**	**-**	**0.003**	0.93

In Table 8, the best degradation results are highlighted in grey, surprisingly belonging to the fourth and final use of each membrane. Contrary to the results obtained from MB, but similar to CIP, the overall efficiency seems to improve after the utilization of the membrane, as evidenced by the results in In Table 8. After the 4^{th} use, the membrane with TiO_2 degraded a total of 66% of IBP, while the membrane with zeolites degraded 68% of IBP, both with a degradation rate of 0.003 min^{-1}. The P(VDF-TrFE)/TiO_2 membrane adsorbed 22% of IBP in the first 30 minutes in the dark, implying the final degradation results might have also been influenced, while the P(VDF-TrFE)/TiO_2/NaY membrane adsorbed 15%. The increase of efficiency obtained from the latter, as was observed in the SEM images previously discussed, can be due to, not just the increase of pore size and interconnectivity, which increases percolation, but also to the re-disposition of the particles after the membranes have been used, meaning the micropollutants have an increase area in which to attach themselves to the TiO_2 nanoparticles, consequently increasing the photocatalytic activity.

El-Sheikh *et. al.* [112] degraded 99% of 20 mg L^{-1} of IBP in 2 hours under UV using Carbon and nitrogen co-doped mesoporous TiO_2, although there was no indication of the 220 nm peak.

4.2.4. BISPHENOL A

Degradation of a solution containing 45 mg L^{-1} of BPA was attempted with 5x5 cm nanocomposite membranes. The results for the first use of immobilized (with and without NaY) and suspended TiO_2 nanoparticles can be observed in the absorbance spectra in Figure 30, as well as the respective degradation curves for two uses (one reuse) of the membranes.

By observing Figure 30.a and Figure 30.b, no visible degradation took place at the maximum absorbance peak located at 277 nm, though degradation did occur around it. Similarly, no visible degradation of BPA occurred in the results obtained by suspended TiO_2 nanoparticles (Figure 30.c)), as the maximum absorption peak did not exhibit any significant change in value. All of the kinetic curves are similar to the controls in [Annex D].

a)

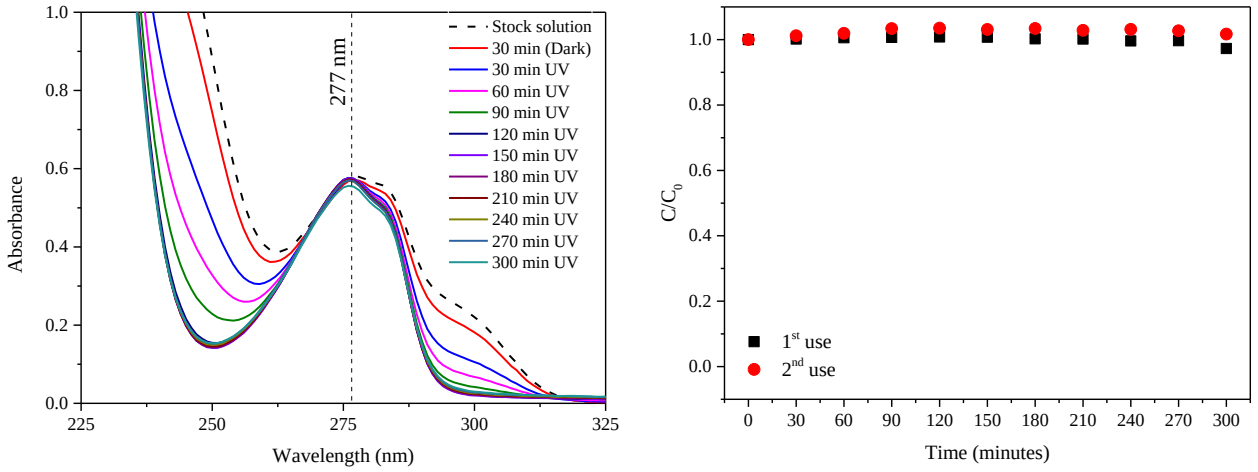

b)

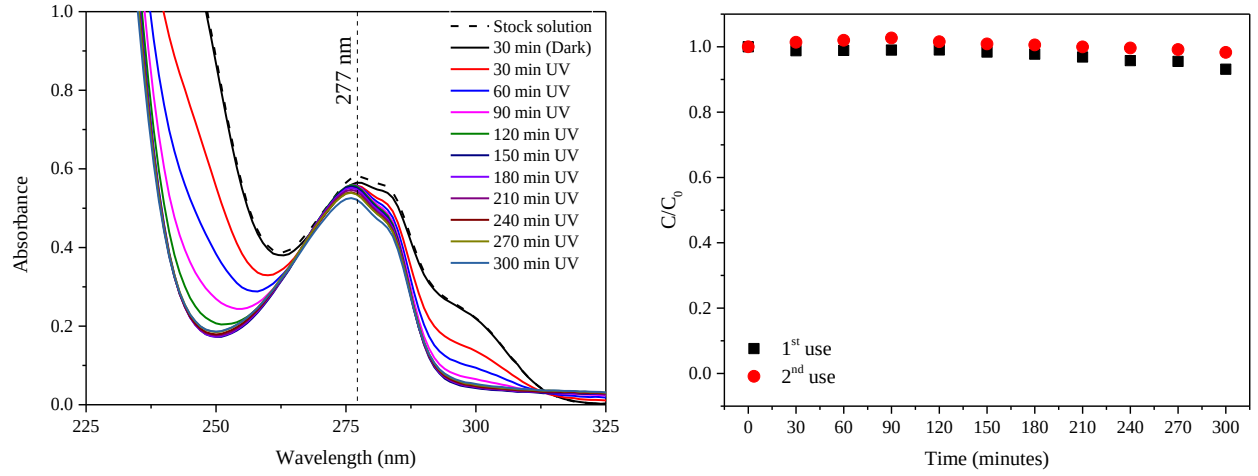

c)

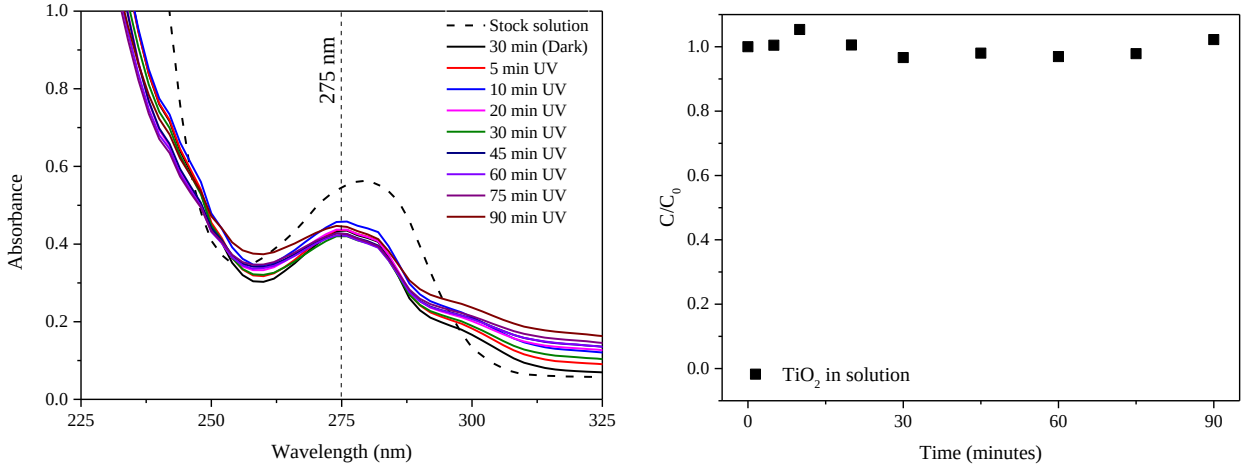

Figure 30 – Absorbance spectra and degradation over time curves of BPA degraded with **a)** P(VDF-TrFE)/TiO_2 membrane; **b)** P(VDF-TrFE)/TiO_2/NaY membrane; **c)** TiO_2 nanoparticles in solution.

The degradation results can be summarized in Table 9.

Table 9 – Results of photocatalytic degradation of BPA with immobilized TiO_2, with A being the percentage of Adsorption, D the percentage of degradation, $t_{90\%}$ the time at which the micropollutant had was degraded more than 90%, k the degradation rate and R^2 the adjust for k.

TYPE	SIZE (cm)	USE	A (%)	D (%)	$t_{90\%}$ (min)	k (min^{-1})	R^2
P(VDF-TrFE)/TiO_2	5x5	1	2	3	-	-	-
		2	1	2	-	-	-
P(VDF-TrFE)/TiO_2/NaY	5x5	1	3	7	-	-	-
		2	2	2	-	-	-

Through observation of Table 9, the membrane with TiO_2 degraded 3% of BPA over 300 minutes in its first utilization, while the membrane with zeolites degraded a total of 7% of BPA. Because no degradation took place, it made it impossible to fit a pseudo-first-order curve and calculate the reaction rate. Moreover, reusability is also excluded and the membranes were only used two times.

Because BPA is recalcitrant, it cannot be readily removed from the water, due to its complex aromatic molecular structure and low biodegradability. It is unclear what mechanism is responsible for this, however, there are several possibilities, such as heterogeneous aggregates, that contain anaerobic zones, and the non-reversible sorption of compounds into the biosolids matrix, resulting in decreased availability for microbial degradation [72], [113].

Studies have reported that the concentration of contaminants in water greatly influences the photocatalytic reaction rate of TiO_2, as does varying the pH, temperature, light intensity and catalyst concentration, greatly influences the efficiency of photocatalytic degradation. Although using similar operating conditions, varying the initial concentration of the pollutants results in different irradiation times necessary to achieve a complete degradation. This may be due to the saturation of the TiO_2 surface and reduction of the photonic efficiency, which leads to the deactivation of the photocatalyst [3], [18], [46], [63], [114], [115]. Kaneco *et. al.* [18] have successfully degraded $\simeq$ 60% of 1 mg L^{-1} of BPA in 60 minutes with 10 mg L^{-1} of suspended TiO_2 nanoparticles, a solar light intensity of 1.3 mW cm^{-2} ($\lambda = 320 - 410$ nm), temperature of 30 ◦C and pH of 6. Wang *et. al.* [46] degraded $\simeq$ 97% of 10 mg L^{-1} BPA after 6 hours of UV, using 1% of TiO_2 immobilized on polyurethane foam, at pH of 12.3, and temperature of 24.3 ◦C. Chiang *et.* al. [114] found that 20 mg L^{-1} of BPA was completely mineralized into CO_2 after 120 minutes of UV, using 0.1 g L^{-1} of platinized TiO_2, at pH of 3. Finally, Erjavec *et. al.* [64] degraded 20% of 4.38×10^{-5} mol L^{-1} BPA after 400 minutes, using glass fibre supported TiO_2,

4.2.5. FINAL CONSIDERATIONS

Comparing all the obtained results for the four studied micropollutants, at the different studied conditions, each compound presented different results in the TiO_2 photocatalysis reaction. Table 10 and Table 11 contain the first utilizations of TiO_2 in immobilization and solution, respectively, with the corresponding results.

Table 10 – Results of the first photocatalytic degradation of MB, CIP, IBP and BPA with 5x5 cm P(VDF-TrFE) membranes with immobilized TiO_2, with A being the percentage of Adsorption, D the percentage of degradation, $t_{90\%}$ the time at which the micropollutant had was degraded more than 90%, k the degradation rate and R^2 the adjust for k.

		A (%)	D (%)	$t_{90\%}$ (min)	k (min^{-1})	R^2
MB	TiO_2	13	99	150	0.019	0.97
	TiO_2/NaY	38	98	60	0.044	0.987
CIP	TiO_2	7	93	240	0.010	0.993
	TiO_2/NaY	12	90	300	0.008	0.98
IBP	TiO_2	3	48	-	0.003	0.96
	TiO_2/NaY	3	18	-	0.001	0.98
BPA	TiO_2	2	3	-	-	-
	TiO_2/NaY	3	7	-	-	-

Table 11 – Results of photocatalytic degradation of MB, CIP, IBP and BPA with TiO_2 in solution, with A being the percentage of Adsorption, D the percentage of degradation, $t_{90\%}$ the time at which the micropollutant had was degraded more than 90%, k the degradation rate and R^2 the adjust for k.

	A (%)	D (%)	$t_{90\%}$ (min)	k (min^{-1})	R^2
MB	12	99	20	0.177	0.995
CIP	2	81	-	0.033	0.95
IBP	10	21	-	0.003	0.8
BPA	19	3	-	0.0005	0.987

The dye MB degraded more efficiently than the other compounds. Degradation of CIP and IBP seemed to improve after the membranes were reused. The degradation of IBP seemed to generate by-products that were eventually degraded as well. BPA was the only

micropollutant that was not degraded, not only by TiO_2 nanoparticles in solution, but also with the nanocomposite membranes. Even so, the reutilization of the membranes was successfully achieved in the sense that the results did not vary significantly between uses. The decrease in the photocatalytic performance of the membranes during its reuse might be due to the loss of TiO_2 particles and/or the accumulation of intermediates with a poisoning effect on the surface of the nanocomposites [45]. Both were not completely proved, even though SEM images showed no difference before and after utilization in MB, which means no considerable TiO_2 loss took place, though the membrane was not studied in relation to mass loss. No additional bands were seen in the FTIR spectra of MB after utilization, the membranes would have to be further analysed for contamination. The increase in efficiency after the reuse of the membranes in the degradation of CIP and IBP can be due to the increase in membrane pore size and re-dispersion of the TiO_2 nanoparticles within the pores, increasing the contact area between the pollutant and the catalyst.

Overall, the results show that the prepared membranes offer a suitable platform for photocatalytic degradation of micropollutants, allowing reusability.

5. Conclusions and Future Perspectives

In this Chapter, the most relevant conclusions of this work are presented, as are suggestions that could help the development and application of future works.

5.1. CONCLUSIONS

Due to the increase of water pollution and the impending need for clean and inexpensive water treatment processes, photocatalysis has risen as viable technology for water treatment. The main goal of the present work was to develop photocatalytic membranes for the removal of micropollutants from wastewater. Thus, immobilised TiO_2 nanoparticles were tested on the degradation of four compounds, methylene blue, ciprofloxacin, ibuprofen and bisphenol A.

Regarding TiO_2 nanoparticles characterization, the X-ray diffraction patterns indicated in the anatase and rutile phases, the obtained particle hydrodynamic diameter was 430 ± 28 nm, which is significantly above the estimated value by SEM of 33.8 ± 10.8 nm.

Afterwards, the nanocomposite membranes of P(VDF-TrFE) with 8% wt. of TiO_2 nanoparticles with and without 3% wt. NaY zeolites, in order to tailor the wettability of the membrane, were successfully produced and characterized. The composites showed good chemical stability, easy synthesis and adaptability. P(VDF-TrFE) crystallization induced the formation of β–phase, independently of the presence and content of nanoparticles, and no chemical bonds were detected between the polymer and the incorporated nanoparticles. The chemical structure of the membranes was intact after four long periods of time under UV.

All the produced membranes possess a porous structure, porosity level above 70%, with similar spherical pores, independent of the presence of nanoparticles. The interconnectivity between these pores favours percolation and eases the reach of the pollutant nanoparticles. TiO_2 nanoparticles were observed inside the pores, both before and after four photocatalytic utilizations and membrane cleaning, meaning nanoparticle loss did not occur. A wider distribution of the nanoparticles throughout the pores was observed, indicating they were re-dispersed after four utilizations. The membrane with TiO_2 nanoparticles shows the highest values of pore size, of 80 ± 70 μm and the smallest values in porosity, 74 ± 3 %. The membrane with zeolites shows the highest porosity, at 89 ± 5 %, and at the smallest avarage pore size, at 30 ± 20 μm, with visible pores inside pores and high interconnectivity. After use, the pores became bigger, with values ranging from 10 and 190 μm, which can be due to the contact with water, which promotes pore expansion. Concerning the nanocomposites wettability, the

pristine membrane is the most hydrophobic, with angles of 98.6° and 75.7°, for 0 and 10 minutes of drop deposition, respectively. The membrane with TiO_2 nanoparticles displayed a more hydrophilic behaviour in relation to the pristine membrane. The presence of TiO_2 nanoparticles favours the absorption of water by the membrane and, with their UV-induced super-hydrophilic behaviour, alters the hydrophobic nature of the P(VDF-TrFE) membranes. The P(VDF-TrFE)/TiO_2/NaY membrane presented the most hydrophilic results, before and after UV exposure.

With respect to MB and CIP, successful photocatalytic degradation and membrane utilization was achieved. All samples were degraded above 90%, with better MB results obtained with a 5x5 cm membrane with zeolites, which degraded a total of 98%, with a reaction rate of 0.044 min^{-1}. In relation to CIP the membranes with TiO_2 obtained better results, with a total of 93% of degradation and a reaction rate of 0.010 min^{-1}. Interestingly, the efficiency increases after membrane reutilization, with the same membrane degrading 98% with a reaction rate of 0.15 min^{-1} in its fourth reutilization.

In terms of IBP, degradation showed interesting results due to the possible formation of by-products during the photocatalytic reaction. The best results belong to the 5x5 cm TiO_2 membrane, which degraded 48% of IBP with a degradation rate of 0.003 min^{-1}, which in turn, similar to CIP, showed a slight efficiency increase after reutilization, where, in the fourth use, 66% of IBP was degraded, with a similar reaction rate. Concerning BPA, a total of 7% was degraded using a 5x5 cm membrane with zeolites. BPA was not completely degraded, although some changes in the spectra were observed over time. In this work a high initial concentrations of the pollutants was used, which are far from those found in environmental matrices, leading to the conclusion that, by changing conditions such as pollutant concentration, further information might be obtained.

However, the membrane with best performance corresponds to an efficiency loss comparatively to the respective assay with nanoparticles in suspension although the final solution does not need any posterior treatment. The results lead us to conclude that the photocatalytic activity is due to the TiO_2 nanoparticles, while the presence of zeolites leads to the hydrophilic behaviour of the membranes.

The process herein described is cost-effective and has high potential for the water treatment at higher scale as the catalyst is immobilised, so easily kept in the photoreactors, and can be reused.

5.2. FUTURE WORK

Despite the fact that combined methods are not a very common practice, they are still one of the most powerful processes for the removal of many micropollutants from the water [5]. In terms of practicality, a combination of processes, such as adsorption and photocatalysis, could be a good solution for the treatment of effluents containing pharmaceuticals, as the membranes can be cleaned after each use. Furthermore, the application of these membranes is not limited to water treatment. As stated by the authors in [13], the photocatalytic performance of the membranes can also be applied in sensors and/or actuators.

In scope of this work, the next step would be to optimize a photoreactor and the ideal conditions for the photocatalytic process herein described. More analysis had to be made in order to also confirm the toxicity of the degradation by-products obtained through this process, specifically for Ibuprofen and Bisphenol A and test their degradations at lower concentrations. Another possibility would be the degradation of various more micropollutants, in order to test the overall effectiveness and efficiency based on type of reagents.

Another objective should also be the application of the process in grander scale reactors, with higher quantity of micropollutants, and, subsequently, designing the most effective disposition of the membranes for a successful photocatalytic degradation. The aim of system optimization also touches upon to difficulty of grand-scale UV photoreactors, as UV lamps are expensive and energy consuming. Visible radiation presents itself as an alternative, as it is available naturally and indefinitely. Current investigations focus on moving the active wavelength of a material into the range of visible light. In this sense, photocatalysis is a promising alternative technology for the removal of organic pollutants in water or other matrices, particularly at low concentrations [31], [49]. Because TiO_2 electrons do not absorb photons with wavelength in the range of visible radiation, TiO_2 nanoparticles would have to be doped. As such, the membranes would need to be studied in relation to the incorporation of these doped nanoparticles and, eventually, their application in photocatalytic degradation of micropollutants.

REFERENCES

[1] C. Yu, W. Zhou, H. Liu, Y. Liu, and D. D. Dionysiou, 'Design and fabrication of microsphere photocatalysts for environmental purification and energy conversion', *Chemical Engineering Journal*, vol. 287, pp. 117–129, 2016.

[2] S. Yang *et al.*, 'Polypropylene membrane surface modification by RAFT grafting polymerization and TiO_2 photocatalysts immobilization for phenol decomposition in a photocatalytic membrane reactor', *Separation and Purification Technology*, vol. 83, no. 1, pp. 157–165, 2011.

[3] M. N. Chong, B. Jin, C. W. K. Chow, and C. Saint, 'Recent developments in photocatalytic water treatment technology: A review', *Water Research*, vol. 44, no. 10, pp. 2997–3027, 2010.

[4] M. Klavarioti, D. Mantzavinos, and D. Kassinos, 'Removal of residual pharmaceuticals from aqueous systems by advanced oxidation processes', *Environment International*, vol. 35, no. 2, pp. 402–417, 2009.

[5] V. Homem and L. Santos, 'Degradation and removal methods of antibiotics from aqueous matrices - A review', *Journal of Environmental Management*, vol. 92, no. 10, pp. 2304–2347, 2011.

[6] 'Micropollutants in municipal wastewater', Bern, 2012.

[7] M. Hijosa-Valsero *et al.*, 'Removal of antibiotics from urban wastewater by constructed wetland optimization', *Chemosphere*, vol. 83, no. 5, pp. 713–719, 2011.

[8] S. Ahmed, M. G. Rasul, W. N. Martens, R. Brown, and M. A. Hashib, 'Heterogeneous photocatalytic degradation of phenols in wastewater: A review on current status and developments', *Desalination*, vol. 261, no. 1–2, pp. 3–18, 2010.

[9] S. Malato, P. Fernández-Ibáñez, M. I. Maldonado, J. Blanco, and W. Gernjak, 'Decontamination and disinfection of water by solar photocatalysis: Recent overview and trends', *Catalysis Today*, vol. 147, no. 1, pp. 1–59, 2009.

[10] T. Wintgens, F. Salehi, R. Hochstrat, and T. Melin, 'Emerging contaminants and treatment options in water recycling for indirect potable use', *Water Science and Technology*, vol. 57, no. 1, pp. 99–107, 2008.

[11] S. D. Richardson, 'Environmental Mass Spectrometry: Ermerging Contaminants and Current Issues', *Analytical Chemistry*, vol. 80, no. 12, pp. 4373–4402, 2008.

[12] S. Suárez, M. Carballa, F. Omil, and J. M. Lema, 'How are pharmaceutical and personal care products (PPCPs) removed from urban wastewaters?', *Reviews in Environmental Science and Biotechnology*, vol. 7, no. 2, pp. 125–138, 2008.

[13] P. M. Martins *et al.*, 'Improving Photocatalytic Performance and Recyclability by Development of Er-Doped and Er / Pr-Codoped TiO_2/ Poly (vinylidenedifluoride)—Trifluoroethylene Composite Membranes', *Journal of Physical Chemistry C*, vol. 118, p. 27944—27953, 2014.

[14] M. Klavarioti, D. Mantzavinos, and D. Kassinos, 'Removal of residual pharmaceuticals from aqueous systems by advanced oxidation processes', *Environment International*, vol. 35, no. 2, pp. 402–417, 2009.

[15] P. Wexler, *Encyclopedia of Toxicology*, 3rd ed. Academic Press, 2014.

[16] S. T. Odonkor and K. K. Addo, 'Resistance to Antibiotics : Recent Trends and Challenges', *International Journal of Biological and Medical Research*, vol. 2, no. 4, pp. 1204–1210, 2011.

[17] J. Jin, Y. Wang, H. Liu, and Z. Zhang, 'Determination and calculation of solubility of bisphenol A in supercritical carbon dioxide', *Chemical Engineering Research and Design*, vol. 91, no. 1, pp. 158–164, 2013.

[18] S. Kaneco, M. A. Rahman, T. Suzuki, H. Katsumata, and K. Ohta, 'Optimization of solar photocatalytic degradation conditions of bisphenol A in water using titanium dioxide', *Journal of Photochemistry and Photobiology A: Chemistry*, vol. 163, no. 3, pp. 419–424, 2004.

[19] A. V. Krishnan, P. Stathis, S. F. Permuth, L. Tokes, and D. Feldman, 'Bisphenol-A: An Estrogenic Substance In Released from Polycarbonate Flasks during Autoclaving', *Endocriminology*, vol. 132, no. 6, 2014.

[20] R. J. Witorsch, 'Low-dose in utero effects of xenoestrogens in mice and their relevance to humans: An analytical review of the literature', *Food and Chemical Toxicology*, vol. 40, no. 7, pp. 905–912, 2002.

[21] O. A. Arikan, 'The fate of chlortetracycline during the anaerobic digestion of manure from medicated calves', *Environmental Earth Sciences*, vol. 158, pp. 1087–1096, 2011.

[22] N. M. Vieno, H. Härkki, T. Tuhkanen, and L. Kronberg, 'Occurrence of pharmaceuticals in river water and their elimination in a pilot-scale drinking water treatment plant', *Environmental Science and Technology*, vol. 41, no. 14, pp. 5077–5084, 2007.

[23] P. E. Stackelberg, J. Gibs, E. T. Furlong, M. T. Meyer, S. D. Zaugg, and R. L. Lippincott, 'Efficiency of conventional drinking-water-treatment processes in removal of pharmaceuticals and other organic compounds', *Science of the Total Environment*, vol. 377, no. 2–3, pp. 255–272, 2007.

[24] A. Göbel, C. S. McArdell, A. Joss, H. Siegrist, and W. Giger, 'Fate of sulfonamides, macrolides, and trimethoprim in different wastewater treatment technologies', *Science of the Total Environment*, vol. 372, no. 2–3, pp. 361–371, 2007.

[25] C. Adams, M. Asce, Y. Wang, K. Loftin, and M. Meyer, 'Removal of Antibiotics from Surface and Distilled Water in Conventional Water Treatment Processes', *Environmental Engineering*, no. MARCH, pp. 253–260, 2002.

[26] P. V. A. Padmanabhan *et al.*, 'Nano-crystalline titanium dioxide formed by reactive plasma synthesis', *Vacuum*, vol. 80, no. 11–12, pp. 1252–1255, 2006.

[27] U. I. Gaya and A. H. Abdullah, 'Heterogeneous photocatalytic degradation of organic contaminants over titanium dioxide: A review of fundamentals, progress and problems', *Journal of Photochemistry and Photobiology C: Photochemistry Reviews*, vol. 9, no. 1, pp. 1–12, 2008.

[28] R. Andreozzi, *Advanced oxidation processes (AOP) for water purification and recovery*, vol. 53, no. 1. 1999.

[29] M. A. Oturan and E. Brillas, 'Electrochemical Advanced Oxidation Processes (EAOPs) for Environmental Applications', vol. 25, pp. 1–18, 2007.

[30] X. . W. Zhao L.; Liu, D., 'Effect of several factors on peracetic acid pretreatment of sugarcane bagasse for enzymatic hydrolysis', *Journal of Chemical Technology & Biotechnology*, vol. 82, no. May, pp. 1115–1121, 2007.

[31] C. Schmoock *et al.*, 'S-layer proteins as possible immobilization matrix for photocatalysts - OH radical scavenging capacity and protein stability', *Journal of Photochemistry and Photobiology A: Chemistry*, vol. 277, pp. 12–18, 2014.

[32] A. Stocking, R. Rodriguez, T. Browne, and D. Ph, 'Advanced Oxidation Processes', *Evaluation*, vol. 32, no. 9–10, pp. 1031–41, 2011.

[33] H. Katsumata, S. Kawabe, S. Kaneco, T. Suzuki, and K. Ohta, 'Degradation of bisphenol A in water by the photo-Fenton reaction', *Journal of Photochemistry and Photobiology A: Chemistry*, vol. 162, no. 2–3, pp. 297–305, 2004.

[34] B. Tryba, 'Immobilization of TiO2 and Fe-C-TiO_2 photocatalysts on the cotton material for application in a flow photocatalytic reactor for decomposition of phenol in water', *Journal of Hazardous Materials*, vol. 151, no. 2–3, pp. 623–627, 2008.

[35] M. Silva *et al.*, 'Immobilization of halogenated porphyrins and their copper complexes in MCM-41: Environmentally friendly photocatalysts for the degradation of pesticides', *Applied Catalysis B: Environmental*, vol. 100, no. 1–2, pp. 1–9, 2010.

[36] B. P. Chaplin, 'Environmental Science Processes & Impacts Critical review of electrochemical advanced oxidation processes for water treatment applications', vol. 1, no. 312, pp. 1182–1203, 2014.

[37] M. R. Hoffmann, S. Martin, W. Choi, and D. W. Bahnemannt, 'Environmental Applications of Semiconductor Photocatalysis', *Chemical Reviews*, vol. 95, no. 1, pp. 69–96, 1995.

[38] A. R. Silva *et al.*, 'Ciprofloxacin wastewater treated by UVA photocatalysis: contribution of irradiated TiO_2 and ZnO nanoparticles on the final toxicity as assessed by Vibrio fischeri', *RSC Adv.*, pp. 95494–95503, 2016.

[39] R. Bott, 'Applications of Titanium Dioxide Photocatalysis to Construction Materials', *Igarss 2014*, no. 1, pp. 1–5, 2011.

[40] B. Wang, D. Gu, L. Ji, and H. Wu, 'Photocatalysis: A novel approach to efficient demulsification', *Catalysis Communications*, vol. 75, pp. 83–86, 2016.

[41] M. M. Halmann, *Photodegradation of Water Pollutants*. CRC Press, 1996.

[42] W. chao Peng, Y. Chen, and X. yan Li, 'MoS2/reduced graphene oxide hybrid with CdS nanoparticles as a visible light-driven photocatalyst for the reduction of 4-nitrophenol', *Journal of Hazardous Materials*, vol. 309, pp. 173–179, 2016.

[43] M. Akkari, P. Aranda, H. Ben Rhaiem, A. Ben Haj Amara, and E. Ruiz-Hitzky, 'ZnO/clay nanoarchitectures: Synthesis, characterization and evaluation as photocatalysts', *Applied Clay Science*, 2015.

[44] A. Yousef, N. A. M. Barakat, S. S. Al-Deyab, R. Nirmala, B. Pant, and H. Y. Kim, 'Encapsulation of CdO/ZnO NPs in PU electrospun nanofibers as novel strategy for effective immobilization of the photocatalysts', *Colloids and Surfaces A: Physicochemical and Engineering Aspects*, vol. 401, pp. 8–16, 2012.

[45] S. Teixeira, P. M. Martins, S. Lanceros-Méndez, K. Kühn, and G. Cuniberti, 'Reusability of photocatalytic TiO_2 and ZnO nanoparticles immobilized in poly(vinylidene difluoride)-co-trifluoroethylene', *Applied Surface Science*, vol. 384, pp. 497–504, 2016.

[46] R. Wang, D. Ren, S. Xia, Y. Zhang, and J. Zhao, 'Photocatalytic degradation of Bisphenol A (BPA) using immobilized TiO_2 and UV illumination in a horizontal circulating bed photocatalytic reactor (HCBPR)', *Journal of Hazardous Materials*, vol. 169, no. 1–3, pp. 926–932, 2009.

[47] K. Chiang, T. M. Lim, L. Tsen, and C. C. Lee, 'Photocatalytic degradation and mineralization of bisphenol A by TiO_2 and platinized TiO_2', *Applied Catalysis A: General*, vol. 261, no. 2, pp. 225–237, 2004.

[48] K. Thamaphat, P. Limsuwan, and B. Ngotawornchai, 'Phase Characterization of TiO_2 Powder by XRD and TEM\n', *Nature Science*, vol. 42, pp. 357–361, 2008.

[49] L. L. P. Lim, R. J. Lynch, and S. I. In, 'Comparison of simple and economical photocatalyst immobilisation procedures', *Applied Catalysis A: General*, vol. 365, no. 2, pp. 214–221, 2009.

[50] W. Tu, Y. P. Lin, and R. Bai, 'Enhanced performance in phenol removal from aqueous solutions by a buoyant composite photocatalyst prepared with a two-layered configuration on polypropylene substrate', *Journal of Environmental Chemical Engineering*, vol. 4, no. 1, pp. 230–239, 2016.

[51] M. Akkari, P. Aranda, H. Ben Rhaiem, A. Ben Haj Amara, and E. Ruiz-Hitzky, 'ZnO/clay nanoarchitectures: Synthesis, characterization and evaluation as photocatalysts', *Applied Clay Science*, 2015.

[52] L. Pereira *et al.*, 'UV/TiO2 photocatalytic degradation of xanthene dyes', *Photochemistry and Photobiology*, vol. 89, no. 1, pp. 33–39, 2013.

[53] P. Zhou, Z. Le, Y. Xie, J. Fang, and J. Xu, 'Studies on facile synthesis and properties of mesoporous CdS/TiO_2 composite for photocatalysis applications', *Journal of Alloys and Compounds*, vol. 692, pp. 170–177, 2017.

[54] Yu JC, Yu JG, and Zhao JC, 'Enhanced photocatalytic activity of mesoporous and ordinary TiO_2 thin films by sulfuric acid treatment', *Appl. Catal. B: Environ.*, vol. 36, no. 1, pp. 31–43, 2002.

[55] R. Comparelli, E. Fanizza, M. L. Curri, P. D. Cozzoli, G. Mascolo, and A. Agostiano, 'UV-induced photocatalytic degradation of azo dyes by organic-capped ZnO nanocrystals immobilized onto substrates', *Applied Catalysis B: Environmental*, vol. 60, no. 1–2, pp. 1–11, 2005.

[56] J. Yang, J. Dai, C. Chen, and J. Zhao, 'Effects of hydroxyl radicals and oxygen species on the 4-chlorophenol degradation by photoelectrocatalytic reactions with TiO_2-film electrodes', *Journal of Photochemistry and Photobiology A: Chemistry*, vol. 208, no. 1, pp. 66–77, 2010.

[57] S. S. Chin, K. Chiang, and A. G. Fane, 'The stability of polymeric membranes in a TiO_2 photocatalysis process', *Journal of Membrane Science*, vol. 275, no. 1–2, pp. 202–211, 2006.

[58] Y. Ao, J. Xu, D. Fu, and C. Yuan, 'Preparation of porous titania thin film and its photocatalytic activity', *Applied Surface Science*, vol. 255, no. 5 PART 2, pp. 3137–3140, 2008.

[59] L. Pereira *et al.*, 'UV/TiO_2 photocatalytic degradation of xanthene dyes', *Photochemistry and Photobiology*, vol. 89, no. 1, pp. 33–39, 2013.

[60] M. Da Motta, R. Pereira, M. M. Alves, and L. Pereira, 'UV/TiO_2 photocatalytic reactor for real textile wastewaters treatment', *Water Science and Technology*, vol. 70, no. 10, pp. 1670–1676, 2014.

[61] A. R. Silva *et al.*, 'Ciprofloxacin wastewater treated by UVA photocatalysis: contribution of irradiated TiO_2 and ZnO nanoparticles on the final toxicity as assessed by Vibrio fischeri', *RSC Adv.*, pp. 95494–95503, 2016.

[62] U. I. Gaya and A. H. Abdullah, 'Heterogeneous photocatalytic degradation of organic contaminants over titanium dioxide: A review of fundamentals, progress and problems', *Journal of Photochemistry and Photobiology C: Photochemistry Reviews*, vol. 9, no. 1, pp. 1–12, 2008.

[63] M. Saquib and M. Muneer, 'TiO_2/mediated photocatalytic degradation of a triphenylmethane dye (gentian violet), in aqueous suspensions', *Dyes and Pigments*, vol. 56, no. 1, pp. 37–49, 2003.

[64] B. Erjavec, P. Hudoklin, K. Perc, T. Tišler, M. S. Dolenc, and A. Pintar, 'Glass fiber-supported TiO_2 photocatalyst: Efficient mineralization and removal of toxicity/estrogenicity of bisphenol A and its analogs', *Applied Catalysis B: Environmental*, vol. 183, pp. 149–158, 2016.

[65] D. Wang *et al.*, 'Self-assembled TiO_2–graphene hybrid nanostructures for enhanced Li-ion insertion', *ACS nano*, vol. 3, no. 4, pp. 907–914, 2009.

[66] Y. Zhang, Z.-R. Tang, X. Fu, and Y.-J. Xu, 'Engineering the unique 2D mat of graphene to achieve graphene-TiO_2 nanocomposite for photocatalytic selective transformation: what

advantage does graphene have over its forebear carbon nanotube?', *ACS nano*, vol. 5, no. 9, pp. 7426–7435, 2011.

[67] N. A. Almeida *et al.*, 'TiO_2/graphene oxide immobilized in P(VDF-TrFE) electrospun membranes with enhanced visible-light-induced photocatalytic performance', *Journal of Materials Science*, vol. 51, no. 14, pp. 6974–6986, 2016.

[68] N. An, H. Liu, Y. Ding, M. Zhang, and Y. Tang, 'Preparation and electroactive properties of a PVDF/nano-TiO_2 composite film', *Applied Surface Science*, vol. 257, no. 9, pp. 3831–3835, 2011.

[69] F. Liu, N. A. Hashim, Y. Liu, M. R. M. Abed, and K. Li, 'Progress in the production and modification of PVDF membranes', *Journal of Membrane Science*, vol. 375, no. 1–2, pp. 1–27, 2011.

[70] T. G. Mofokeng, 'Praparation and properties of PVDF based $BaTiO_3$ containing nanocomposites', University of the Fr, 2014.

[71] M. Hosseini and A. S. H. Makhlouf, *Industrial Applications for Intelligent Polymers and Coatings*. Springer, 2016.

[72] S. I. Rathnayake, Y. Xi, R. L. Frost, and G. A. Ayoko, 'Environmental applications of inorganic – organic clays for recalcitrant organic pollutants removal : Bisphenol A', *Journal of Colloid and Interface Science*, vol. 470, pp. 183–195, 2016.

[73] P. M. Martins, R. Miranda, J. Marques, C. J. Tavares, G. Botelho, and S. Lanceros-Mendez, 'Comparative efficiency of TiO_2 nanoparticles in suspension vs. immobilization into P(VDF-TrFE) porous membranes', *RSC Adv.*, vol. 6, no. 15, pp. 12708–12716, 2016.

[74] P. Martins, A. C. Lopes, and S. Lanceros-Mendez, 'Electroactive phases of poly(vinylidene fluoride): Determination, processing and applications', *Progress in Polymer Science*, vol. 39, no. 4, pp. 683–706, 2014.

[75] E. Cossich *et al.*, 'Development of electrospun photocatalytic TiO_2-polyamide-12 nanocomposites', *Materials Chemistry and Physics*, vol. 164, pp. 91–97, 2015.

[76] M. Hosseini and A. S. H. Makhlouf, *Industrial Applications for Intelligent Polymers and Coatings*. Springer, 2016.

[77] A. Salimi and A. A. Yousefi, 'FTIR studies of β-phase crystal formation in stretched PVDF films', *Polymer Testing*, vol. 22, no. 6, pp. 699–704, 2003.

[78] M. D. Duca, C. L. Plosceanu, and T. Pop, 'Surface modifications of polyvinylidene fluoride (PVDF) under rf Ar plasma', *Polymer Degradation and Stability*, vol. 61, no. 1, pp. 65–72, 1998.

[79] A. Salimi and A. A. Yousefi, 'FTIR studies of β-phase crystal formation in stretched PVDF films', *Polymer Testing*, vol. 22, no. 6, pp. 699–704, 2003.

[80] R. Gregorio, 'Determination of the alfa, beta, and gamma crystalline phases of poly(vinylidene fluoride) films prepared at different conditions', *Journal of Applied Polymer Science*, vol. 100, no. 4, pp. 3272–3279, 2006.

[81] Z. Ramakrishna, Seeram; Fujihara, Kazutoshi; Teo, Wee-Eong; Lim, Telk-Cheng; Ma, *An Introduction to Electrospinning and Nanofibers*, no. 1. 2005.

[82] J. Zheng, A. He, J. Li, and C. C. Han, 'Polymorphism control of poly(vinylidene fluoride) through electrospinning', *Macromolecular Rapid Communications*, vol. 28, no. 22, pp. 2159–2162, 2007.

[83] N. A. Almeida *et al.*, 'TiO_2/graphene oxide immobilized in P(VDF-TrFE) electrospun membranes with enhanced visible-light-induced photocatalytic performance', *Journal of Materials Science*, vol. 51, no. 14, pp. 6974–6986, 2016.

[84] E.-R. Kenawy, F. I. Abdel-Hay, M. H. El-Newehy, and G. E. Wnek, 'Processing of polymer nanofibers through electrospinning as drug delivery systems', *Materials Chemistry and Physics*, vol. 113, no. 1, pp. 296–302, 2009.

[85] V. Cardoso, 'Sistema de fluxo acústico de base polimérica para aplicações microfluídicas', Universidade do Minho.

[86] S. Ortelli, M. Blosi, S. Albonetti, A. Vaccari, M. Dondi, and A. Costa, 'TiO_2 based nano-photocatalysis immobilized on cellulose substrates', *Journal of Photochemistry and Photobiology A: Chemistry*, vol. 276, pp. 58–64, 2014.

[87] A. L. Costa, S. Ortelli, M. Blosi, S. Albonetti, A. Vaccari, and M. Dondi, 'TiO_2 based photocatalytic coatings: from nanostructure to functional properties', *Chemical engineering journal*, vol. 225, pp. 880–886, 2013.

[88] H. Tang, K. Prasad, R. Sanjines, P. Schmid, and F. Levy, 'Electrical and optical properties of TiO_2 anatase thin films', *Journal of applied physics*, vol. 75, no. 4, pp. 2042–2047, 1994.

[89] J.-G. Yu, H.-G. Yu, B. Cheng, X.-J. Zhao, J. C. Yu, and W.-K. Ho, 'The effect of calcination temperature on the surface microstructure and photocatalytic activity of TiO_2 thin films prepared by liquid phase deposition', *The Journal of Physical Chemistry B*, vol. 107, no. 50, pp. 13871–13879, 2003.

[90] R. J. Collins, H. Shin, M. R. DeGuire, A. H. Heuer, and C. N. Sukenik, 'Low temperature deposition of patterned TiO_2 thin films using photopatterned self-assembled monolayers', *Applied physics letters*, vol. 69, no. 6, pp. 860–862, 1996.

[91] A. W. Chester and E. G. Derouane, *Zeolite characterization and catalysis: A tutorial*. 2010.

[92] H. Gu, C. Wang, S. Gong, Y. Mei, H. Li, and W. Ma, 'Investigation on contact angle measurement methods and wettability transition of porous surfaces', *Surface and Coatings Technology*, vol. 292, pp. 72–77, 2016.

[93] E. Balaur, J. M. Macak, L. Taveira, and P. Schmuki, 'Tailoring the wettability of TiO2 nanotube layers', *Electrochemistry Communications*, vol. 7, no. 10, pp. 1066–1070, 2005.

[94] Q. Du, J. Liu, L. Guo, M. Lv, and X. Zeng, 'Tailoring the surface wettability of polyimide by UV laser direct texturing in different gas atmospheres', *Materials & Design*, vol. 104, pp. 134–140, 2016.

[95] Y. Leng, *Materials characterization: introduction to microscopic and spectroscopic methods*. John Wiley & Sons, 2009.

[96] Ashcroft, 'Solid state physics', vol. lll. 1971.

[97] R. Egerton, *Physical Principles of Electron Microscopy*. 2005.

[98] S. Bhattacharjee, 'DLS and zeta potential - What they are and what they are not?', *Journal of Controlled Release*, vol. 235, pp. 337–351, 2016.

[99] 'Operation of the Zetasizer Nano - Size measurements', in *Zetasizer Nano Seriees*, p. 14.

[100] Malvern, 'Zeta potential theory', in *Zetasizer Nano Series User Manual*, pp. 15-1-12, 2009.

[101] L. Benavente *et al.*, 'FTIR mapping as a simple and powerful approach to study membrane coating and fouling', *Journal of Membrane Science*, vol. 520, pp. 477–489, 2016.

[102] G. Bracco and B. Holst, *Surface science techniques*, vol. 51, no. 1. 2013.

[103] J. N. Israelachvili, *Intermolecular and Surface Forces*, 2nd ed. California, USA: Academic Press, 1991.

[104] Pike Technologies, 'APPLICATION NOTE ATR – Theory and Applications', *Pike Technologies*, pp. 1–3, 2014.

[105] P. L. King, M. S. Ramsey, P. F. McMillan, and G. Swayze, 'Laboratory fourier transform infrared spectroscopy methods for geologic samples', *Infrared Spectroscopy in Geochemistry, Exploration Geochemistry and Remote Sensing*, pp. 57–91, 2004.

[106] PerkinElmer, 'FT-IR Spectroscopy Attenuated Total Reflectance (ATR)', *PerkinElmer Life and Analystical Sciences*, pp. 1–5, 2005.

[107] S. Behera, S. Ghanty, F. Ahmad, S. Santra, and S. Banerjee, 'UV-Visible Spectrophotometric Method Development and Validation of Assay of Paracetamol Tablet Formulation', *J Anal Bioanal Techniques*, vol. 3, no. 6, p. 151, 2012.

[108] T. H. Fereja, M. F. Seifu, and T. Y. Mola, 'UV-Visible spectrophotometric method development and quantification of ciprofloxaciline in tablets dosage form', *American journal Pharmacy and Pharmacology*, vol. 2, no. 1, pp. 1–8, 2015.

[109] M. Hijosa-Valsero *et al.*, 'Removal of antibiotics from urban wastewater by constructed wetland optimization', *Chemosphere*, vol. 83, no. 5, pp. 713–719, 2011.

[110] M. Remer *et al.*, 'Dynamic water contact angle during initial phases of droplet impingement', *Colloids and Surfaces A: Physicochemical and Engineering Aspects*, vol. 508, pp. 57–69, 2016.

[111] B. Cacciapuoti, W. Sun, and D. G. McCartney, 'A study on the evolution of the contact angle of small punch creep test of ductile materials', *International Journal of Pressure Vessels and Piping*, vol. 145, pp. 60–74, 2016.

[112] S. M. El-Sheikh, T. M. Khedr, A. Hakki, A. A. Ismail, W. A. Badawy, and D. W. Bahnemann, 'Visible light activated carbon and nitrogen co-doped mesoporous TiO_2 as efficient photocatalyst for degradation of ibuprofen', *Separation and Purification Technology*, vol. 173, pp. 258–268, 2017.

[113] K. A. Langdon, M. Stj, R. J. Smernik, A. Shareef, and R. S. Kookana, 'Comparison of degradation between indigenous and spiked bisphenol A and triclosan in a biosolids amended soil', *Science of the Total Environment*, vol. 447, pp. 56–63, 2013.

[114] K. Chiang, T. M. Lim, L. Tsen, and C. C. Lee, 'Photocatalytic degradation and mineralization of bisphenol A by TiO_2 and platinized TiO2', *Applied Catalysis A: General*, vol. 261, no. 2, pp. 225–237, 2004.

[115] M. N. Chong, S. Lei, B. Jin, C. Saint, and C. W. K. Chow, 'Optimisation of an annular photoreactor process for degradation of Congo Red using a newly synthesized titania impregnated kaolinite nano-photocatalyst', *Separation and Purification Technology*, vol. 67, no. 3, pp. 355–363, 2009.

[116] D. Heger, J. Jirkovský, and P. Klán, 'Aggregation of methylene blue in frozen aqueous solutions studied by absorption spectroscopy', *Journal of Physical Chemistry A*, vol. 109, no. 30, pp. 6702–6709, 2005.

APPENDIX

ANNEX A – STANDARD XRD SPECTRUM CARDS

The standard spectrum JCPDS cards 88-1175 and 84-1286, used to characterize the particle's phase, can be observed in Figure 31.

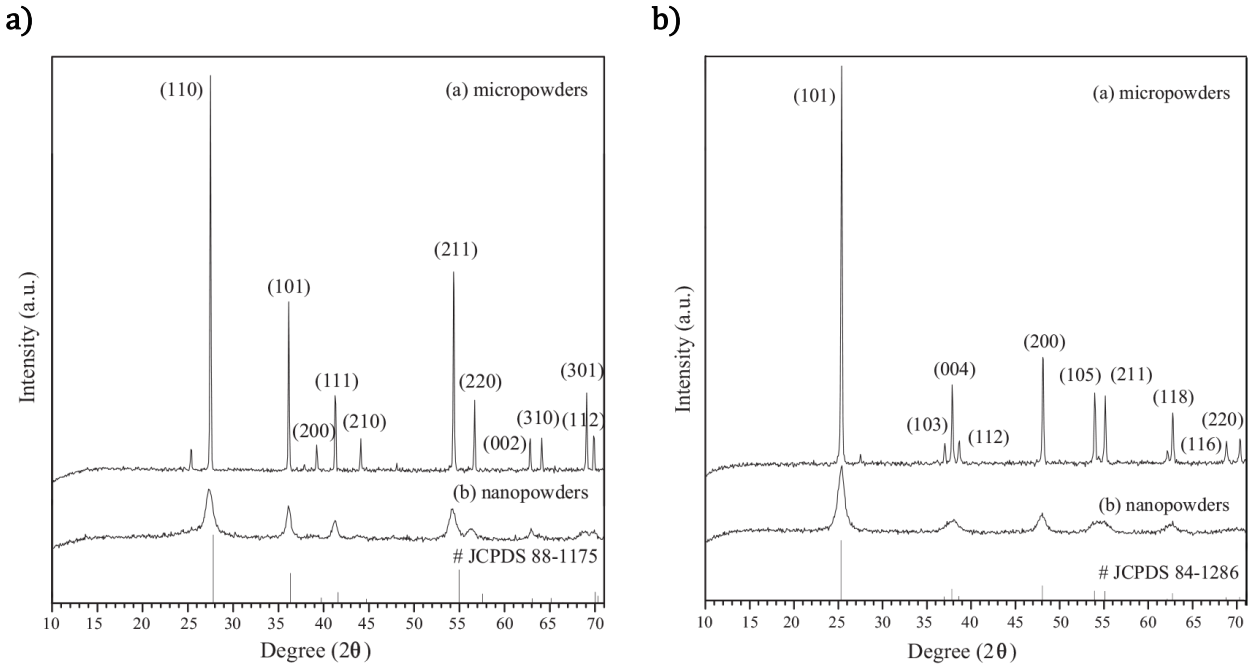

Figure 31 – a) XRD JCPDS card 88-1175 pattern of rutile TiO_2 micropowders; **b)** XRD JCPDS card 84-1286 pattern of anatase TiO_2 micropowders. Adapted from **[48]**.

ANNEX B – ELECTROACTIVE PHASES OF POLY(VINYLIDENE DIFLUORIDE) OBTAINED THROUGH INFRARED SPECTROSCOPY

As was previously discussed, FTIR spectra of PVDF provides information about its structure and allows to distinguish between its different crystalline forms. The characteristic bands of each crystalline phase are summarized in Figure 32.

a)

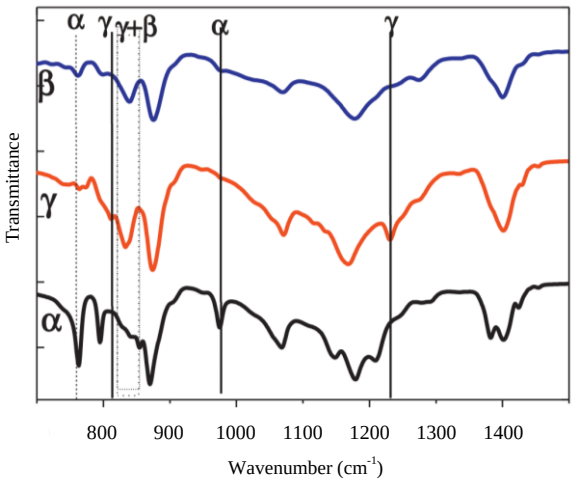

b)

	α	*β*	*γ*
Wavenumber (cm^{-1})	408	510	431
	532	840	512
	614	1279	776
	766	1400	812
	795		833
	855		840
	976		1234

Figure 32 – Absorption FTIR bands characteristics of **α, β** and **γ** PVDF. **a)** Graphical representation; **b)** Wavenumber values of the phases. Taken from **[74]**.

The identified bands can be used to identify the phase content. α-Phase of PVDF presents a large number of characteristic bands. Making it the most easily detected by FTIR absorption. There are also bands which are common to both β and γ-phases due to their similar polymer chain conformation, appearing at similar wavenumbers, as is the case for the γ-phase band at 512 cm^{-1} and the β-phase band at 510 cm^{-1}. For the case of the band at 840 cm^{-1}, it is accepted as common to both polymorphs but a strong band only for the β-phase, with the γ-phase it appearing more as a shoulder of the 833 cm^{-1} band. Some other bands are associated to the amorphous phase of the polymer, but will not be discussed [74], [76], [80].

ANNEX C – ABSORBANCE SPECTRUM AND CALIBRATION CURVE

According to the Beer-Lambert law, the concentration is directly associated with the absorbance value [107], [108]. From this assumption, it is able to determine the molar coefficient, Ɛ, through the calibration curve of a compound. Initially, for this, sets of deluded solutions were prepared using the dye Methylene blue (MB) with various concentrations, 0.025, 0.05, 0.1, 2.5, 5, 10 and 40 mg L^{-1}, diluted in water. Considering that the concentration is given by the number of moles in a determined volume, the relation between the concentration and volume in a diluted solution can be given by the equation:

$$C_i V_i = C_f V_f \quad (16)$$

where C_i is the initial concentration of the solution and V_i is the initial volume. C_f and C_f are the concentration and volume of the final solution. Before any other analysis took place, the visual results for MB can be observed in Figure 33, as the blue color diminishes with higher dilution.

Figure 33 – Visual colour loss in relation to the concentrations of MB: 0.025, 0.05, 0.1, 0.5, 2.5, 10 and 40 mg L^{-1}.

The Absorbance of the samples was then analyzed by a Biotek Cytation3 Microplate reader in spectrum mode, 200 µL replicated three times for each concentration, using a set of 96 well plates, and a Shimadzu UV-Vis spectrophotometer, in order to also compare the two data reading methods. This method is used to obtained the calibration curve, which helps determining the necessary concentration of solution for the desired absorbance. Using the spectra in Figure 34, the absorbance peak of MB, 669 nm, was plotted as a function of the concentration and the corresponding Lambert-Beer calibration curve was drawn. These results can be observed in Figure 34, as MB's absorbance values increase proportionally with the increasing of the concentration.

a)

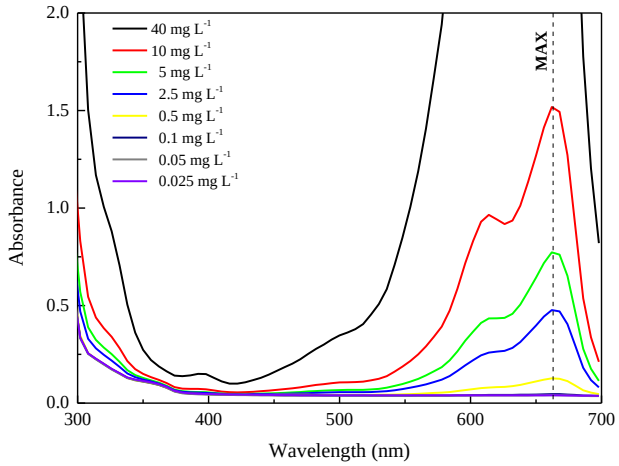

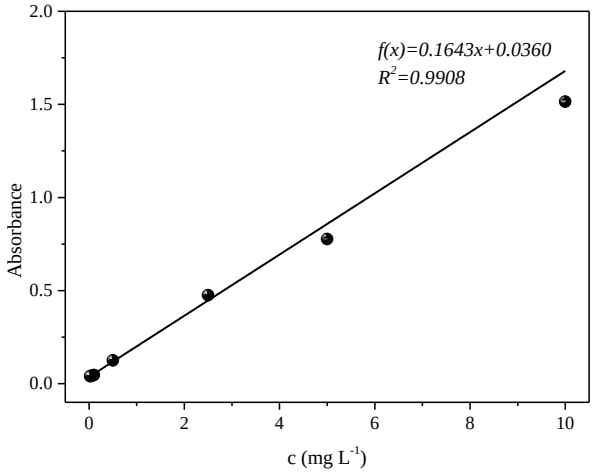

b)

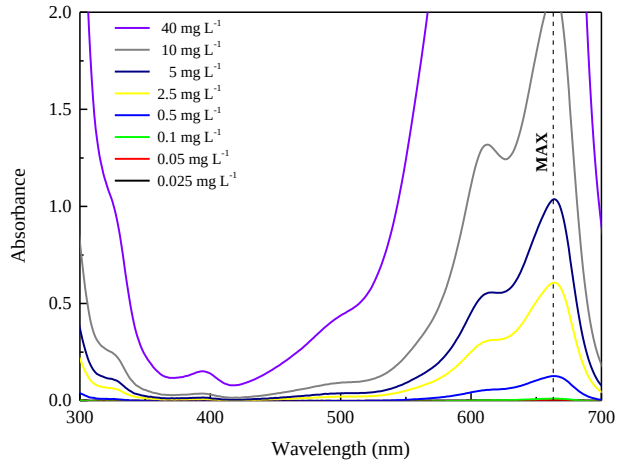

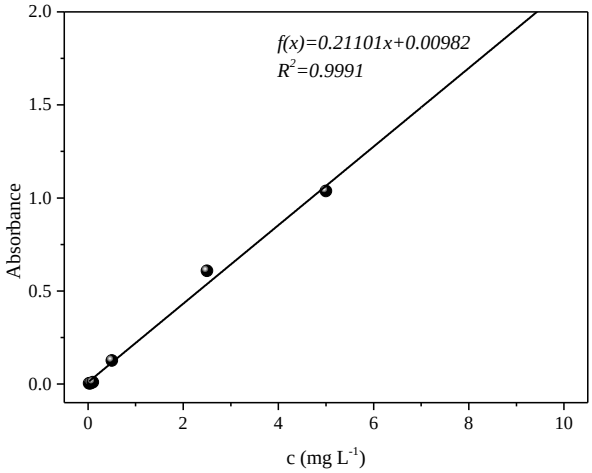

Figure 34 – Absorbance spectrum (left side) and calibration curve (right side) of MB obtained by **a)** microplate reader; **b)** UV-Vis spectrophotometer.

The main absorbance peak of MB is at 669 nm (Figure 34). Another smaller peak can be observed at 609 nm [116], but will not be considered. The values equivalent to 40 mg L^{-1} must be disregarded, as the peak surpasses the measuring capacity of the equipment, meaning the solution is saturated. The resulting equations for the calibration curves can also be observed. Calibration curves were also plotted for CIP, IBP and BPA using UV-Vis Data (Figure 35).

a)

$f_{CIP}(x) = 0.1262x + 0.0005$

$R^2{}_{CIP} = 0.9999$

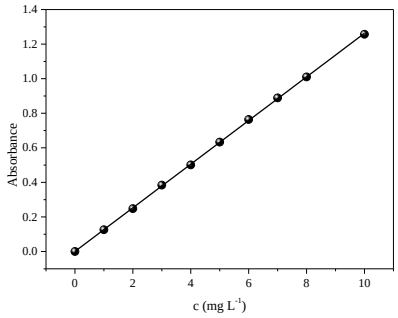

b)

$f_{IBP}(x) = 0.0399x + 0.0039$

$R^2{}_{IBP} = 0.9999$

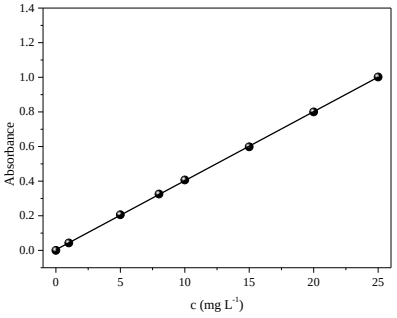

c)

$f_{BPA}(x) = 0.0137x + 0.0034$

$R^2{}_{BPA} = 0.9999$

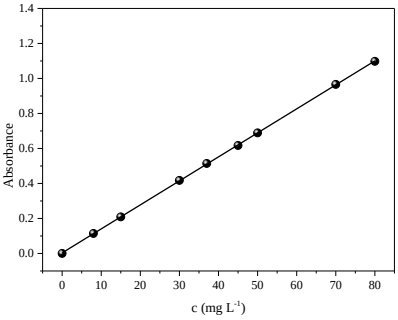

Figure 35 – Calibration curves and respective equations for **a)** CIP; **b)** IBP; **c)** BPA.

All the results obtained from the calibration curves of all the micropollutants studied in this work can be observed and compared in Table 12.

Table 12 – List of molar extinction coefficient **ε** and respective standard error for all the studied micropollutants using two different methods.

Type	**Microplate Reader**		**UV-Vis Spectrophotometer**	
	ε ($\mu g^{-1} L cm^{-1}$)	**$\Delta\varepsilon$**	**ε ($\mu g^{-1} L cm^{-1}$)**	**$\Delta\varepsilon$**
MB	0.1643	0.0065	0.2110	0.0040
CIP	-	-	0.1262	0.0005
IBP	-	-	0.0399	0.0001
BPA	-	-	0.0137	0.00004

In order to compare our results more efficiently in the future, one way is to use the same estimated initial absorbance value for all samples. This can be achieved through Equation (11), in which the relation is obtained:

$$c = \frac{A}{\varepsilon \cdot l} \tag{17}$$

which, assuming $l = 1$ cm and $A = 0.6$ (a. u.), allows us to calculate the necessary approximate concentrations needed for each compound and can be seen in Table 13.

Table 13 – Concentrations of micropollutants obtained through equation and concentrations used in this work.

Micropollutant	c (mg L^{-1})	
	Obtained	Used in this work
MB	2.8	2
CIP	4.8	5
IBP	15.0	15
BPA	43.8	45

ANNEX D – MICROPOLLUTANTS CONTROL CURVES

The control kinetic curves of the photocatalytic degradation of 2 mg L^{-1} of MB, 5 mg L^{-1} of CIP, 15 mg L^{-1} of IBP and 45 mg L^{-1} of BPA, with TiO_2 nanoparticles in solution, P(VDF-TrFE)/TiO_2 and P(VDF-TrFE)/TiO_2/NaY membranes in the dark (without UV) and P(VDF-TrFE) membranes without catalyst under UV, are presented in Figure 36.

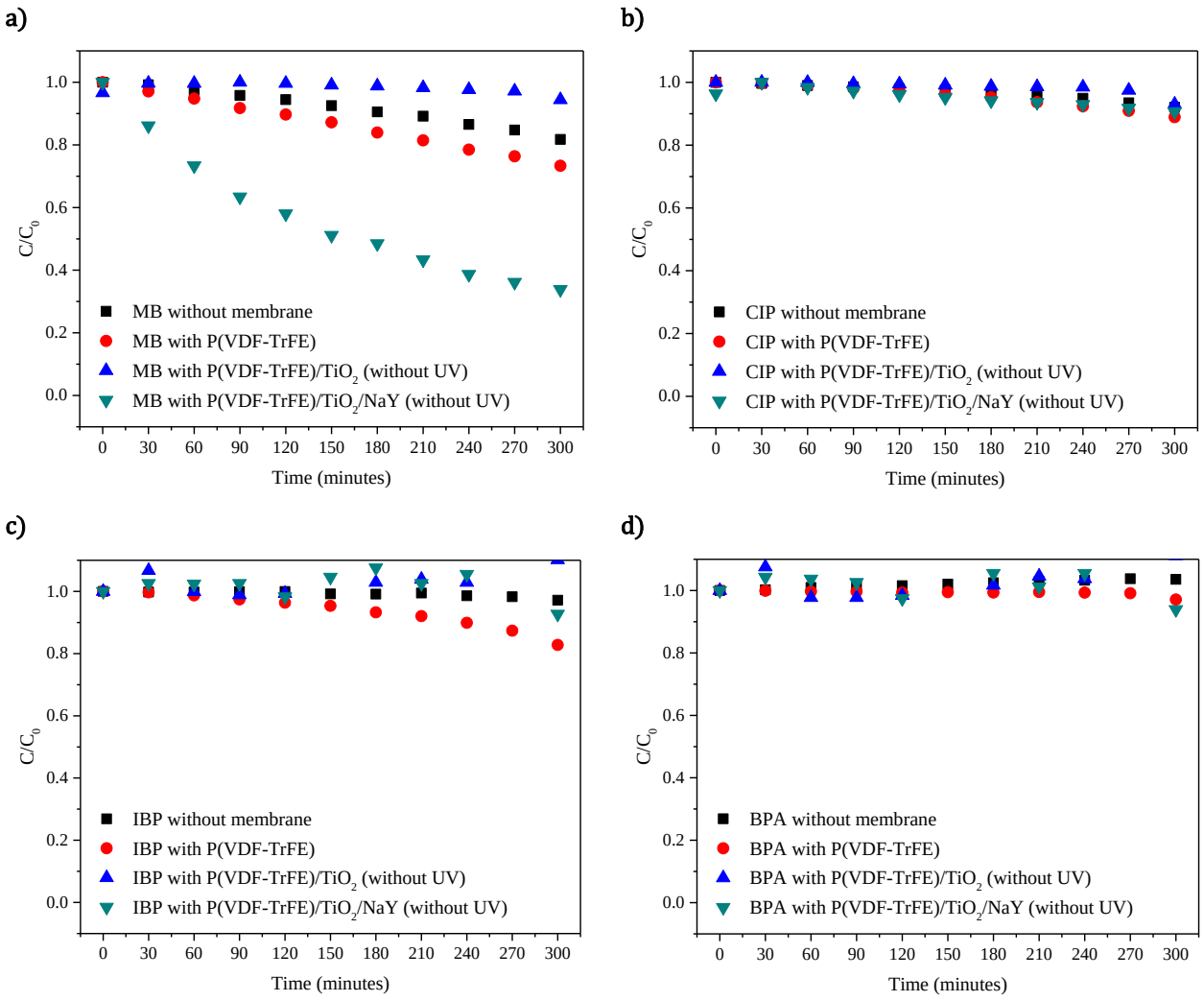

Figure 36 – Controls used for the photocatalytic degradation of **a)** MB; **b)** CIP; **c)** IBP; **d)** BPA.

Figure 36, shows low to none degradation took place after a total time of 300 minutes, apart from Figure 36.a, where the curve where zeolites were present in the membrane shows a decrease of 40% of absorbance after 300 minutes. This leads us to believe that the decrease in absorbance is not, in fact, due to degradation, but to the occurrence of adsorption by the NaY

particles, as the same is not seen in the other tests with other membranes (with and without UV). This occurrence is also more prominent in the results where MB was used.